The Pennsylvania State University

The Graduate School

Department of Civil and Environmental Engineering

SPATIAL AND TEMPORAL PATTERNS OF WATER STABLE ISOTOPE COMPOSITIONS AT THE SUSQUEHANNA-SHALE HILLS CRTICAL ZONE OBSERVATORY

A Thesis in

Civil Engineering

by

Evan M. Thomas

Submitted in Partial Fulfillment
of the Requirements
for the Degree of

Master of Science

August 2013

The thesis of Evan M. Thomas was reviewed and approved* by the following:

Christopher Duffy
Professor of Civil and Environmental Engineering
Thesis Advisor

Henry Lin
Professor of Hydropedology/Soil Hydrology

Michael Gooseff
Associate Professor of Civil and Environmental Engineering

Peggy A. Johnson
Professor of Civil Engineering
Head of the Department of Civil and Environmental Engineering

*Signatures are on file in the Graduate School

ABSTRACT

Patterns of water flow paths and time scales are important for nearly all environmental processes within in the Critical Zone. To better understand these hydrological processes, a water stable isotope network was established at the Susquehanna-Shale Hills Critical Zone Observatory to determine spatial and temporal dynamics of the hydrologic pools (precipitation, soil water, groundwater, and stream water) within the catchment. Precipitation samples were collected automatically on an event basis in a clearing at the ridge top. Soil water was collected every two weeks from four distinct transects at varying depths using suction cup lysimeters. Groundwater at two locations in the stream riparian and stream water at the outlet were collected daily using automatic samplers. Groundwater was also sampled every two weeks at 18 spatially distributed wells throughout the catchment. Isotopic analysis was performed using LGR Isotope Analyzer following IAEA guidelines. Results demonstrated the strong seasonality of precipitation isotope compositions and relative stationarity of groundwater isotopic compositions around the annual amount weighted isotope composition of precipitation suggesting groundwater is recharged by precipitation from each season, but that recharge mechanisms appear to differ during the year. Results strongly demonstrate the ability of the soil profile to attenuate the seasonal isotopic composition of the input to a constant composition at a depth of 1.5 m suggesting the importance of hydrodynamic mixing of precipitation from different seasons. Spatial patterns of soil water isotope profiles showed asymmetric snow melt dynamics between the north and south slopes. Investigations of standard deviations of seasonal isotope profiles provided evidence of lateral preferential flow along soil horizon and soil-bedrock interfaces during the cold season and vertically through macropores during the warm season.

Investigation of the temporal dynamics of isotopic composition of precipitation yielded interesting results with respect to the influence of precipitation amounts and type on expected frequencies as well as the local meteoric water line. A test case of a small subset of the precipitation record showed that incorporation of precipitation amounts to one-dimensional and two-dimensional kernel density estimates shifted the distribution substantially. Full record unweighted and weighted kernel density estimates revealed that isotope compositions of precipitation were not symmetrical but skewed towards more depleted values for the four year monitoring period. Monthly weighted kernel density estimates showed the importance of snow and tropical storm isotopic composition imposing a seasonal variation to the precipitation record. Time integration of precipitation isotope compositions using an amount weighing procedure from event to seasonally amount weighted isotope compositions reduced the variability within the record yet preserved the seasonal cycle. Construction of local meteoric water lines using event, daily, weekly, monthly, and seasonally amount weighted isotope composition time series demonstrated the significance of incorporation of precipitation amounts and averaging, with event and daily local meteoric water lines being statistically different from a local meteoric water line based on a precipitation amount weighted least squares regression. These differences in local meteoric water lines become important when investigations of hydrologic pool interactions or other moderate to long-term hydrologic processes are in question.

Utilizing the knowledge of earlier investigations, a robust comparison of two isotope incorporated atmospheric general circulation models against SSHCZO observations was performed with the goal of developing a fully distributed high-resolution data product predicting isotope compositions of precipitation for the Chesapeake Bay. Comparisons were performed on daily, weekly, and monthly amount weighted values as well as monthly values from the Online Isotopes in Precipitation Calculator. Linear regression results showed the best agreement between the monthly amount weighted values yet Nashe-Sutcliffe coefficients were only 0.2807 and 0.5792 for the global GCM and regional GCM respectively. To determine the temporal structure of the time series, singular spectrum analysis (SSA) was performed on both GCM models and observations from SSHCZO. SSA results demonstrated the importance of the annual cycle and its harmonics. Reconstruction of weekly amount weighted isotope compositions for the regional model and SSHCZO recovered 43.44% and 51.78% amounts of the variance respectively suggesting much of the records contain inherent noise.

TABLE OF CONTENTS

LIST OF FIGURES VII
LIST OF TABLES XIII
ACKNOWLEDGEMENTS XIV

Chapter 1. INTRODUCTION 1
1.1. BACKGROUND 1
1.2. WATER STABLE ISOTOPE OVERVIEW 3
1.3. GEOSPATIAL DATA AND SURVEYING AT SSHCZO 5
1.4. RESEARCH OBJECTIVES AND EFFORTS 6

Chapter 2. SPATIOTEMPORAL PATTERNS OF STABLE ISOTOPE COMPOSITIONS AT THE SHALE HILLS CRITICAL ZONE OBSERVATORY: LINKAGES TO SUBSURFACE HYDROLOGIC PROCESSES 7
2.1. ABSTRACT 7
2.2. INTRODUCTION 7
2.3. METHODS & MATERIALS 9
2.3.1. SITE DESCRIPTION 9
2.3.2. DATA COLLECTION 12
2.3.3. DATA ANALYSIS 15
2.4. RESULTS 17
2.4.1. CATCHMENT HYDROLOGY 17
2.4.2. PRECIPITATION ISOTOPE COMPOSITION 17
2.4.3. DEPTH-TIME VARIABILITY OF SOIL WATER ISOTOPE COMPOSITIONS 20
2.4.4. SPATIAL VARIABILITY OF SOIL WATER ISOTOPE COMPOSITIONS 25
2.5. DISCUSSION 29
2.5.1. DAMPING OF SEASONALITY WITH SOIL DEPTH, ADVECTION, AND MIXING 29
2.5.2. EVIDENCE FOR PREFERENTIAL FLOW 29
2.5.3. SNOW MELT DYNAMICS 31
2.5.4. EVAPORATION DYNAMICS 32
2.6. SUMMARY CONCLUSION 33
2.7. ACKNOWLEDGEMENTS 35

Chapter 3. INTERPRETING HIGH-RESOLUTION SAMPLING OF PRECIPITATION ISOTOPE COMPOSITIONS FOR HYDROLOGIC APPLICATIONS 36
3.1. ABSTRACT 36
3.2. INTRODUCTION 36
3.3. MATERIALS & METHODS 38
3.3.1. SSHCZO DESCRIPTION & CLIMATE 38
3.3.2. MONITORING PROCEDURES & ISOTOPIC ANALYSIS 40
3.3.3. ANALYSIS METHODS 41
3.4. RESULTS & DISCUSSION 44
3.4.1. OBSERVED METEOROLOGY 44
3.4.2. KERNEL DENSITY ESTIMATIONS 46
3.4.3. TEMPORAL PATTERNS OF ISOTOPES IN PRECIPITATION 52

3.4.4. LMWL Based on Different Integration Periods 56
3.5. Summary & Conclusion 59

Chapter 4. Validation of Precipitation Isotope Compositions from an Atmospheric General Circulation Model Using SSHCZO Observations 61
4.1. Abstract 61
4.2. Introduction 62
4.3. Data 63
4.3.1. Isotope-Incorporated Atmospheric General Circulation Models 63
4.3.2. Online Isotopes in Precipitation Calculator (OIPC) 64
4.3.3. Susquehanna-Shale Hills Critical Zone Observatory 64
4.4. Methods 66
4.4.1. Time Integration 66
4.4.2. Regression Procedures 67
4.4.3. Singular Spectrum Analysis (SSA) 68
4.5. Results & Discussion 70
4.5.1. Regression Results 71
4.5.2. SSA Results 73
4.5.3. 32-Year Reconstruction at SSHCZO 80
4.6. Summary & Conclusions 82

Chapter 5. Conclusions and Future Work 84
5.1. Summary of Completed Work 84
5.2. Potential Future Work 85
5.2.1. Continued Isotope Hydrology Studies at SSHCZO 85
5.2.2. Spatial Validation of Results from Downscaled Atmospheric GCM 86
5.2.3. Distributed Isotopic Age Modeling of Chesapeake Bay watershed 87

References Cited 88

Appendix A. **Data Management: Comparison between LPM and Ott Instruments 95**
Appendix B. **Data Management: SSHCZO Stream Flow 102**
Appendix C. **Local Meteoric Water Line Regression Procedures 103**

LIST OF FIGURES

Figure 1-1: Location of Susquehanna-Shale Hills Critical Zone Observatory in relation to the Chesapeake Bay watershed. **2**

Figure 2-1: Topographic map of Susquehanna-Shale Hills Critical Zone Observatory with stable isotope monitoring instruments. Colors indicate soil type based on field observations (Lin et al., 2006). Ten-minute precipitation amounts and event-based water samples were collected at the ridge top clearing (grey box) for isotope analysis. Soil water was collected bi-weekly at four nested lysimeter transects (orange circles) as described by Jin et al., (2011). Two unscreened groundwater wells were installed in the stream riparian zone to observe daily evolution of isotope composition (dark blue triangles). Depth to groundwater table was monitored in real-time in the stream riparian zone (teal triangle). Stream discharge and isotope composition values were monitored daily at the double V-notch weir located at the stream outlet (red triangle). **11**

Figure 2-2: Violin plots of the distribution of oxygen-18 (a) and deuterium (b) compositions in precipitation. The plot for the total record consists of precipitation events collected from Jan. 14, 2009 to Feb. 12, 2012, with sample number n indicated. Seasons are divided based on astronomical calendar to more closely correspond to the growing season within the catchment. Colors of the seasons correspond to colors used in seasonal soil water profile figures (**Figure 2-3**, **Figure 2-7**, **Figure 2-8**, and **Figure 2-9**). The shape of the violin plot is the smoothed, weighted kernel density distribution, normalized so the area of each plot is equal to one. The center square is the amount-weighted mean composition and the bars are plus and minus two weighted-standard deviations. Black points are individual data points, jittered horizontally for visualization. **18**

Figure 2-3: A total of 331 precipitation samples collected for isotope composition from Jan. 14, 2009 to Feb. 12, 2012. Precipitation is shown as both rain (grey circles) and snow (blue stars). All samples were collected over six-hour intervals. The local meteoric water line (LMWL, solid line) was calculated using all precipitation samples (a). The global meteoric water line (GMWL, dashed line) is plotted for reference. The time series of $\delta^{18}O$ for all precipitation samples and the daily precipitation record (b) with precipitation grouped into rain and snow. **19**

Figure 2-4: Temporal variation in weekly precipitation amount (dark bars), and the isotope composition of precipitation (gray bars) and soil water at three depths (shallow, intermediate, and deep). Soil water data prior to November 2008 are not shown since precipitation record did not begin until January 2009. Shaded regions correspond to one standard deviation of each soil depth. Data for each soil depth is averaged over the entire catchment. Groundwater mean (green line) is shown as a reference. **20**

Figure 2-5: Monthly amount-weighted isotope composition in precipitation, the kriged map of soil water isotope composition through depth and time, and monthly precipitation amount. Red values correspond to less-depleted isotope composition while blue values correspond to more-depleted values. Black circles correspond to catchment-averaged lysimeters (see text). Ten-day moving averages of the groundwater level in the valley floor are plotted as a black line. Kriging uncertainty contours are plotted over the same space-time domain (see supplemental materials). Ordinary kriging and kriging variance were computed in Matlab. **21**

Figure 2-6: Violin plots of the distribution of deuterium (**a**) and oxygen-18 (**b**) composition for each hydrologic pool within the catchment sampled from Jun. 13, 2008 to Mar. 16, 2012, with sample number, n, indicated. The full record was split into four seasons, spring (**c**), summer (**d**), fall (**e**), and winter (**f**), based on astronomical calendar. The full soil profile violin plot (orange) is a composite of shallow soil water (purple, ≤30 cm), intermediate soil water (teal, 40-100 cm), and deep soil water (blue, ≥120 cm). The shape of the violin plot is the smoothed kernel density distribution, normalized so the area of each plot is equal to one. Inside each violin plot is a standard bar plot. The white point corresponds to the median of the data, inner black box is interquartile range, and whiskers cover 1.5 interquartile range. Outliers are left off for clarity, but can be seen in the tails of the kernel density distribution.. **22**

Figure 2-7: Seasonal $\delta^{18}O$ profiles of soil water for wet (winter) and dry (summer) seasons (a) and transitional seasons (spring and fall) (b) based on the three-year monitoring. Isotope composition at each depth was averaged over the entire catchment. One standard deviation is represented with shaded regions. Depths with only one sample were removed for clarity. For reference, groundwater mean and one standard deviation is shown as a grey bar, and the amount weighted precipitation compositions with weighted standard error for corresponding seasons are shown as colored arrows at the top. **24**

Figure 2-8: Seasonally-averaged $\delta^{18}O$ composition in soil profiles for the north (south-facing) (a) and south (north-facing) (b) slopes based on the three-year monitoring. One standard deviation is represented with shaded regions. Depths with only one sample were removed for clarity. Typical soil horizon interfaces are shown as black dashed lines. Groundwater mean and one standard deviation are shown as grey bar for reference.. **26**

Figure 2-9: Seasonally-averaged $\delta^{18}O$ composition in soil profiles for each slope location based on the three-year monitoring: ridge top (a), midslope (b), and valley floor (c). One standard deviation is represented with shaded regions. Depths with only one sample were removed for clarity. Typical soil horizon interfaces are shown for each slope location. Groundwater mean and one standard deviation are shown as grey bar for reference. **27**

Figure 2-10: Seasonally-averaged $\delta^{18}O$ composition in soil profiles for hillslope type based on three-year monitoring: swale depression (a) and planar hillslope (b). One standard deviation is represented with shaded regions. Depths with only one sample were removed for clarity. Typical soil horizon interfaces are shown for each hillslope type. Groundwater mean and one standard deviation are shown as grey bar for reference. **28**

Figure 2-11: Shallow (≤30 cm depth) and intermediate (40-100 cm depth) soil water sampled during the summer (dry) season with SSHCZO Local Meteoric Water Line. Amount weighted precipitation compositions with weighted standard error bars for each of the four seasons are shown for reference. Green region indicates groundwater average (± one standard deviation) for each isotope composition. **33**

Figure 3-1: Location of Susquehanna-Shale Hills Critical Zone Observatory (yellow start) with respect to the Chesapeake Bay major watersheds (black lines). **39**

Figure 3-2: Monthly climate normals for precipitation (grey bars) and temperature (grey circles) based on NOAA 30-year record and monthly precipitation and temperature observations at SSHCZO for 2009 – 2012. .... **45**

Figure 3-3: One-dimensional kernel density estimations for unweighted (a) and weighted (b) subset of full precipitation dataset. Gaussian kernels (blue curves) are centered over data points (red points) and have a standard deviation equal to one. Summation of individual Gaussian kernels gives kernel density estimation with bandwidth equal to one (red curve). Kernel density estimation with bandwidth selected using Silverman method is shown in black. Distribution shapes change with bandwidth selection and incorporation of precipitation amounts. **47**

Figure 3-4: Individual two-dimensional Gaussian kernels, with x and y-directional standard deviation estimated using the Silverman method for bandwidth selection, are centered at the observations for unweighted (a) and weighted (c) subsets of full precipitation dataset. Smooth two-dimensional KDEs using Silverman method to estimate bandwidth for the unweighted (b) and weighted (d) dataset show distinct differences in the peak density and shape of distributions. **49**

Figure 3-5: One-dimensional unweighted (a) and weighted (b) kernel density estimates and probability density histograms for all observed $\delta^{18}O$ values of precipitation for 2009-2012. Bandwidth selection for kernel density estimates was made using Silverman method. Bin width selection for histograms was made using Freedman–Diaconis' method. Both unweighted and weighted distributions of $\delta^{18}O$ values of precipitation are negatively skewed; yet incorporation of precipitation amounts reduces the peak probability of the kernel density estimate and slightly shifts the distribution towards the more depleted range. **50**

Figure 3-6: Two-dimensional unweighted (a) and weighted (b) kernel density estimates for all observed $\delta^{18}O$ and δD values of precipitation for 2009 – 2012. Bandwidth selection for kernel density estimates was made using Silverman method. Contour intervals correspond to 95, 90, 75, 50, 25, 10, and 5% inclusion quantiles. LMWL calculated using precipitation amount weighted least squares and sample points are shown for reference. Both two-dimensional KDEs show skewness towards more negative values. 51

Figure 3-7: Observed $\delta^{18}O$ compositions in precipitation for SSHCZO for 2009 – 2012. Sample compositions were integrated independently to daily, weekly, monthly, seasonally, and yearly amount weighted compositions from individual samples. Major meteorological events are shown as grey bars and correspond to earliest observed snowfall (i), two-day snow event (ii), Tropical Storm Nicole (iii), Tropical Storm Lee (iv), record snow event (v), and Hurricane Sandy (vi). Seasonal variability is preserved through all sub-annual integration periods. Sample, daily, and weekly amount weighted time series contain large variability where as monthly, seasonally, and yearly amount weighted time series are relatively smooth. 53

Figure 3-8: Monthly weighted kernel density estimates of precipitation $\delta^{18}O$ values at SSHCZO for 2009 – 2012 and the 4-year composite weighed kernel density estimate. KDEs were constructed using sample $\delta^{18}O$ values and precipitation amounts. The x-axis for each plot has been scaled to allow for clear interpretation of the shape of each KDE. Each KDE for each precipitation type and month has been normalized by amount, therefore the area under all KDEs for a given month is equal to one. Precipitation type was determined using LPM (see text) or by major tropical storm events (Nicole, Lee, or Sandy). Sample number for rain, tropical storm, or snow KDE is listed at the top of each subplot. Based on LPM measurement of "No Precipitation," twenty samples were not included in KDEs. 55

Figure 3-9: Close up comparison of local meteoric water lines for SSHCZO based on different integration periods. Inset figure shows extents of observed isotopic composition of precipitation for 2009-2012. Groundwater ellipse encompassing 95% of observed groundwater isotope compositions is show in both figures for reference. LMWLs defined by individual samples and daily amount weighted values fall directly on each other. 57

Figure 3-10: Local meteoric water line for SSHCZO (a) defined using least squares regression of individual samples (black line) and amount weighted least squares regression of individual samples (orange line). Comparison of d-excess values and precipitation amount (b) show large negative values associated only with small precipitation amounts. Colors of scatter points correspond to d-excess values, where lighter colors are more negative and darker colors are positive d-excess values. 58

Figure 4-1: Location of SSHCZO (green point) in relation to IsoGSM grid cell (pink square) and IsoRSM domain (black rectangle). IsoRSM domain consisted of 129 grid cells east-west and 120 grid cells north-south. Blue shaded regions correspond to IsoRSM simulated precipitation isotope compositions for an arbitrary day for demonstration purposes only. 66

Figure 4-2: Daily, weekly, and monthly amount weighted time series for IsoGSM (light grey), IsoRSM (dark grey), OIPC (green), and SSHCZO observations (blue). Long-term averages are shown for each time period (right panels). 71

Figure 4-3: Comparison of IsoRSM (blue), IsoGSM (pink), and OIPC (green) for daily, weekly and monthly amount weighted $\delta^{18}O$ values. The OIPC was compared for the monthly time series only. One-to-one line (black) is shown for reference.............72

Figure 4-4: Eigenspectrum for daily, weekly, and monthly amount weighed $\delta^{18}O$ (blue) and δD (red) values of IsoGSM. Colored circles represent significant paired oscillatory or trend components. Solid line represents red noise floor and dashed lines correspond to 97.5 and 2.5% confidence bounds. The embedding dimension was 10 years for each time series (3650 days, 520 weeks, or 120 months)....................74

Figure 4-5: Significant eigenvectors from SSA analysis of daily, weekly, and monthly IsoGSM time series. The first five pairs of eigenvectors represented the largest portion of variance for daily and weekly time series. Only the first pair of eigenvectors was considered significant for the monthly time series the remainder of the eigenvectors were near significant (grey)..76

Figure 4-6: Eigenspectrum for daily, weekly, and monthly amount weighed $\delta^{18}O$ (blue) and δD (red) time series of IsoRSM. Colored circles represent significant paired oscillatory or trend components. Solid line represents red noise floor and dashed lines correspond to 97.5 and 2.5% confidence bounds. The embedding dimension was 10 years for each time series (3650 days, 520 weeks, or 120 months)....................77

Figure 4-7: Significant eigenvectors from SSA analysis of daily, weekly, and monthly $\delta^{18}O$ IsoRSM time series. The first five pairs of eigenvectors represented the largest portion of variance for daily and weekly time series. The first three pairs of eigenvectors were considered significant for the monthly time series. Eigenvectors in grey were not statistically different from the red noise spectrum but considered important components of the time series...78

Figure 4-8: Eigenspectrum for daily and weekly amount weighted $\delta^{18}O$ (blue) and δD (red) time series of SSHCZO. Colored circles represent significant paired oscillatory or trend components. Eigenvalues labeled with star (*) correspond are single eigenvectors and not part of a pair. Solid line represents red noise spectrum and dashed lines correspond to 97.5 and 2.5% confidence bounds. The embedding dimension was 2 years for each time series (730 days or 104 weeks)............................79

Figure 4-9: Major eigenvectors from SSA analysis of daily and weekly $\delta^{18}O$ time series for SSHCZO. Blue eigenvectors were considered statistically significant and fell above the red noise confidence bounds. Grey eigenvectors were not statistically significant but considered important to the time series. 80

Figure 4-10: Reconstructions of weekly amount weighted $\delta^{18}O$ values for SSHCZO (blue) and IsoRSM (grey) using major eigenvectors (see text). Upper panel shows long-term reconstruction of IsoRSM in relation to SSHCZO time series. Lower panel shows agreement between SSHCZO and IsoRSM reconstructions. SSHCZO reconstruction accounts for 51.78% of the variability of the original time series while IsoRSM reconstruction accounts for 43.44% of the variability.................. **82**

LIST OF TABLES

Table 2-1: Installed suction cup lysimeter depths and corresponding soil horizons for Transects 1-3, based on in situ observations (Lin, 2006). The soil horizons for Transect 4 were identified by Jin et al., (2010). Organic Oe-horizon covers the upper ~5 cm of the entire catchment. Lysimeters located in the A-Horizon are colored green, B-Horizon yellow, C-Horizon red, and in bedrock (R) brown. Locations with two lysimeters are labeled A and B after lysimeter depth. **14**

Table 3-1: Subset of complete precipitation dataset for analysis of effects of bandwidth selection and precipitation amount weighting on one-dimensional and two-dimensional kernel density estimations (**Figure 3-3** and **Figure 3-4**)............................ **43**

Table 3-2: Statistics of local meteoric water lines based on different integration periods and the amount-weighted least squares regression. T-test significance is for the difference in slope between the amount-weighted least squares regression and a given integration period.. **59**

Table 4-1: Summary statistics for comparisons of SSHCZO daily, weekly, and monthly amount weighted values against IsoRSM, IsoGSM, and OIPC. **73**

ACKNOWLEDGEMENTS

First off, I would like to sincerely thank Professor Christopher Duffy for providing the opportunity to learn and develop as a scientist over the past two years as well as for his encouragement and assistance through the challenges of research and graduate school. I believe our captivating weekly discussions were where I learned the most about hydrology, research, academia, and professional life. I would also like to thank Professor Henry Lin for his interest in my work and valuable support over the past year and half. He too directly guided my development as a scientist and stirred an interest in catchment hydrology that otherwise would have likely remained dormant. I also thank Professor Michael Gooseff for his valuable insight to my thesis and contributing to the scientific impact of the work.

I thank George Holmes for his efforts to get the isotope hydrology project at SSHCZO off the ground. His time spent installing field instruments, collecting thousands of water samples, implementing the isotopic analyzer, managing results, and passing knowledge on to me has allowed me to quickly and successfully begin my own Masters work. I would also like to thank all of those who have helped with various field work and contributed to the data within this thesis: Ryan Jones, Laurie Eccles, Lixin Jin, Danielle Andrews, Jennifer Williams, Colin Duffy, Andrew Neal, and numerous others.

I would also like to express my gratitude to the Duffy research group: Lorne Leonard, Xuan Yu, Yu Zhang, Pam Sullivan, Gopal Bhatt, and Lele Shu for their help with various CZO tasks. Their experiences and knowledge has increased my productivity and ultimately allowed to me becoming a better researcher. I thank all those in the Water Resources Engineering graduate student office for their patience with my Matlab questions and making the office a generally enjoyable environment.

Finally and most importantly, I would like to thank my family for their support over the past two years. I thank my parents for their love, support, and encouragement as I continued my studies away from home. I also thank Emily for her resolve, patience, support, and even her feigned interest in my scientific endeavors. Not only have I learned a great deal of hydrology during my time here in Pennsylvania, but also I have learned the importance of friends and family.

Chapter 1.

Introduction

1.1. Background

Nearly all terrestrial life on the planet depends on the ecosystem services provided by the Critical Zone, a dynamic system of earth's near surface acting as the nexus of the pedosphere, atmosphere, biosphere, and hydrosphere (Brantley et al., 2007; Anderson et al., 2008). Unfortunately, anthropogenic forces are now applying significant stresses and pressures around the global, generating an urgent need for a better understanding of this complex system (National Research Council, 2001). Further complicating the scenario, the dynamics of Critical Zone exist over a large range of spatial and temporal scales, from tectonic activity, chemical weathering and drainage network development over large regions taking millennia to fluid transport and ion exchange in soil pore spaces acting on the order of seconds or microseconds. Often associated with these processes are feedbacks and process interactions, which can be difficult to understand without interdisciplinary efforts. Progress has been made by various disciplines including soil scientists (Wilding and Lin, 2006), hydrologists (Kirchner, 2003; Lin et al., 2006a; McDonnell et al., 2007), geochemists (Anderson et al., 2007), and ecologists (Brooks et al., 2009) on various processes yet further work is required to fully understand the complexities of the Critical Zone.

In 2006, the Susquehanna-Shale Hills Critical Zone Observatory (SSHCZO) was established to further the understanding of Critical Zone processes and to ultimately understand regolith formation, evolution and function including hydrologic flow paths and timescales (Brantley et al., 2007; Anderson et al., 2008). SSHCZO provided an excellent opportunity to further environmental research due to its proximity to the Penn State campus and because of the previous hydrologic work accomplished at the site (Nutter, 1964; Lynch, 1976; Duffy, 1996). Located in the Ridge and Valley Physiographic Province of eastern United States, SSHCZO has the added benefit of being a classic headwater basin of the Chesapeake Bay watershed (Figure 1-1), with work potentially contributing to the Chesapeake Bay Program and other related projects.

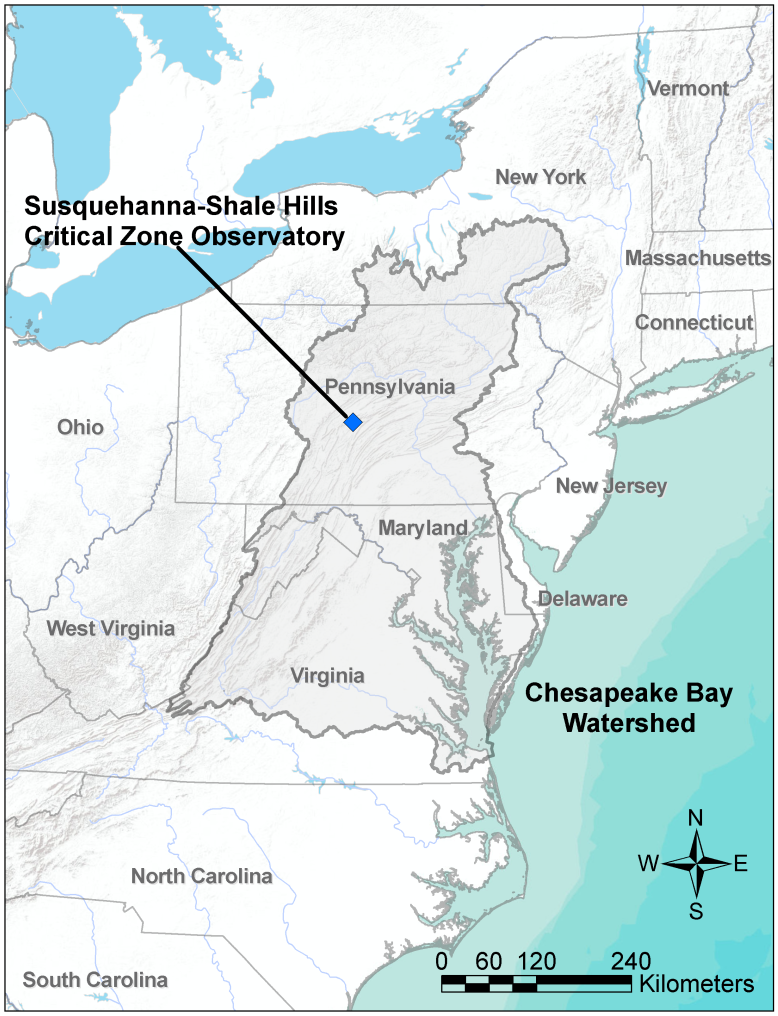

Figure 1-1: Location of Susquehanna-Shale Hills Critical Zone Observatory in relation to the Chesapeake Bay watershed.

Numerous hydrologic studies at the catchment allowed researchers to build off previous findings (Nutter, 1964; Lynch, 1976; Duffy, 1996). Early work established the importance of antecedent soil moisture to quickflow and total storm runoff (Lynch, 1976). More recent works have made substantial progress with respect to soil moisture dynamics (Lin, 2006; Lin et al., 2006b), preferential flow pathways (Lin and Zhou, 2008; Graham and Lin, 2011), and solute transport (Jin et al., 2010, 2011; Andrews et al., 2011; Kuntz et al., 2011; Jin and Brantley, 2011). Additionally extensive distributed hydrologic modeling using the Penn State Integrated Hydrologic Model (PIHM) has successfully detailed the importance of antecedent soil moisture, topographic controls of connectivity, saturated/unsaturated storage dynamics, and isotopic age distributions (Duffy, 1996; Qu and Duffy, 2007; Bhatt, 2012).

To better grasp the driver of many complex environmental processes, research has focused on development of a conceptual hydrologic model. Jin et al. (2011) used water stable isotopes and Magnesium concentrations on one planar hillslope in SSHCZO to better understand surface and subsurface hydrologic processes. Their findings suggest the prevalence of three types of water: low flow waters in the A and B horizons with high Mg concentrations, high flow waters with low Mg concentrations, and groundwater with high Mg concentrations. They also found residence times within the catchment were relatively short, typically less than one year. The work of Holmes (2011) further refined the estimates of residences times within SSCHZO by using a piecewise constant input isotopic age model. His findings suggest the mean age of the water in the catchment reached a peak of 9 months during the summer drought and a minimum of 4.5 months during the winter with an average of 5-6 months. Bhatt (2012) further refined the estimates of isotopic age at SSHCZO by using a spatially distributed, multi-process numerically based model equipped with transport equations. His results showed the space-time average isotopic age for the catchment was 217 days or 7.2 months and varied from 85 days to 347 days. His estimates correspond to an age for the integrated depth of water over all grid cells in the catchment. All results of the previous studies demonstrate the transient nature and complexity of hydrology at SSHCZO.

1.2. Water Stable Isotope Overview

One promising tool at SSHCZO is the use of stable isotopes of water (oxygen-18 and deuterium (^{2}H)) as natural tracers to determine water flowpaths and hydrologic process timescales. Because stable isotopes move with the water molecule itself, they allow for nondestructive, long-term monitoring of subsurface hydrologic processes (Vanclooster et al., 2005; Leibundgut et al., 2009). Over the past decades, water stable isotopes have been used successfully to determine groundwater recharge rates (Gat, 1971; Darling and Bath, 1988; Davisson and Criss, 1993; Criss and Davisson, 1996; Winograd et al., 1998), hydrograph separation (Sklash et al., 1976; Sklash and Farvolden, 1979; Pearce et al., 1986; Rice and Hornberger, 1998), preferential flow paths (McDonnell, 1990; Leaney et al., 1993; Kirchner, 2003; Vogel et al., 2010), soil water evaporation (Zimmermann et al., 1968; Barnes and Allison, 1983, 1988; Gazis and Feng, 2004), and sources of transpired water (Dawson and Ehleringer, 1991; Ehleringer and Dawson, 1992; Brooks et al., 2009; Gierke, 2012).

Stable isotope hydrology dates back nearly 80 years with the discovery of seawater being isotopically heavier than fresh waters (Gilfillan, 1934). Unfortunately, soon after this discovery, World War II forced researchers to devote efforts towards more defense-minded endeavors, including the development of mass spectrometry. After the war, researchers equipped with these new laboratory methods began to analyze natural abundances of oxygen-18 and deuterium in meteoric waters around the globe and started to explain the underlying physics controlling the abundances (Epstein and Mayeda, 1953; Friedman, 1953; Dansgaard, 1954). Efforts to summarize and standardize global results (Craig, 1961a; b) laid the framework for future isotopic studies by formally establishing a linear relationship between concentrations of oxygen-18 and deuterium and defining a standard for use globally. In 1961, Craig was the first to propose development of Standard Mean Ocean Water (SMOW) which then allowed samples to be compared against each other (Craig, 1961a), simplifying analysis and promoting world wide investigation of isotope hydrometeorology. Standard isotope notation follows the form:

$$\delta_X(permil) = \left(\frac{R_X}{R_{SMOW}} - 1\right) \times 1000 \qquad (1)$$

where R is the ratio of deuterium (^2H) to hydrogen (H) or ^{18}O to ^{16}O in the standard (X) or Standard Mean Ocean Water (SMOW). Delta values are multiplied by 1000 for convenient comparisons of samples. Over time SMOW has undergone revisions to more precisely establish a world wide standard for isotopic composition of ocean water, the most recent revision occurring in 2009 with the development of V-SMOW2 or Vienna Standard Mean Ocean Water 2 (International Atomic Engery Agency, 2009).

The International Atomic Energy Association (IAEA) was also influential in the coordination of an observation network intended to monitor oxygen-18, deuterium, and tritium concentration spatial and temporal patterns across the globe. In 1964, Dansgaard thoroughly detailed the preliminary results of the IAEA's network and outlined the geochemical processes governing them (Dansgaard, 1964). He found empirical relationships relating precipitation isotope compositions to physical and environmental parameters such as surface temperatures, latitude, distance from coast, and amounts of precipitation. Later studies supported his findings (Gat and Gonfiantini, 1981; Rozanski et al., 1993). The empirical relationships can be thought of as representing the degree of rainout and associated isotopic depletion as the air mass is transported from its source area to the site of precipitation. That is to say, the isotopic composition of precipitation contains information regarding the history of a given air mass and the associated atmospheric circulation patterns. The isotopic composition of precipitation is controlled by the interaction of four main factors: the meteorological (e.g. temperature, humidity) conditions at the source area, the fraction of available moisture, snow formation or evaporation of liquid from falling droplet, and mixing of different air masses (Gat, 1996; Araguás-Araguás et al., 2000). Much of these factors may vary seasonally leading to seasonal variation in isotopic compositions for a given site.

Deuterium and oxygen-18 compositions of precipitation have been found to vary linearly at the global (Craig, 1961b; Rozanski et al., 1993; Araguás-Araguás et al., 2000) and regional scales (Fritz et al., 1987; IAEA, 1992). Refining Craig's (1961b) initial estimate of the Global Meteoric Water Line (GMWL: $\delta D = 8\ \delta^{18}\mathrm{O} + 10$ ‰), Rozanski et al. (1993) found the GMWL based on long term amount weighted means of 205 observation points to be:

$$\delta D = 8.17\ (\pm 0.07)\ \delta^{18}\mathrm{O} + 11.27\ (\pm 0.65)\ ‰ \qquad (2)$$

The GMWL can be though of as a composite of many local meteoric water lines (LMWL) from different locations or regions. Deviations from the GMWL are due to evaporative processes which influence the d-excess value (d-excess = $\delta D - 8\ \delta^{18}\mathrm{O}$, originally defined by Dansgaard (1964)), and is commonly found in arid or semi-arid environments. Typically LMWLs for arid or semi-arid regions have slopes less than 8. Slopes larger than 8 are possible in locations where depleted precipitation values fall below the GMWL and relatively enriched precipitation has high d-excess values. Locations with large LMWL slopes typically have two or more distinct sources of precipitation (Araguás-Araguás et al., 2000).

1.3. Geospatial Data and Surveying at SSHCZO

Concurrently with much of the isotope hydrology studies performed over the past two year, substantial progress was made surveying and mapping instrumentation at SSHCZO. Because of the scope and complexity of SSHCZO, instrumentation is continually being installed, and thus surveying is required to precisely map relative locations within the catchment. To expedite all future survey efforts, semi-permanent control points were installed and marked throughout the catchment based off permanent monuments installed by a professional surveyor in the summer of 2011. Control points consist of 0.75 inch diameter rebar emplaced in the soil with approximately

2 inches of rebar exposed at each control point to allow for removal if desired. These additional control points now accelerate surveyors ability to quickly setup and gather coordinate data as well as check accuracy in the field.

1.4. Research Objectives and Efforts

There are two general objectives of this thesis: 1) building a robust understanding of water stable isotopes at the SSHCZO and 2) developing a high-resolution dataset of isotopes in precipitation for future implementation into the Penn State Integrated Hydrologic Model (PIHM) and HydroTerre. Ideally, with the knowledge gained through work on the first objective, an improved data product will be developed for the second objective.

Chapter 2 partially addresses the first objective through in-depth investigation of the spatiotemporal patterns of soil water isotope compositions at SSHCZO. The motivation behind investigating soil water isotope compositions was to to improve our understanding of subsurface hydrologic processes and supplement the overall conceptual hydrologic model. The relationship between soil water, precipitation, and groundwater isotope compositions is also discussed briefly in the second chapter. Chapter 3 continues to addresses the first general objective of building a robust understanding of water stable isotopes at SSHCZO by more closely examining temporal patterns of precipitation stable isotope compositions. The results from this work are intended to support the development of the data product in Chapter 4 as well as to support any future isotope hydrology studies at SSHCZO or nearby sites.

The second main objective was addressed in Chapter 4. Knowledge from the previous chapters was applied to the comparison of observed isotopic composition of SSHCZO precipitation to two related isotope-incorporated atmospheric general circulation models. It is intended that with a valid comparison, the results from one isotope-incorporated atmospheric general circulation models would suffice as the initial data product for isotopes in precipitation for the Chesapeake Bay watershed. The comparison was performed using standard regressions and singular spectrum analysis. With the results of the comparison, a 32-year record of isotopes in precipitation was established for SSHCZO. Future work includes validation of the isotope incorporated atmospheric general circulation model at other spatial locations and the development of a usable data layer for PIHM implementation.

Chapter 2.

Spatiotemporal Patterns of Stable Isotope Compositions at the Shale Hills Critical Zone Observatory: Linkages to Subsurface Hydrologic Processes

This chapter has been submitted in similar form to the Vadose Zone Journal, with co-authors H. Lin, C. Duffy, P. Sullivan, G. Holmes, S. Brantley, and L. Jin.

2.1. Abstract

To better understand flow pathways and patterns in the subsurface, a stable isotope monitoring network was established at the Shale Hills Critical Zone Observatory. Soil water samples were collected approximately bi-weekly using suction-cup lysimeters installed at multiple depths along four different transects in the catchment. Groundwater and stream water were collected daily using automatic samplers, while precipitation samples were collected automatically on an event basis. Our over 3-year (2008-2012) monitoring data showed strong seasonal precipitation isotope composition, which was imprinted in seasonal patterns of various hydrologic pools. The groundwater isotope composition remained relatively constant throughout the year and closely matched the yearly amount-weighted precipitation average, suggesting groundwater received recharge water in each season, although recharge mechanisms differed between growing and non-growing seasons. Soil water samples showed strong seasonal trends in isotopic composition and clear attenuation with depth, with the variation in shallow soil water closely mirroring precipitation inputs, while deep soil water matched the groundwater average. Spatial patterns showed that snowmelt infiltrated the A-Horizon on the northern slope but sublimated from the southern slope. Soil water isotope composition profiles provided evidence for preferential flow occurring laterally and vertically at various points and times in the catchment.

2.2. Introduction

Knowledge of subsurface flowpaths and timescales is essential to the understanding of soil formation and hydrologic processes in the Critical Zone. Soil water plays an essential role by transporting major constituents important for terrestrial ecosystem services including carbon, nitrogen, and other nutrients, chemical weathering products, sediments, and possible contaminants. Furthermore, soil water acts as the linkage between precipitation and groundwater, facilitating recharge and dictating when subsurface flow occurs. As anthropogenic forces continue to stress the environment, it becomes more important to understand this linkage and transport processes within the vadose zone. Stable isotopes of water provide an important environmental tracer for understanding vadose zone hydrology, groundwater recharge, mixing processes, stream flow generation, subsurface storage, and catchment yield (Vanclooster et al., 2005; Leibundgut et al., 2009).

Water stable isotopes (deuterium and oxygen-18) allow for nondestructive, long term monitoring of subsurface hydrology. Stable isotopes have been used to determine groundwater composition and recharge rates (Gat, 1971; Darling and Bath, 1988; Davisson and Criss, 1993; Criss and Davisson, 1996; Winograd et al., 1998), preferential flow pathways and the old water-new water paradox (McDonnell, 1990; Leaney et al., 1993; Kirchner, 2003; Vogel et al., 2010), soil water evaporation (Zimmermann et al., 1968; Barnes and Allison, 1983, 1988; Gazis and Feng, 2004), hydrograph separation (Sklash et al., 1976; Sklash and Farvolden, 1979; Rice and Hornberger, 1998), and tree water source (Ehleringer and Dawson, 1992; Brooks et al., 2009; Gierke, 2012).

The Susquehanna-Shale Hills Critical Zone Observatory (SSHCZO) was established in 2007 in order to determine regolith formation and evolution as well as hydrologic flowpaths and timescales within a small, forested catchment. To date, many successful studies have identified the importance of hydrological processes including soil moisture dynamics (Lin, 2006; Lin et al., 2006b; Lin and Zhou, 2008), solute transport (Jin et al., 2010, 2011; Andrews et al., 2011; Kuntz et al., 2011), and stream flow generation mechanisms (Lynch, 1976; Duffy, 1996). Additionally, water stable isotopes have been used along with other chemical tracers to conceptualize catchment hydrology (Holmes, 2011; Jin et al., 2011). Jin et al. (2011) used variations in Mg concentrations and water stable isotopes to identify three types of water storage within the south planar hillslope of the SSHCZO: low-flow waters where chemical dissolution occurs, high-flow waters where residence times are low, and groundwater storage in fractured shale bedrock. Their findings indicate typically low-flow waters are stored within soil matrix, high-flow waters are found at interfaces of low permeability, and groundwater is found continually in the valley floor.

In addition, Jin et al. used the water isotopes to estimate that residence times of waters in the catchment are less than a year, indicating the fast nature of draining of the hillslopes.

Preferential flow pathways have been found to be prominent in the catchment (Lin, 2006; Lin and Zhou, 2008; Graham and Lin, 2011; Jin et al., 2011). Analysis of 175 precipitation events over three years by Graham and Lin (2011) showed that preferential flow occurred during at least 90% of the events. While these studies have successfully conceptualized the subsurface hydrology at the SSHCZO, water isotopes have not yet been used to investigate the temporal and spatial patterns of subsurface hydrologic processes across the catchment.

The goal of this study is to determine the spatial and temporal drivers of subsurface hydrology utilizing high frequency sampling of water stable isotopes. Specifically, we will examine the influence of hillslope orientation, slope location, landform type, and soil depth on soil water isotope compositions to determine water flowpaths associated with specific soil or landscape features. We aim to improve the understanding of temporal patterns of water isotope compositions involving: seasonal differences (growing vs. non-growing), snowmelt dynamics, and periods of water scarcity. Finally, this study will help improve the understanding of mechanisms involved in controlling spatiotemporal patterns of soil water isotope composition, growing season evaporation patterns, and subsurface preferential flow.

2.3. Methods & Materials

2.3.1. Site Description

2.3.1.1. Landform and Vegetation

The SSHCZO, a 7.9-ha forested catchment located in central Pennsylvania, is characteristic of the Ridge and Valley Physiographic Province of eastern United States. The V-shaped, headwater catchment is oriented east-west and contains an intermittent 1st order stream that typically flows from late September to early June. The SSHCZO lies within the Shavers Creek watershed of the Juniata River, which in turn is a sub-basin of the Susquehanna River. Slopes within the catchment are considered moderate and range from 25-48%, with elevation varying from 310 m at the ridge top to 256 m at the stream outlet (Lin, 2006). The strike and dip of the underlying shale bedrock are approximately N54°E and 76°NW, respectively, as measured in the northern ridge top (Jin et al., 2010) but shallower dip has been measured near the valley floor (Kuntz et al., 2011).

There are four distinct landform units within the catchment: north (south-facing) slope with deciduous forest and underbrush, south (north-facing) slope with deciduous forest and thicker underbrush, valley floor with evergreen (hemlock) trees along the western side and deciduous oak-hickory forest on the eastern side, and topographic depressional areas (swales) with deciduous forest cover and deeper soils. There are seven swales distributed over the catchment, with five on the north slope and two on the south slope, each separated by near-planar slopes. The catchment was clear-cut approximately 60 years ago and the current mature forest is composed of deciduous trees on the slopes and ridges (Maple [*Acer spp*.], Oak [*Quercus spp*.], and Hickory [*Carya spp*.]) and eastern hemlock conifers on the valley floor (*Tsuga Canadensis* [L. Carriere]).

2.3.1.2. Soils

The soil survey shows that soils in this catchment were formed from shale residuum or colluvium and contain many channery shale fragments throughout most of the soil profiles (Lin et al., 2006b). Hillslope soils have silt loam texture in general, moderately developed soil structure, and are generally well drained. In the valley floor, there are redoximorphic features starting to appear at 30-60 cm in soil profiles. Throughout the catchment there is about 0.05 m thick organic layer (Oe-horizon) (Lin et al., 2006b). There are five distinct soil series that are distinguished based on depth to bedrock, landform unit, and drainage condition (Figure 2-1). The Weikert series is the most prevalent soil type (loamy-skeletal, mixed, active, mesic Lithic Dystrudepts) and is generally < 0.5 m thick to bedrock. The Berks soil series (loamy-skeletal, mixed, active, mesic Typic Dystrudepts) is 0.5-1 m thick to bedrock. The Rushtown series (loam-skeletal over fragmental, mixed, mesic Typic Dystrochrepts) is located in the center of swales as well as in the eastern end of the catchment and is >1 m thick to bedrock. Soil series located on the valley floor are distinguished by fragipan-like layer and depth to redox features. The Ernest series (fine-loamy, mixed, superactive, mesic, Aquic Fragiudults) occupies the majority of the streambed and contains redox features starting at 0.3-0.5 m. The Blairton series (fine-loamy, mixed, active, mesic Aquic Hapludults) is of minor extent and contains redox features at > 0.6 m depth. Further information regarding the soil survey and features can be found in Lin et al. (2006). Specific soil characteristics, weathering reactions, soil chemistry and mineralogy have been previously reported for the locations of the lysimeter nests described herein (Jin et al., 2010; Jin and Brantley, 2011).

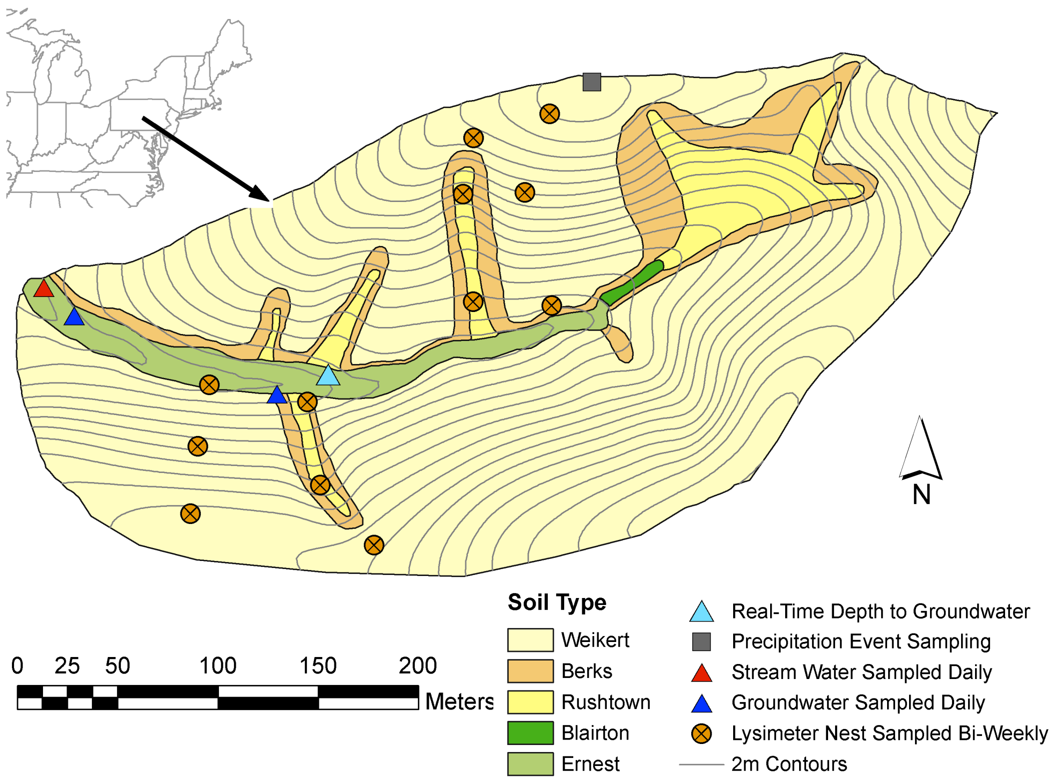

Figure 2-1: Topographic map of Susquehanna-Shale Hills Critical Zone Observatory with stable isotope monitoring instruments. Colors indicate soil type based on field observations (Lin et al., 2006). Ten-minute precipitation amounts and event-based water samples were collected at the ridge top clearing (grey box) for isotope analysis. Soil water was collected bi-weekly at four nested lysimeter transects (orange circles) as described by Jin et al., (2011). Two unscreened groundwater wells were installed in the stream riparian zone to observe daily evolution of isotope composition (dark blue triangles). Depth to groundwater table was monitored in real-time in the stream riparian zone (teal triangle). Stream discharge and isotope composition values were monitored daily at the double V-notch weir located at the stream outlet (red triangle).

2.3.1.3. Climate

The SSHCZO is located in a humid climate where the long-term average precipitation of 1,006 mm is approximately evenly distributed throughout the year. Mean annual temperature is 10.1°C. Summers are typically hot and humid with temperatures >30°C and precipitation events consisting of short, high-intensity storms. Winters are typically wet and cold with temperatures less than -10°C and precipitation events consisting predominantly of snow (based on a 30-year record, NOAA, 2007).

2.3.2. Data Collection

2.3.2.1. Hydrologic Monitoring

Meteorological data were collected in a small clearing area at the ridge top of the catchment from 2009-2012. Precipitation was monitored using an Ott-Pluvio weighing bucket (Hach Company, Loveland, CO) in ten-minute intervals with a precision of 0.1 mm and Laser Precipitation Monitor (LPM, Thies Clima, Göttingen, Germany) in ten-minute intervals with precision of 0.01 mm. The LPM is capable of determining the type of precipitation (e.g., drizzle, rain, snow, or hail) based on the size and velocity of the precipitation. Data were collected and transmitted on-line in real time and processed annually for missing data. Missing data were filled directly using 16 tipping-bucket rain gages with HOBO recorders (Davis Instruments Corp., Hayward, CA) located throughout the catchment and the LPM. The tipping-buckets record rainfall at a height of 0.3 m with a precision of 0.2 mm. Because the tipping buckets were typically located under the canopy and only collected throughfall, these data were used only when necessary.

A double V-notch weir located at the outlet of the stream was used to monitor stream discharge accurately during high and low flows. Water depths were recorded in one-minute intervals, integrated to daily values and converted to discharge using a rating curve developed by Nutter (1964). Depth to groundwater was monitored at one well in the stream riparian zone from Jan. 2009 to Dec. 2011 in ten-minute intervals using Druck pressure transducers (Campbell Scientific Inc., Logan, UT) (Figure 2-1).

2.3.2.2. Stable Isotope Monitoring

From Jun. 13, 2008 to Mar. 16, 2012, a total of 4,460 unfiltered water samples were collected over the entire catchment to determine the isotopic composition of various hydrologic pools and their linkages. Precipitation samples were collected Jan. 14, 2009 to Feb. 12, 2012 on an event basis using an automatic precipitation sampler (model: NSA 181/S, Eigenbrodt GmbH & Co., Königsmoor, Germany) located in the clearing area on the ridge top (Figure 2-1). To capture intra-storm variability, precipitation was collected for the first 30-minutes of a storm followed by three 6-hour intervals. Precipitation amount and isotope composition were assumed to be consistent over the entire catchment. Previous studies in central Pennsylvania have shown that one rain gage per 12.6 km^2 is suitable to resolve spatial variability of precipitation (Reich, 1966; O'Driscoll et al., 2005). As isotopic enrichment of summer precipitation associated with throughfall (0.11‰ and 2.9‰ for $\delta^{18}O$ and δD, respectively Pearce et al., 1986) is similar to analytical precision; thus the isotopic composition of throughfall was assumed to be equal to the composition of the sampled precipitation.

Daily stream water and groundwater samples were collected using automatic samplers (2700 series, Teledyne Isco, Lincoln, NE). Stream water was sampled directly upstream of the weir from Mar. 2009 to Mar. 2012. Groundwater was collected from Mar. 2009 to Mar. 2012 at two screened wells (approximately 3 m deep), located in the stream riparian zone (shown in Figure 2-1).

As reported originally by Jin et al., (2011) soil water samples were collected approximately every two weeks from four transects of nested suction-cup lysimeters (48 mm diameter, SoilMoisture 1900 series, Soil Moisture Inc., Santa Barbara, CA) emplaced in 2006 (Figure 2-1 and Table 2-1). Jin et al., (2011) only report samples from the south planar hillslope of the catchment collected from 2006 to 2010. That same dataset is extended here through 2011 and includes samples from the north side of the catchment and swale transects. Soil water sampling was often limited during the summer (Jun.-Sep.) due to low soil water content and in the winter (December-March) due to frozen soil matrix and snow cover. Soil water samples were collected according to established USGS protocols (White et al., 2005) as described previously by Jin et al., (2011). Lysimeters were suctioned to 50 kPa one week prior to sampling and thus only collected mobile water within the soil matrix. The four transects of lysimeters were located along a swale and a planar hillslope each along the south and north slopes (Jin et al., 2010, 2011). Each transect contained lysimeter nests at three locations along the topographic gradient: ridge top, midslope, and valley floor. The midslope and valley floor of swales were dominated by Rushtown soils while ridge tops and planar slopes were dominated by Weikert soils (Figure 2-1) (for soil chemistry and mineralogy see Jin et al. (2010) and Jin and Brantley (2011). Each nest consisted of 3 to 13 lysimeters (depending on soil thickness) installed at 10 cm interval depths and spaced 10 cm apart (Table 2-1). The first lysimeter was installed at a depth of 10 cm with subsequent lysimeters added until the point of augering refusal.

Table 2-1: Installed suction cup lysimeter depths and corresponding soil horizons for Transects 1-3, based on in situ observations (Lin, 2006). The soil horizons for Transect 4 were identified by Jin et al., (2010). Organic Oe-horizon covers the upper ~5 cm of the entire catchment. Lysimeters located in the A-Horizon are colored green, B-Horizon yellow, C-Horizon red, and in bedrock (R) brown. Locations with two lysimeters are labeled A and B after lysimeter depth.

Transect 1: North (South-Facing) Swale Depression					
Ridge Top		Midslope		Valley Floor	
Soil Series: Weikert		Soil Series: Rushtown		Soil Series: Rushtown	
Depths (cm)	Soil Horizon	Depths (cm)	Soil Horizon	Depths (cm)	Soil Horizon
10	A	10	A	10	A
20	Bw	20	Bw2	20	Bw2
30	CR	40	BC	40	BC
40	R	60	BC	60	BC
		80	C	80	C
		100	C	100	C
		140A/140B	C	140	C
		180	C	180	C
		220	C	220	C
		260	C	260	C
		300	C	300	C
		340	C	340	C

Transect 2: North (South-Facing) Planar Hillslope					
Ridge Top		Midslope		Valley Floor	
Soil Series: Weikert		Soil Series: Weikert		Soil Series: Berks	
Depths (cm)	Soil Horizon	Depths (cm)	Soil Horizon	Depths (cm)	Soil Horizon
10	A	10	A	10	Bw1
20	Bw	20	Bw	20	Bw2
30	CR	30	CR	30	Bw2
40	R	40A/40B	R	40	Bw2
		50A/50B	R	50	Bw2
		60	R	60	Bw3
		160	R	70	C
		220	R	80	C
				100	C
				120	C

Transect 3: South (North-Facing) Swale Depression					
Ridge Top		Midslope		Valley Floor	
Soil Series: Weikert		Soil Series: Rushtown		Soil Series: Rushtown	
Depths (cm)	Soil Horizon	Depths (cm)	Soil Horizon	Depths (cm)	Soil Horizon
10	A	20	Bw2	10A/10B	A
20	Bw	40	BC	20	Bw2
30	CR	60	BC	30	Bw3
		80	C	40	BC
		100	C	50	BC
		120	C	60	BC
		140	C	70	C
		160	C	80	C
				90	C

Transect 4: South (North-Facing) Planar Hillslope					
Ridge Top		Midslope		Valley Floor	
Soil Series: Weikert		Soil Series: Weikert		Soil Series: Ernest	
Depths (cm)	Soil Horizon	Depths (cm)	Soil Horizon	Depths (cm)	Soil Horizon
10	A	10	A	10	A
20	B	20	Bw	20	AE
30	C	30	CR	30	Bt
		40	R	40	Bt
		50	R	60	2C

All liquid water samples were collected and stored in 30 mL amber glass vials with cone-lined caps to prevent evaporation. Sample bottles contained little or no headspace to minimize water-air exchange. Water samples were analyzed using laser absorption spectrometer (DT-100 Liquid Water Isotope Analyzer, Los Gatos Research, Inc., Mountain View, CA) following the IAEA Standard Operating Procedure (Newman et al., 2008). The analytical precision of the instrument is 0.1‰ and 0.8‰ for oxygen-18 and deuterium, respectively (Lis et al., 2008). The isotopic composition of the water was reported as a δ-value relative to Vienna Standard Mean Ocean Water (VSMOW):

$$\delta_X(permil) = \left(\frac{R_X}{R_{VSMOW}} - 1\right) \times 1000 \quad (1)$$

where R is the ratio of deuterium to hydrogen or ^{18}O to ^{16}O in the unknown (X) or VSMOW.

2.3.3. Data Analysis

To determine the isotope composition of precipitation for a given time period, the mean precipitation isotope composition was weighted by volume of precipitation and calculated using the following equation:

$$\delta_T = \frac{\sum_{i=1}^{n} P_i \delta_i}{\sum_{i=1}^{n} P_i} \quad (2)$$

where δ_T is the amount-weighted precipitation value, P_i represents the amount (depth) of precipitation in an event, δ_i is the isotope composition of an event, and n is the number of events in the time period considered. To determine temporal variations in isotope compositions and to account for the moderate sampling frequency of lysimeters, samples were averaged into four seasons: spring, summer, fall, and winter. Seasons were defined based on the astronomical calendar rather than the meteorological calendar in order to more closely align with the growing season of the vegetation in the catchment. For example, the spring season begins on the Spring Equinox and ends on the Summer Solstice, dates which vary from year to year. The growing season was defined as the combination of spring and summer while the non-growing season was defined as the combination of fall and winter. This seasonal naming convention remains consistent throughout the study.

Violin plots (Hintze and Nelson, 1998) of the smoothed kernel density distributions were used to examine the isotopic distribution of seasonal precipitation inputs as well as the other hydrologic pools (soil, stream, and groundwater). The size of the violin plot was normalized so the area of each plot was equal to one. For precipitation violin plots, amount-weighted concentrations were calculated as well as two weighted standard deviations. Observations were offset along the x-axis to allow for visualization. For the violin plots of various hydrologic pools, standard box and whisker plots were created. Boxes correspond to the inner-quartile and whiskers correspond to 1.5 of inner-quartile range. Violin plots of soil water were binned into three groups: shallow soil water (≤30 cm depth), intermediate soil water (40-100 cm depth), and deep soil water (≥120 cm depth). This was intended to facilitate the investigation of general soil water isotope composition patterns with respect to depth throughout the entire catchment.

To determine the temporal evolution of soil water isotope composition profiles and the associated uncertainty, the isotopic composition of the soil water was spatially and temporally interpolated using an ordinary kriging method in the MATLAB software package (The MathWorks, Natick, MA). Soil water isotope compositions of lysimeters emplaced at equal depths were averaged for each collection date over all locations and applied to a grid with 1 cm spacing vertically and five-day spacing horizontally. This was done to identify depths or times of either gradual or rapid turnover throughout the catchment. Monthly amount-weighted isotope composition of precipitation along with precipitation amounts were calculated for Jan. 2009 through Dec. 2011 for reference. The color map thus created was applied to discern depth-time patterns of soil water isotope composition in relation to precipitation. Depth to the water table at one location in the stream riparian zone was filtered using a ten-day moving average to reduce noise and was superimposed on the above map to facilitate the investigation of its possible relation to soil water isotopes.

To determine spatial patterns of soil water isotope composition with depth and location in the catchment, various isotope profiles were created. Seasonal profiles were created to separate temporal patterns from spatial patterns. Seasonal groupings were performed following the convention as described above. As described above, lysimeter samples are presented as catchment-averaged profiles, i.e., all sampled lysimeters at equivalent depths throughout the catchment for a given season were averaged to develop a composite average seasonal isotope profile. Isotope profiles were also composited for each hillslope type (swale vs. planar hillslope), slope location (ridge top, midslope, and valley floor), and slope orientation (south-facing vs. north-facing) by averaging soil water collected from equal depths at each location. In other words, for each season we calculated the average isotope composition and standard deviation for each depth (10, 20, 30, etc.) at each location. Because profiles represent general seasonal patterns at given locations, depths with only one observation were removed from profiles to limit misinterpretation. The winter and summer profiles were selected for comparison because the soils are typically the wettest during the winter and the driest during the summer months (Lin, 2006; Lin et al., 2006b). Furthermore, the winter and summer isotope profiles make up the boundaries of the annual isotope profiles, providing the clearest differences in seasonal changes. In each soil water isotope profile, we have estimated representative soil horizons based on each lysimeter nest's location and surveyed soil map and the mapped soil-bedrock interfaces (Figure 2-1 and Table 2-1). This may provide additional insight to the influence of soil horizonation on hydrologic processes and thus on soil water isotope compositions.

2.4. Results

2.4.1. Catchment Hydrology

Annual precipitation amounts were 997.95 mm (2008), 1033.30 mm (2009), 895.56 mm (2010), and 1320.90 mm (2011) as recorded in the rain gauge. During the winters (December-March), the precipitation amounts were 250.67 mm (2008-09), 350.80 mm (2009-10), and 276.70 mm (2010-2011), consisting mostly of snow. Discharge ranged between 0 – 48 L/s, with periods of zero discharge typically occurring between late June and early September. Large discharges (> 20 L/s) occurred immediately after large storms or snowmelt events, after which discharge quickly decreased to < 5 L/s. Patterns of depth to water table mirrored discharge but had a slower rate of change. Rising water tables were associated with large storms and/or snowmelt events but generally were found to relax more slowly than stream discharge. Depth to water table within the stream riparian corridor ranged from 0.36 to 2.26 m during 2009-2011, with the deepest depth (well below the streambed) found at the end of the growing season (late Aug.).

2.4.2. Precipitation Isotope Composition

For the entire study period, the precipitation amount-weighted average isotopic composition was -8.71‰ and -57.35‰ for $\delta^{18}O$ and δD, respectively (Figure 2-2). For monthly averaged samples, the least depleted values were detected in the spring, with progressively more depleted values observed in the summer, fall, and then in the winter. These data compare well to other observations of seasonal differences in precipitation isotope composition (Gat, 1996; Araguás-Araguás et al., 2000). This trend was attributed to the temperature dependent water fractionation associated with phase changes in the hydrologic cycle, including variable temperatures at the moisture source of water, variable temperatures at the precipitation site, and variations in evaporative fluxes throughout the year. The largest seasonal range in the precipitation's isotopic signature occurred in the winter, while the smallest range was observed in the spring. The weighted kernel density distributions (Figure 2-2) indicated that the isotopic composition of the precipitation within each season was normally distributed, yet the aggregated yearly distribution was non-normal, indicating that the impact of seasonality alters the relative frequency.

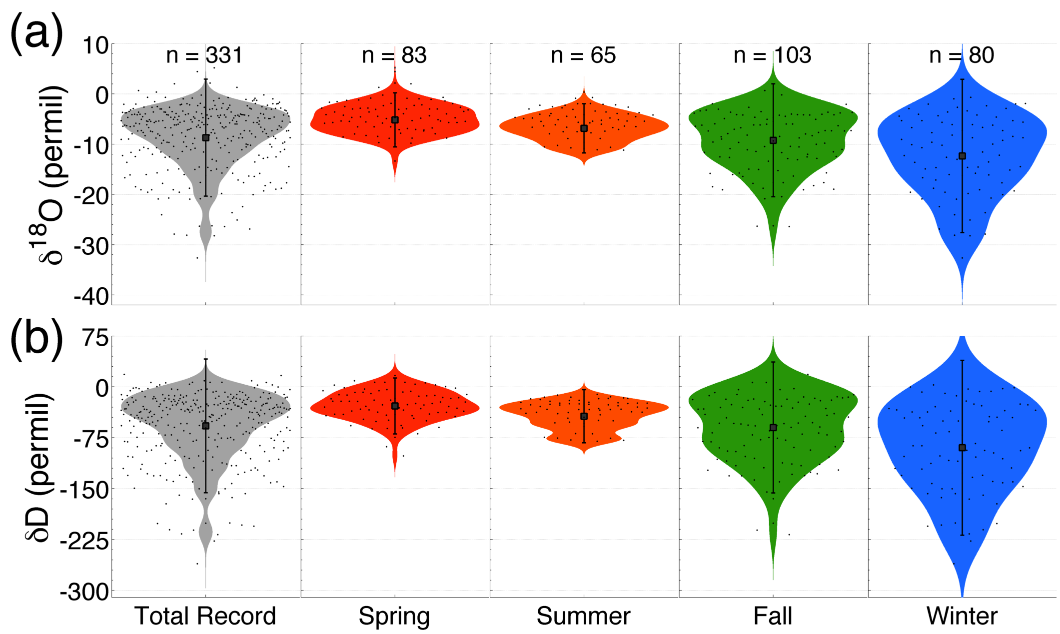

Figure 2-2: Violin plots of the distribution of oxygen-18 (a) and deuterium (b) compositions in precipitation. The plot for the total record consists of precipitation events collected from Jan. 14, 2009 to Feb. 12, 2012, with sample number n indicated. Seasons are divided based on astronomical calendar to more closely correspond to the growing season within the catchment. Colors of the seasons correspond to colors used in seasonal soil water profile figures (**Figure 2-3**, **Figure 2-7**, **Figure 2-8**, and **Figure 2-9**). The shape of the violin plot is the smoothed, weighted kernel density distribution, normalized so the area of each plot is equal to one. The center square is the amount-weighted mean composition and the bars are plus and minus two weighted-standard deviations. Black points are individual data points, jittered horizontally for visualization.

Precipitation records were also analyzed to determine sub-seasonal temporal trends. Although the record contained substantial noise, the time series of individual precipitation sample compositions (Figure 2-3) showed typical seasonal oscillations, with depleted values in the winter months as snow and subsequently less depleted values in the summer months as rain. Unlike daily and monthly amounts of precipitation, weekly amount-weighted isotope compositions (Figure 2-4) showed strong seasonal trends, ranging from -25.80‰ to 1.31‰ for $\delta^{18}O$ and from -200.72‰ to 6.47‰ for δD. Further, the monthly amount-weighted isotope compositions also showed a strong seasonality with much less noise (Figure 2-5).

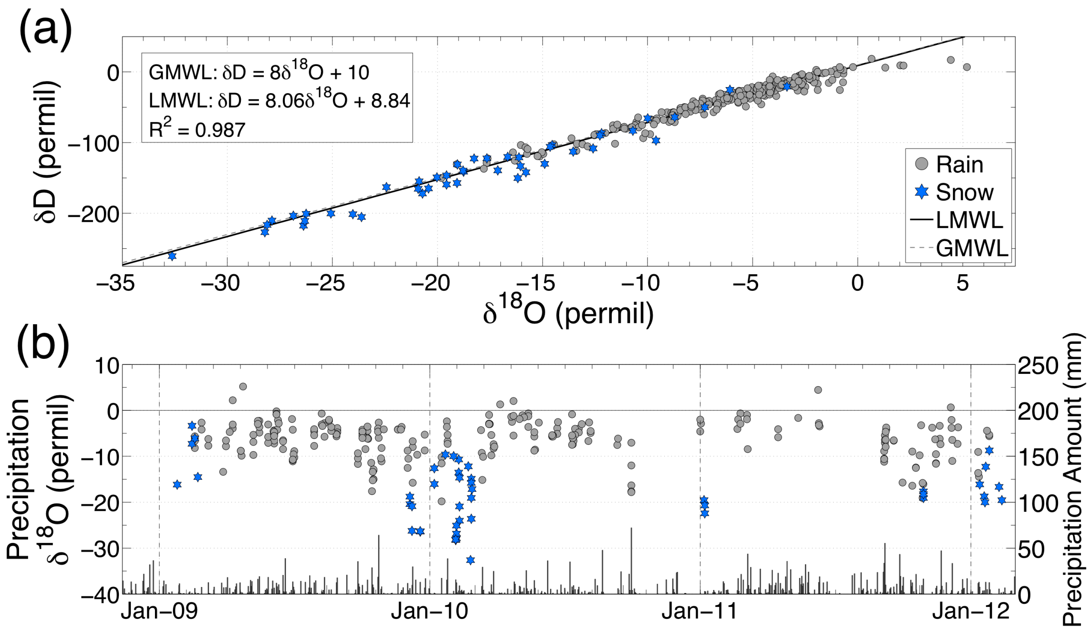

Figure 2-3: A total of 331 precipitation samples collected for isotope composition from Jan. 14, 2009 to Feb. 12, 2012. Precipitation is shown as both rain (grey circles) and snow (blue stars). All samples were collected over six-hour intervals. The local meteoric water line (LMWL, solid line) was calculated using all precipitation samples (a). The global meteoric water line (GMWL, dashed line) is plotted for reference. The time series of $\delta^{18}O$ for all precipitation samples and the daily precipitation record (b) with precipitation grouped into rain and snow.

The Local Meteoric Water Line (LMWL) of the SSHCZO was created using all 331 six-hour precipitation sample composites. The LMWL at the SSHCZO closely matches the Global Meteoric Water Line proposed by Craig (1961) (Figure 2-3), and the smaller intercept of the LMWL (i.e., 8.84) is typical of the slightly more humid climate of central Pennsylvania. Snow (winter precipitation) at the SSHCZO was slightly more depleted than liquid precipitation (non-winter precipitation) but had a larger range in isotopic composition.

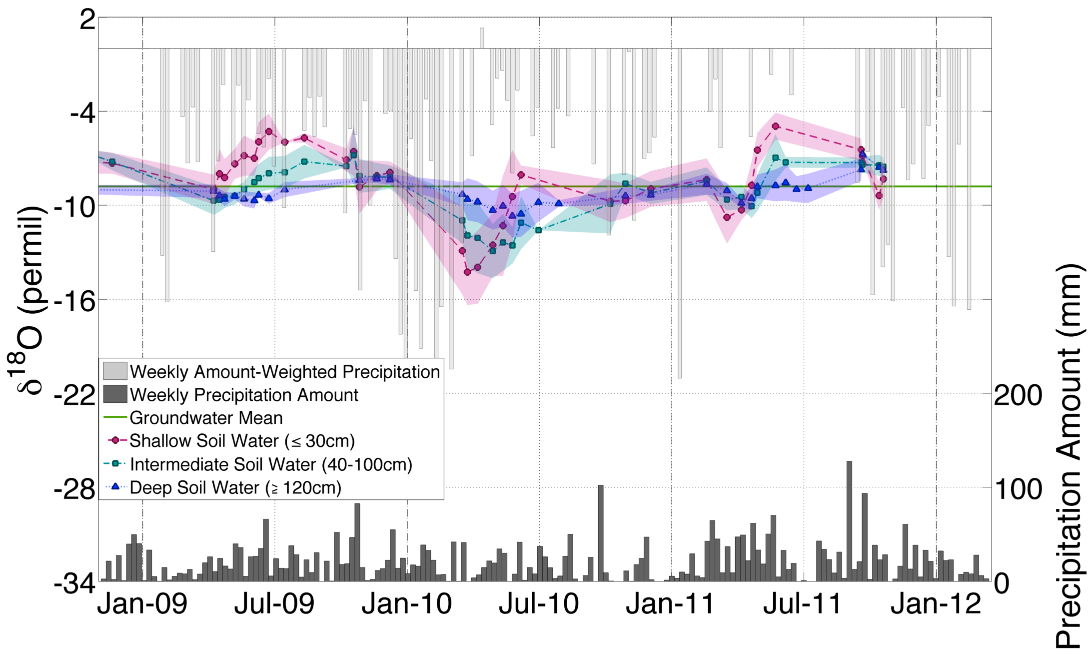

Figure 2-4: Temporal variation in weekly precipitation amount (dark bars), and the isotope composition of precipitation (gray bars) and soil water at three depths (shallow, intermediate, and deep). Soil water data prior to November 2008 are not shown since precipitation record did not begin until January 2009. Shaded regions correspond to one standard deviation of each soil depth. Data for each soil depth is averaged over the entire catchment. Groundwater mean (green line) is shown as a reference.

2.4.3. Depth-Time Variability of Soil Water Isotope Compositions

Aggregation of soil water samples across the entire catchment showed clear pattern of isotope composition attenuation with depth (Figure 2-4 and Table 2-1). The kernel density distribution of isotopic composition of all combined soil water samples was normally distributed (Figure 2-6). Further separation into shallow (≤30 cm), intermediate (40-100 cm), and deep soil water (≥120 cm) indicated the kernel density distributions remained consistently normally distributed. The stream water kernel density distribution had a slight bi-modal distribution, while that for groundwater was normally distributed for $\delta^{18}O$ but bimodal for δD (Figure 2-6). As observed by Jin et al., (2011), for the smaller dataset, it is apparent that the range of isotope compositions substantially decreased from precipitation water to soil water to stream water and to groundwater. During the entirety of this study, the groundwater isotope composition remained near its average of -8.82‰ and -56.53‰ for $\delta^{18}O$ and δD, respectively.

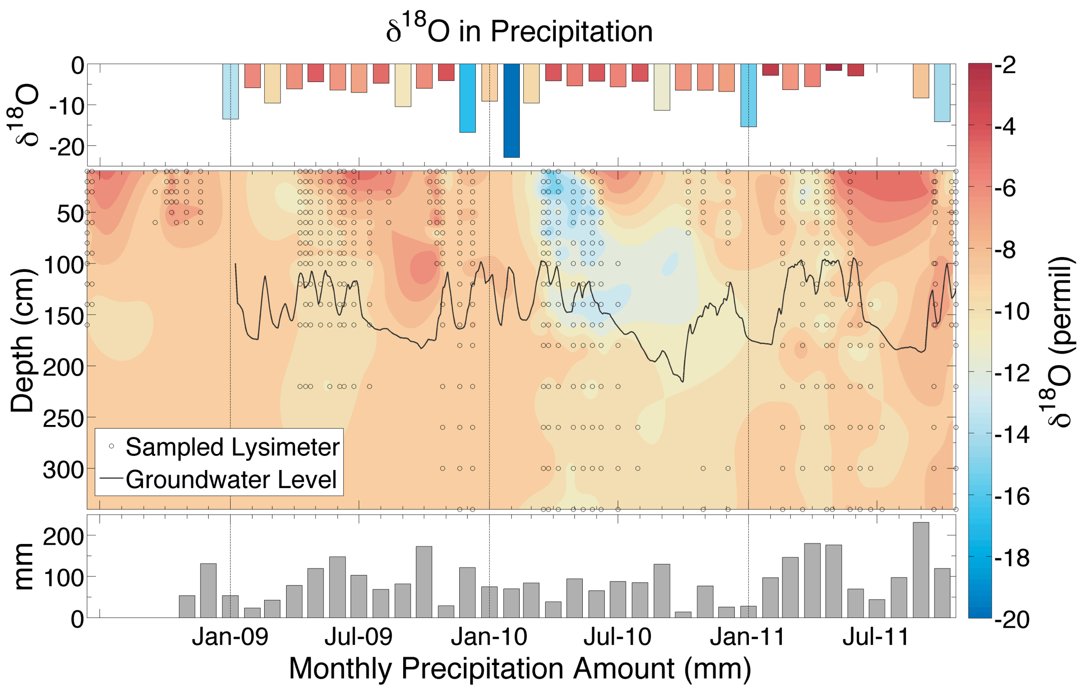

Figure 2-5: Monthly amount-weighted isotope composition in precipitation, the kriged map of soil water isotope composition through depth and time, and monthly precipitation amount. Red values correspond to less-depleted isotope composition while blue values correspond to more-depleted values. Black circles correspond to catchment-averaged lysimeters (see text). Ten-day moving averages of the groundwater level in the valley floor are plotted as a black line. Kriging uncertainty contours are plotted over the same space-time domain (see supplemental materials). Ordinary kriging and kriging variance were computed in Matlab.

Isotope compositions of soil water varied seasonally, closely reflecting the precipitation composition (Figure 2-4). Generally, more depleted compositions of soil water were found in the winter and spring and less depleted compositions were found in the summer and fall. However, for a given year, the soil water sampled during the spring (rather than winter) was generally the most depleted due to the snowmelt. Compositions evolved through the spring and summer months, with soil water isotope compositions becoming less depleted in the fall; however, the degree of such an enrichment trend varied from year to year (Figure 2-4).

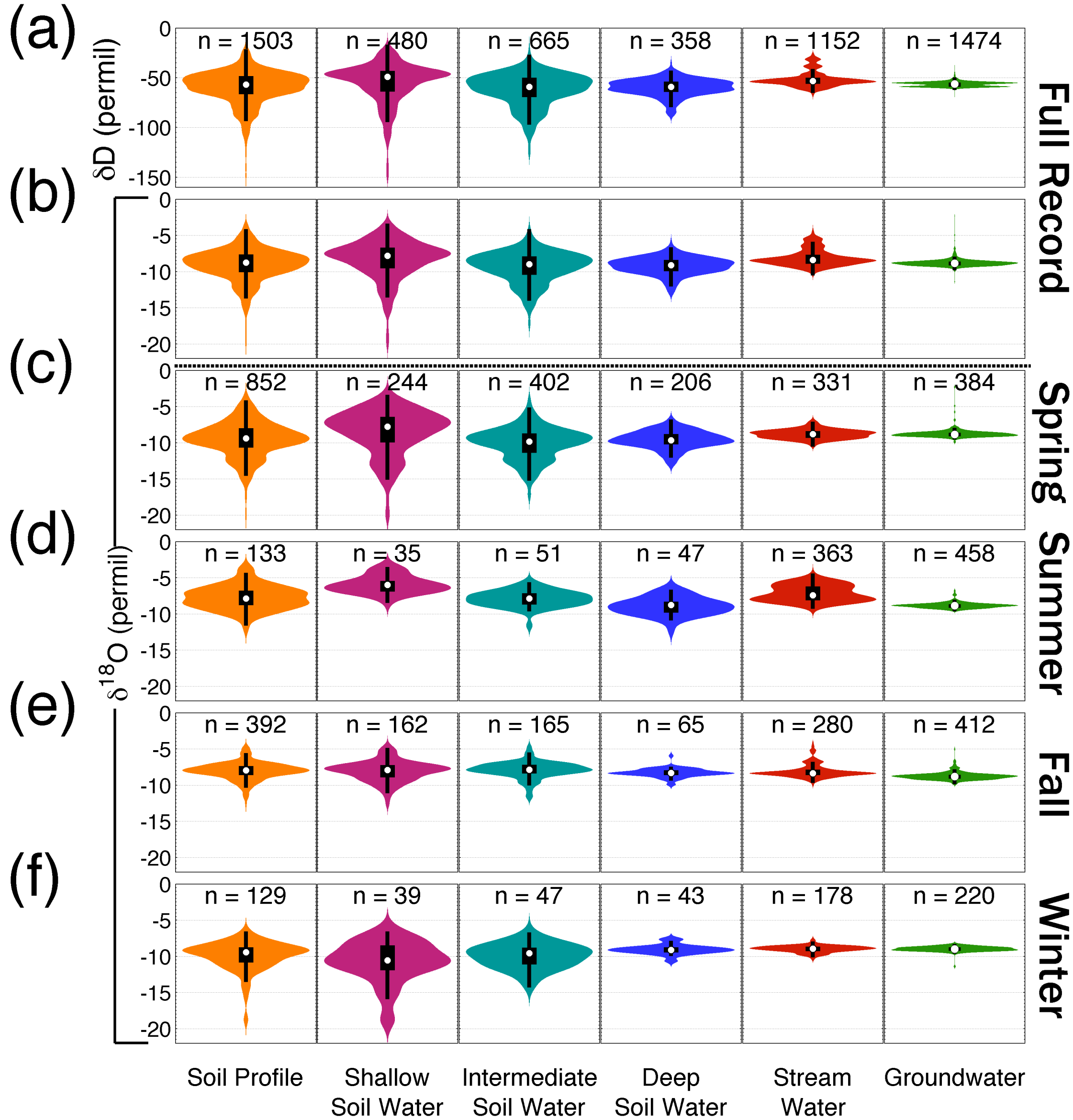

Figure 2-6: Violin plots of the distribution of deuterium (**a**) and oxygen-18 (**b**) composition for each hydrologic pool within the catchment sampled from Jun. 13, 2008 to Mar. 16, 2012, with sample number, n, indicated. The full record was split into four seasons, spring (**c**), summer (**d**), fall (**e**), and winter (**f**), based on astronomical calendar. The full soil profile violin plot (orange) is a composite of shallow soil water (purple, ≤30 cm), intermediate soil water (teal, 40-100 cm), and deep soil water (blue, ≥120 cm). The shape of the violin plot is the smoothed kernel density distribution, normalized so the area of each plot is equal to one. Inside each violin plot is a standard bar plot. The white point corresponds to the median of the data, inner black box is interquartile range, and whiskers cover 1.5 interquartile range. Outliers are left off for clarity, but can be seen in the tails of the kernel density distribution.

Seasonal variation of soil water isotope composition was also reflected in its vertical profile, with $\delta^{18}O$ and δD exhibiting strong damping with depth (Figure 2-7). When analyzed as catchment-wide averages, the shallow soil lysimeters (<30 cm depth) showed larger standard deviations and had a mean similar to the isotope composition of seasonal precipitation. This seasonal amplitude was attenuated with depth as soil water isotope compositions approached the groundwater average. Overall, the winter isotope composition profile was more depleted than the groundwater average while the summer isotope composition profile was less depleted. Furthermore, the winter profile had a larger standard deviation for shallower soil depths (<100 cm) when compared to the summer, suggesting a more hydrologically active soil profile where soil water was being replaced by new precipitation. The stable isotope composition profiles for the transitional seasons of fall and spring were intermediate between that of the wet and dry seasons with shallow soil water closely matching seasonally-weighted precipitation compositions (Figure 2-7). Both these profiles had relatively constant means and decreasing standard deviations with depth. The isotope profile during the spring season had relatively large standard deviation that was indicative of wetter soils and shorter residence times of water, whereas the fall season had less variation indicative of drier soils and longer residence times. These trends matched our field observations (Lin, 2006; Lin et al., 2006b). Both isotope profiles approached the groundwater average at deeper soil depths. Interestingly, only the spring profile was more depleted than the associated seasonal precipitation composition for the entire depth.

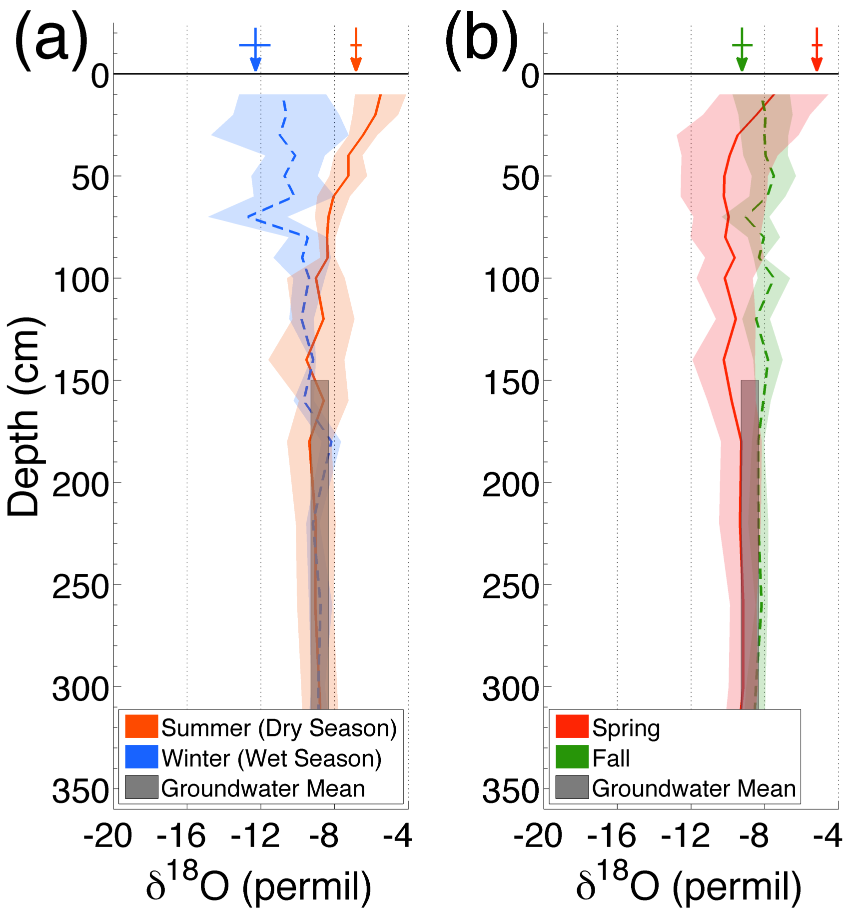

Figure 2-7: Seasonal $\delta^{18}O$ profiles of soil water for wet (winter) and dry (summer) seasons (a) and transitional seasons (spring and fall) (b) based on the three-year monitoring. Isotope composition at each depth was averaged over the entire catchment. One standard deviation is represented with shaded regions. Depths with only one sample were removed for clarity. For reference, groundwater mean and one standard deviation is shown as a grey bar, and the amount weighted precipitation compositions with weighted standard error for corresponding seasons are shown as colored arrows at the top.

Closer investigation using weekly and monthly time series revealed more details of the differences in soil water isotope composition evolution with depth. Water sampled from the lysimeters located in the shallow soil (≤30 cm) had the largest seasonality while water sampled from the deep lysimeters (≥120 cm) showed little seasonality (Figure 2-4). The deepest soil water isotope compositions were relatively constant through time and space and closely matched the groundwater isotope composition (Figure 2-5). This is likely due to the fact that these deep soil waters were collected in the midslope and valley floor where soil waters are known to have been derived from not only precipitation inputs but also groundwater inputs (Jin et al., 2011). Soil water sampled from the upper 30 cm had the largest $\delta^{18}O$ variations, while maximum and minimum isotope compositions deeper in the soil profiles typically occurred later in time indicating a phase lag. The time delay in the amplitude of the isotope soil profiles is especially evident in the upper soil layers and can be seen by comparing isotope composition of precipitation and soil water sampled at 10 cm (Figure 2-5).

Inter-annual variability is also apparent through closer investigation of higher temporal resolution time series. For instance, during the spring and summer of 2009 and 2011, the soil water isotope composition became less depleted than the groundwater average, with the shallow soil water showing the strongest trend (Figure 2-4 and Figure 2-5). Total enrichment of shallow soil water (≤30 cm) from April to October was approximately 3‰ for $\delta^{18}O$. Enrichment of intermediate and deep soils also occurred but was less prominent.

During the spring and summer of 2010, the soil water isotope composition showed a slightly different attenuation with depth as compared to that in 2009 or 2011 (Figure 2-4 and Figure 2-5). Over that period, soil water was more depleted than the groundwater average. This initially more depleted signature was likely due to the 33% larger amount of winter precipitation during 2010 and resulted in a much more depleted starting point once the snowpack melted and the soil thawed. This highlights that inter-annual variability in isotope composition cannot be neglected. Throughout the remainder of the spring and summer in 2010, the soil water displayed a similar enrichment trend as in 2009 and 2011 but with a larger magnitude of 5‰ for $\delta^{18}O$ in the shallow soil layer.

2.4.4. Spatial Variability of Soil Water Isotope Compositions

2.4.4.1. North and South Slopes

To determine spatial patterns in the soil water stable isotope composition, variations of soil isotope profiles on the north (south-facing) and south (north-facing) slopes were compared during the winter and summer (Figure 2-8). For both the north and south slopes, the winter profiles were depleted while the summer profiles were enriched (similar to precipitation) but with attenuation with depth showing an approach toward the groundwater average below ~100 cm. However, the amplitude of the winter (wet season) profiles differed between the two slopes, with a slightly more depleted signature observed on the north slope in the A-horizon (upper 20 cm) as compared to the south slope. Further, the difference between isotope compositions in the A-horizon of the winter and summer profiles was larger for the north slope as compared to the south slope. Also for both the north and south slopes, the winter profile had a larger standard deviation (amplitude) than the summer profile. The winter profile for both the north and south profiles showed considerable variability down to a depth of ~80 cm, while the summer profiles are relatively smooth. The winter-time variation is likely the result of episodic melting and the effect of preferential flow.

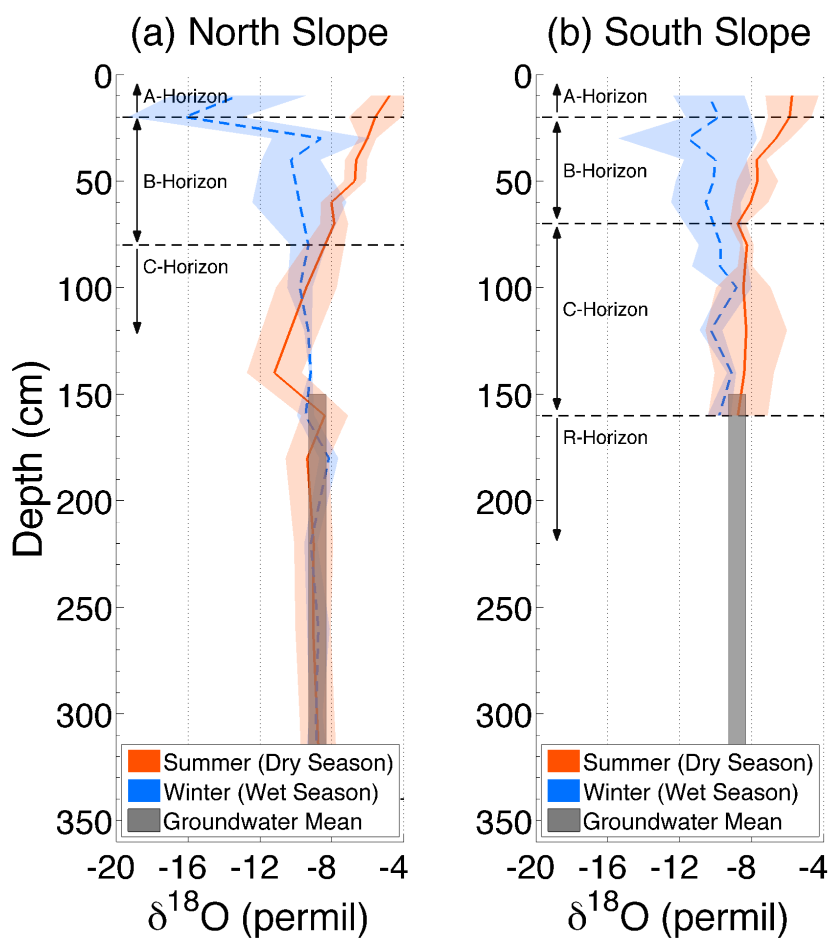

Figure 2-8: Seasonally-averaged $\delta^{18}O$ composition in soil profiles for the north (south-facing) (a) and south (north-facing) (b) slopes based on the three-year monitoring. One standard deviation is represented with shaded regions. Depths with only one sample were removed for clarity. Typical soil horizon interfaces are shown as black dashed lines. Groundwater mean and one standard deviation are shown as grey bar for reference.

2.4.4.2. Ridge Top, Midslope, and Valley Floor

Seasonal soil water isotopic composition profiles also differed with slope location regardless of the north or south slopes (ridge top, midslope, and valley floor). The amplitude of the winter profile for each slope location showed larger variability compared to the summer profiles (Figure 2-9). Profiles on the ridge top were limited by soil depth (<50 cm) and generally reflected winter and summer precipitation. The winter profile at midslope showed increases in amplitude variation at both 20 and 60 cm depths, where horizon interfaces are located (Table 2-1), layers identified by Jin et al., (2011) as high-flow zones. The winter profile in the valley floor showed the greatest variation in the amplitude in the upper part of the profile, which was likely due to the effect of large water table variations near the valley floor, plus episodic melting and the effect of preferential flow.

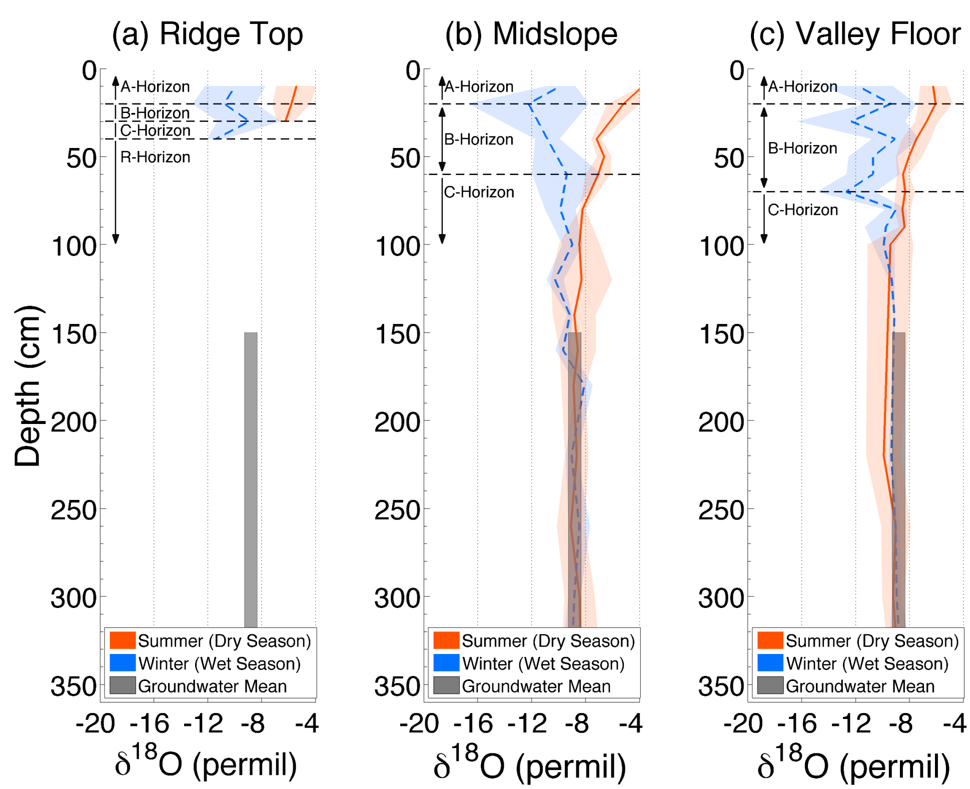

Figure 2-9: Seasonally-averaged $\delta^{18}O$ composition in soil profiles for each slope location based on the three-year monitoring: ridge top (a), midslope (b), and valley floor (c). One standard deviation is represented with shaded regions. Depths with only one sample were removed for clarity. Typical soil horizon interfaces are shown for each slope location. Groundwater mean and one standard deviation are shown as grey bar for reference.

2.4.4.3. Swale and Planar Hillslopes

For both the winter and summer profiles in the swale depressions, there were specific depths where the standard deviation of isotopic composition quickly increased (Figure 2-10). Specifically, in the winter, the standard deviations increased at 30 and 60 cm depths and corresponded to the soil-bedrock interface on the ridge top and the B-C horizon interface at the midslope and valley floor lysimeter nests (Table 2-1). Additionally, the swale summer profile showed increases at depths of 60 and 100 cm. The planar hillslope isotope profiles, on the other hand, were relatively more uniform, but with large variation in amplitude in the A, B, and C-horizons during the wet season. Below the C-horizon, both swale and planar profiles were relatively constant approaching the groundwater mean (Figure 2-10).

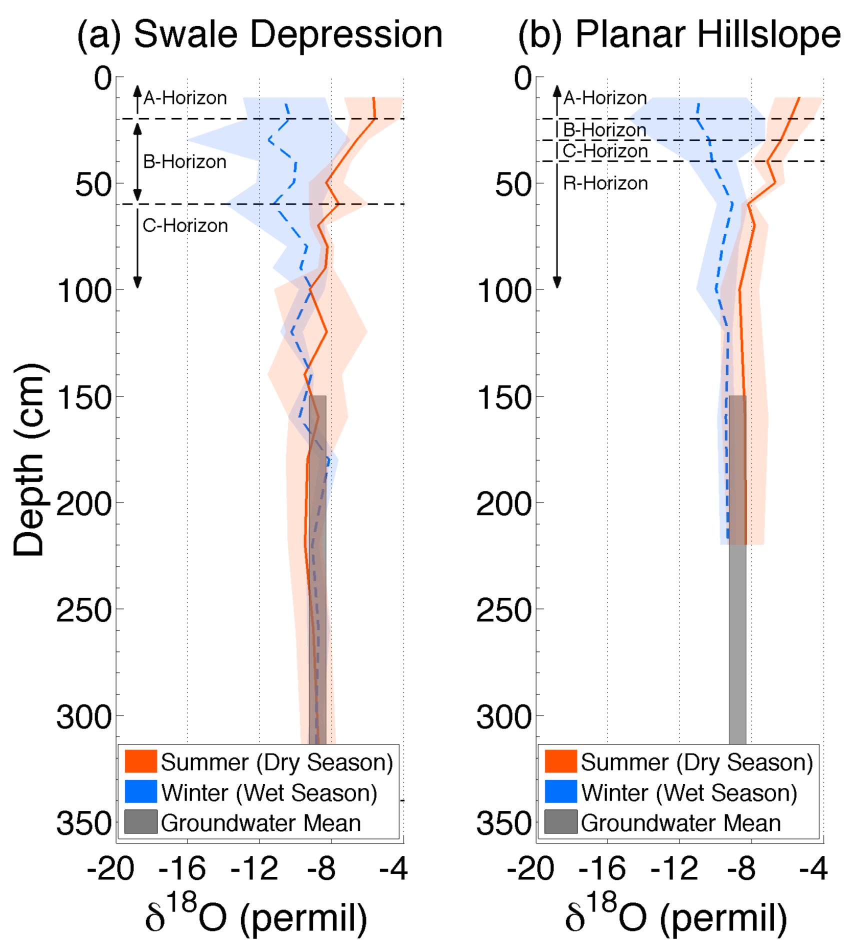

Figure 2-10: Seasonally-averaged $\delta^{18}O$ composition in soil profiles for hillslope type based on three-year monitoring: swale depression (a) and planar hillslope (b). One standard deviation is represented with shaded regions. Depths with only one sample were removed for clarity. Typical

soil horizon interfaces are shown for each hillslope type. Groundwater mean and one standard deviation are shown as grey bar for reference.

2.5. Discussion

2.5.1. Damping of Seasonality with Soil Depth, Advection, and Mixing

The seasonal damping with depth is characteristic of advective-dispersive transport and mixing (Leibundgut et al., 2009) and has been observed in previous studies (Eichinger et al., 1984; Darling and Bath, 1988; Geake and Foster, 1989; Clark and Fritz, 1997; Tang and Feng, 2001; Lee et al., 2007) including work at Shale Hills (Jin et al., 2011). However, the degree and cause of damping reported in these earlier studies differed. Leibundgut et al. (2009) pointed out that the depth of seasonal damping decreases as soils become finer grained. For example, in deep gravel profiles of western Germany, Eichinger et al. (1984) found the seasonal isotopic profile was heavily damped over the first 9 m; while in the English chalk, heavy isotopic damping was found in the first meter (Darling and Bath, 1988; Geake and Foster, 1989). At the SSHCZO, the silt loam or silty-clay loam provided strong attenuation of the seasonal isotopic profile typically within the upper 1.5 m. One explanation for the relatively rapid attenuation of the seasonal isotope profiles is hydrodynamic mixing during percolation through permeable soils, a phenomenon observed in the majority of profiles at the SSHCZO (Figure 2-7 through Figure 2-10).

2.5.2. Evidence for Preferential Flow

Previous work at the SSHCZO has identified the importance of both vertical and lateral preferential flow in the catchment (Lin, 2006; Lin and Zhou, 2008; Graham and Lin, 2011; Jin et al., 2011). Vertical preferential flow in the summer months has been identified as occurring through macropores resulting from multiple causes including hydrophobic organic surface layers and vertical high-permeability zones, while lateral preferential flow occurs along soil horizon and/or soil-bedrock interfaces (Lin and Zhou, 2008; Graham and Lin, 2011; Jin et al., 2011). Our findings in this study support these observations and provide further insight into specific locations.

Soil water isotopic profiles help to understand the timing and direction of water movement at the SSHCZO. For example, the averaged seasonal isotope profile (Figure 2-7) demonstrated the average isotope concentration with depth as well as the standard deviation. In the summer profile, it was clear that the standard deviation remained relatively low throughout the upper 90 cm. This low standard deviation is indicative of longer residence times and smaller change within the soil profile. This pattern changed slightly at a depth of 100 cm where the standard deviation expanded. To explain this increase in standard deviation, water with a different isotope composition must have replaced the water in deeper soils without displacing the water in the shallower soil layers. There were two possibilities for this phenomenon: 1) downward preferential flow through macropores located either in the valley itself or derived from interflow from upslope that itself derived from water inputs through macropores located upslope, or 2) upward groundwater movement through either capillary rise and/or a rising water table. Upward groundwater movement was unlikely since the isotope composition of groundwater remains nearly constant throughout the summer months and thus would not explain the increased standard deviation. This means that downward preferential flow, the flow that bypassed the shallow part of the soil matrix (either through macropores in the valley floor or upslope) was likely the cause of this increased standard deviation. Evidence suggested vertical preferential flow, which bypassed the shallow soils, occurred for each landform type and hillslope location but only appeared in the isotopic measurements during the summer months (Figure 2-8, Figure 2-9, and Figure 2-10).

Soil water isotopic composition profiles also provided the evidence of lateral preferential flow within the SSHCZO. For example, the winter isotope profile for soil water on the midslope showed increases in standard deviation at depths of 20 and 60 cm depths associated with the A-B and B-C horizon interfaces (Table 2-1 and Figure 2-9). This pattern of increased standard deviation at depths related to soil horizon or soil-bedrock interfaces occurred in other soil profiles during the wet season (including the valley floor, swale, and planar hillslopes), suggesting that lateral preferential flow was widespread within this catchment. Note that evidence for such lateral preferential flow was not observed during the summer months when soils were dry (Figure 2-8, Figure 2-9, and Figure 2-10). This general model for fast water flow through vertical macropores and horizontal soil interfaces was also invoked by Jin et al. (2011) to explain the water isotopic data and water chemistry data specifically for the south planar hillslope.

2.5.3. Snow Melt Dynamics

Soil water isotope composition profiles also provided insight into snowmelt dynamics, which play an important role in solute transport and chemical weathering differences between the slopes at the SSHCZO. This was best observed when comparing the profiles from the north (south-facing) and south (north-facing) slopes (Figure 2-8). It was clear that the north slope had a more depleted composition in the A-horizon during the winter months when compared to the south slope. This more depleted signature was due to varying snowmelt dynamics. Due to the small size of the catchment, the amount and isotope composition of snowfall is assumed to be the same for both the slopes. The east-west orientation of the catchment, however, produces an asymmetry in solar radiation between the north (south-facing) slope and south (north-facing) slope. The higher solar radiation on the north slope supports a relatively thin snowpack (typically <30 cm) with likely melting and infiltration to the surface soils. The infiltration of isotopically-depleted snowmelt alters the composition of the upper 20 cm of the soil resulting in a soil water isotope composition of -16‰ for $\delta^{18}O$ on the north slope. Conversely, on the south slope, the snowpack remained intact for longer periods in the winter months. While the south-side snowpack remained frozen, the air temperature increased and the relative humidity remained low allowing the snowpack to sublimate and enrich the isotope composition of the residual snowpack. Over the winter season this resulted in a less depleted isotope composition in the snow on the south slope, and later melting and infiltration than the north slope.

The temporal evolution of soil water isotopes with depth provided other insights into the importance of snow in soil water dynamics at the SSHCZO. For example, after the winter of 2010, the spring and summer isotope profiles showed dramatically more depletion throughout the entire profiles (Figure 2-5). After the first sampling in the spring, relatively depleted isotope compositions appeared in depths from 10 to >150 cm. This depleted signature was due to light wintertime precipitation, melting and infiltration, which subsequently mixed intermittently with deeper soil (150-175 cm) and groundwater. This depleted isotope signature remained in soil water through mid-May 2010, when spring/summer precipitation gradually replaced the shallow soil water while deeper soils (>25 cm) continued to hold water with the depleted signature until fall. During this period, most soil profiles showed high moisture content during the spring snowmelt and this moisture was retained through early summer. As the growing season progressed transpiration gradually removed the matrix water, which then began to absorb spring/summertime precipitation. Still, the soil water at the intermediate depths retained the winter precipitation signature through the entire growing season, showing somewhat depleted signatures at 70 cm depth in October 2010 (Figure 2-5).

2.5.4. Evaporation Dynamics

Seasonal enrichments of soil water isotope compositions were found to occur each growing season (spring-summer) (Figure 2-4 and Figure 2-5). There are two factors contributing to this enrichment trend: 1) evaporation of water from the soil matrix or 2) input of less depleted summer precipitation. To determine the degree of growing season evaporation, soil water samples were plotted against the LMWL (Figure 2-11). Variations along the LMWL correspond to the seasonal precipitation compositions while deviations to the right of the line are indicative of evaporative effects due to differences in fractionation rates of oxygen-18 and deuterium (Barnes and Allison, 1988), allowing for distinction of enrichment trends. During the summer months all the soil water samples fell on or above the LMWL, with samples from shallow soils (≤30 cm) near the spring and summer precipitation compositions and samples from intermediate soils (40-100 cm) near the groundwater average (Figure 2-11) indicating mobile soil water showed little to no evaporative signal, but rather was highly dependent on the precipitation isotope composition. Additionally, investigation of deep soil waters (≥ 120 cm) showed no evidence of evaporation (data not shown). Because of the limited role of evaporation, transpiration is believed to be the main contributor of the evapotranspiration flux in this dense, forested catchment. However, we feel that the lysimeters may not be adequately sampling tightly bound water and a study is underway to assess this effect.

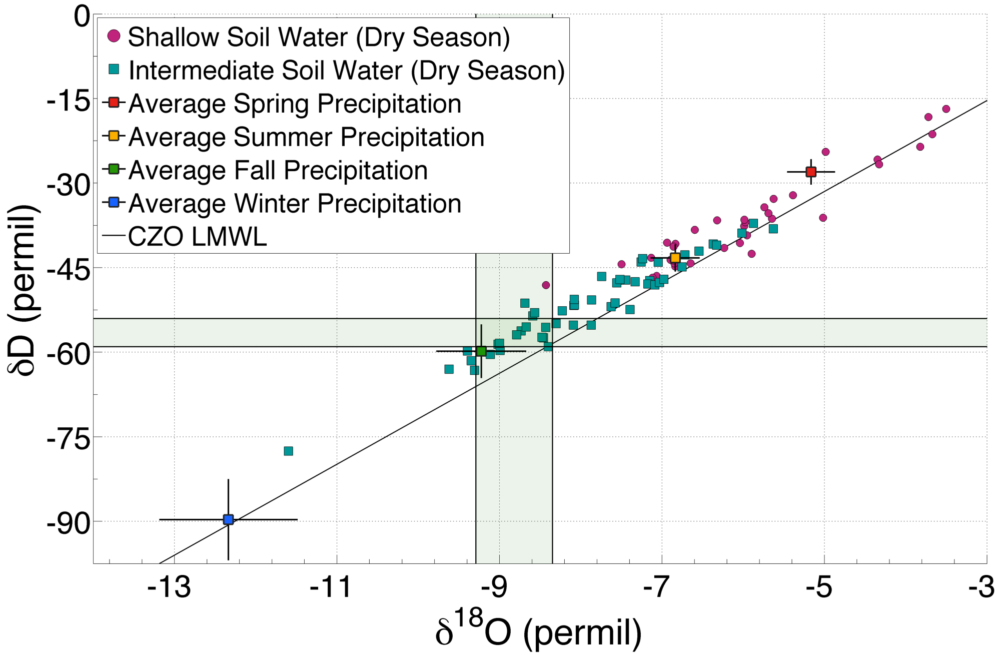

Figure 2-11: Shallow (≤30 cm depth) and intermediate (40-100 cm depth) soil water sampled during the summer (dry) season with SSHCZO Local Meteoric Water Line. Amount weighted precipitation compositions with weighted standard error bars for each of the four seasons are shown for reference. Green region indicates groundwater average (± one standard deviation) for each isotope composition.

2.6. Summary Conclusion

The stable isotope network developed at the SSHCZO has provided extensive monitoring of the evolution and patterns of water stable isotopes for over three years beginning in 2008. Through high frequency sampling of precipitation and groundwater, the isotope compositions of the soil profile's end members were established. Comprehensive investigations of soil water isotope spatiotemporal patterns have provided the following conclusions:

1. Shallow soil water was highly influenced by seasonal precipitation input composition. Monitored soil water clearly displayed the seasonal isotopic signal of precipitation, with more depleted values typically occurring in the winter months and less depleted values occurring in the summer months.
2. The seasonal amplitude of soil water isotope composition was heavily damped within depths of 1-2 m, approaching a nearly constant value similar to the groundwater

composition (Figure 2-7). This successive damping suggests the importance of hydrodynamic mixing, which integrates multiple seasons of precipitation.

3. Large variations in the winter soil water isotope profiles were observed at most sites and we interpreted this variation as evidence for preferential flow (Figure 2-8, Figure 2-9, and Figure 2-10). Increased variations were likely due to intermittent snowmelt, the effects of soil structure and horizons, and low residence times. Relatively smooth isotope profiles were observed in the summer season indicating preferential flow is less frequent or observable during the summer.
4. Asymmetry in the radiation balance between north (south-facing) and south (north-facing) slopes seems to explain early snowmelt and infiltration on the north slope, while the snowpack on the south slope sublimated and became enriched before infiltrating (Figure 2-8).
5. In the winter of 2009-10, heavy snowfall with depleted isotope compositions influenced the soil water isotope composition for the entire growing season. The depleted signatures remained in the deep vadose zone through the end of the growing season (Figure 2-5).
6. Summer soil water profiles aggregated across the catchment showed little evaporative effect (Figure 2-7 and Figure 2-11). The soil water isotope composition at SSHCZO is dominated by the precipitation input, with minor evaporative enrichment, and is consistent with transpiration dominating evapotranspiration in this dense, temperate forest environment.

One limitation of this study is soil water sampled from suction-cup lysimeters may not reflect tightly-held water within the soil matrix (Darling and Bath, 1988; Landon et al., 1999; Figueroa-Johnson et al., 2007; Brooks et al., 2009). Currently, new experiments are underway to resolve the mobile and less-mobile soil water fractions. For example, studies are underway by the SSHCZO ecology team to investigate tree species water usage for addressing interception, transpired water and root uptake. By monitoring tree xylem and root $\delta^{18}O$ composition, we will be able to determine effective depth of root water extraction. Lastly, recent work has identified the importance of fractured bedrock and deep groundwater as important water sources to headwater streams (Burton et al., 2002). Drilling to explore deep groundwater at the SSHCZO is ongoing.

2.7. Acknowledgements

We thank those who installed the soil lysimeters, B. Ketchum and L. Jin and others. We also thank those who helped with fieldwork, including B. Ketchum, R. Ravella, J. Williams, E. Herndon, M. Holleran, Z. Ruge, T. Yesavge, L. Liermann, K. Bazilevskaya, C. Duffy, R. Jones, and L. Eccles. Financial support was provided by the National Science Foundation under Grant No. EAR- 0725019, 2008-2013 for Susquehanna-Shale Hills Critical Zone Observatory to CJD.

Chapter 3.

Interpreting High-Resolution Sampling of Precipitation Isotope Compositions for Hydrologic Applications

This chapter will be submitted for publication with co-authors C. J. Duffy and E. W. Boyer.

3.1. Abstract

Complex, catchment-scale isotope ecohydrologic studies are becoming more prevalent as field and laboratory instrumentation becomes more accessible. Associated with these studies is the high frequency sampling and isotopic analysis of precipitation, which is often performed to ascertain processes that may occur over short time intervals. Often long term hydrologic studies are being performed concurrently to monitor interactions between hydrologic pools. This investigation examined the effect of high frequency (6 hourly) weighted time averaging of isotopic composition of precipitation at the Susquehanna-Shale Hills Critical Zone Observatory (SSHCZO). Unweighted and amount weighted kernel density estimates of 6 hourly samples showed precipitation compositions are biased towards more depleted values. Time averaging decreased variation as samples were integrated to daily, weekly, monthly, or seasonally amount weighted values. Each time series provided a different local meteoric water line, which could influence hydrologic interpretations. The role of high frequency sampling of precipitation clearly shows that the estimation of the local meteoric water lines is influenced by low d-excess and low amount events, which contribute very little to the watershed's hydrology. The study suggests that the most useful LMWL will depend on the nature of the study and the time scales and processes one is interested to study.

3.2. Introduction

Stable isotopes of water ($\delta^{18}O$ and δD) have been used extensively in environmental investigations to trace pathways which otherwise could not be observed. Because they move with the water molecule itself, liquid water stable isotopes are an ideal tracer for many experimental studies. Over the past few decades, substantial progress has been made using water stable isotopes to inform researchers about various environmental processes including groundwater recharge rates (Gat, 1971; Darling and Bath, 1988; Criss and Davisson, 1996; Winograd et al., 1998), storm flow generation and hydrograph separation (Sklash et al., 1976; Sklash and Farvolden, 1979; Rice and Hornberger, 1998), and determination of preferential flowpaths (McDonnell, 1990; Leaney et al., 1993; Kirchner, 2003; Vogel et al., 2010). Recent work has advanced the understanding of ecohydrologic processes such as tree water use (Dawson and Ehleringer, 1991; Ehleringer and Dawson, 1992; Brooks et al., 2009; Gierke, 2012) and vadose zone hydrology (Zimmermann et al., 1968; Barnes and Allison, 1988; Phillips, 1995; Gazis and Feng, 2004). Common to each of these studies is the analysis and interpretation of precipitation isotope compositions as the hydrologic input to the system.

The physical processes governing isotopic compositions of precipitation have been well detailed over time. Dansgaard (1964) outlined the kinetic and equilibrium fractionation factors which influence isotopic composition evolution as well as established a linear relationship between annual isotopic composition and surface air temperatures for the globe. Over time, four main factors have been found to contribute to the isotopic composition of precipitation: continental effects where compositions become more depleted as an air mass moves from its source across a continent, latitude effects where compositions become more depleted towards the polar regions, altitude effects where compositions become more depleted with altitude due to rain out processes, and amount effects where compositions become more depleted with increasing precipitation amounts. Each of these can be thought of as relating to the amount of “rain-out” an air parcel has experienced as it moves from its moisture source to the precipitation site.

Craig (1961) was the first to identify a linear relationship between $\delta^{18}O$ and δD compositions by analysis of 400 samples across the globe. The result was the global meteoric water line (GMWL):

$$\delta D = 8\ \delta^{18}O + 10\ ‰ \qquad (1)$$

Over the past few decades, with an improved understanding of stable isotope geochemistry and larger datasets, more precise values for the slope and intercept of the GMWL were developed (Rozanski et al., 1993):

$$\delta D = 8.17\ (\pm 0.07)\ \delta^{18}O + 11.27\ (\pm 0.65)\ ‰ \qquad (2)$$

The GMWL is a composite of many local precipitation isotope compositions and corresponding local meteoric water lines (LMWL) reflecting local or regional meteorological processes.

Few studies detail the methods of constructing LMWLs. Typically, LMWLs are constructed using standard least squares regressions which assumes the observed x variable ($\delta^{18}O$) is known exactly, which may be a poor assumption in many situations, especially in the case experimental studies where both isotopes are measured with varying degrees of precision. The reduced major axis method, which has been employed by the IAEA (1992), is an improvement over the standard least squares regression by allowing a standard deviation to be associated with the x and y variables. An additional improvement was implemented by Argiriou and Lykoudis (2006) with the use of error-in-variables generalized least squares regression. An additional complication is the decision to either use the highest resolution samples or averaged isotopic compositions in the chosen regression procedure. Simple regression procedures are typically used to produce LMWLs, but Hughes and Crawford (2012) showed that the incorporation of precipitation amounts to the least squares regression can statistically change the regressions. As such, researchers are left with ad-hoc strategies to construct the LMWL for describing precipitation isotope composition patterns for the given location and particular application.

The objectives of this study are to develop a general understanding of high frequency isotopic composition of precipitation at the SSHCZO for the period 2009 – 2012. The goal of the experiment is to support ongoing isotope hydrology studies in an upland watershed. We are interested in understanding the underlying probabilistic characteristics of isotopic species in precipitation and how they may evolve through time. Additionally we hope to establish a robustly defined local meteoric water line sufficient to support hydrologic interactions with other $\delta^{18}O$ and δD pools at the SSHCZO (http://criticalzone.org/shale-hills). Finally, over the longer term, this study will improve the prospects of developing and/or analyzing space and time distributions for isotopes in precipitation, which could be implemented into distributed numerical models for isotope transport and age modeling.

3.3. Materials & Methods

3.3.1. SSHCZO Description & Climate

The SSHCZO is a 7.9-ha forested catchment located in central Pennsylvania and is characteristic of the Ridge and Valley Physiographic Province of eastern United States (Figure 3-1). It is located (40°40' N, 77°54' W) approximately 320 km west of New York City and 250 km southeast of Lake Erie and varies in elevation from 311 m at the ridge top to 258 m at the stream outlet. The V-shaped, headwater catchment is oriented east-west and contains an intermittent 1st order stream that typically flows from late September to early June. The SSHCZO lies within the

Shavers Creek watershed of the Juniata River, which in turn is a sub-basin of the Susquehanna River.

The climate for SSHCZO is humid where the long-term average annual precipitation is 1,006 mm and is approximately evenly distributed throughout the year (Figure 3-2). Winter precipitation consists of a mixture of rain and snow, with the catchment receiving approximately 116 mm of snow annually. Mean annual temperature is 10.1˚C and spends, on average, 32.4 days below 0˚C and 61.2 days above 26.6˚C based on a 30-year record (NOAA, 2007). Summers are typically hot and humid with high temperatures reaching >30˚C and precipitation events consisting of short, high-intensity storms. Winters are typically wet and cold with temperatures less than -10˚C and precipitation events consisting of both rain and snow.

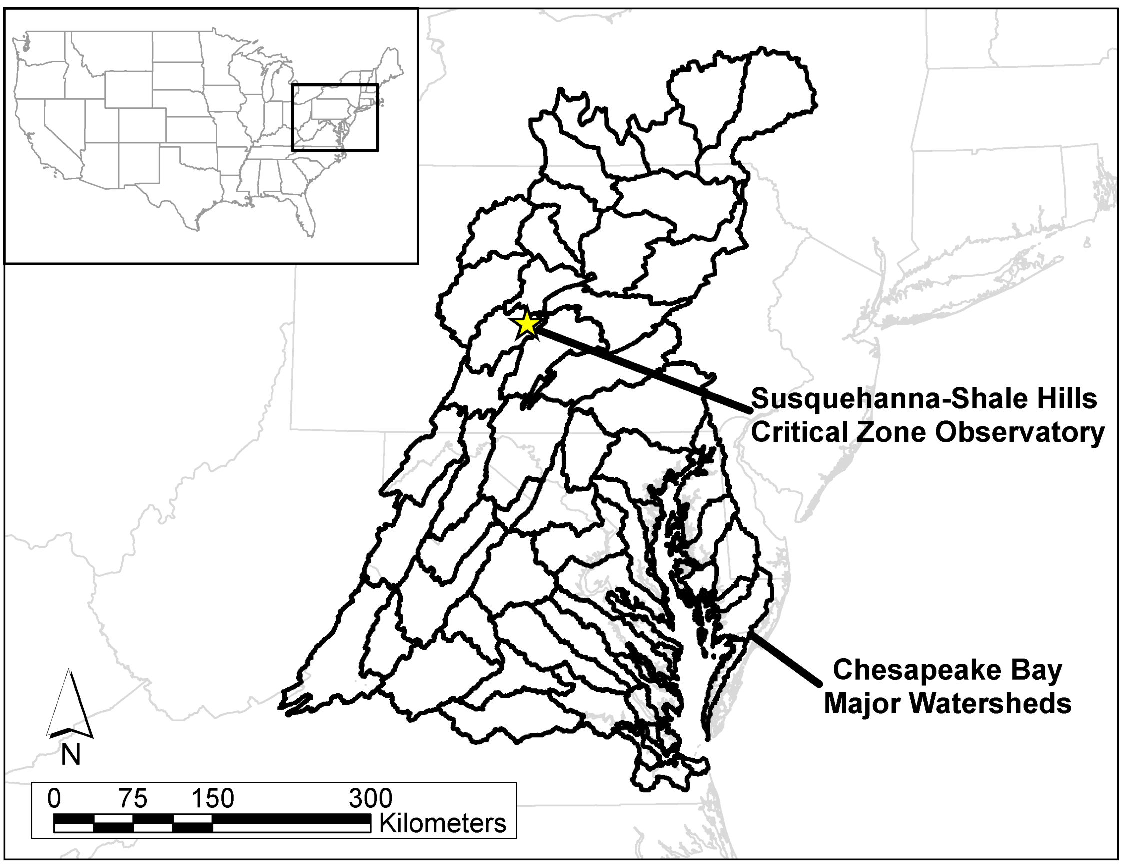

Figure 3-1: Location of Susquehanna-Shale Hills Critical Zone Observatory (yellow start) with respect to the Chesapeake Bay major watersheds (black lines).

3.3.2. Monitoring Procedures & Isotopic Analysis

Meteorological data were collected in a small clearing area along the ridge of the SSHCZO catchment from 2009-2012. Precipitation was monitored using an Ott-Pluvio weighing bucket (Hach Company, Loveland, CO) in ten-minute intervals with a precision of 0.1 mm and a Laser Precipitation Monitor (LPM, Thies Clima, Göttingen, Germany) in ten-minute intervals with precision of 0.01 mm. The LPM is capable of distinguishing 21 separate types of precipitation (e.g., drizzle, rain, snow, or hail) based on the size and velocity of the precipitation. Data were collected and transmitted on-line in real time and processed annually for missing data. Appendix A outlines the relationship between the Ott and LPM. Results from their comparison provided a range of regressions depending on integration period (10-minute, 1-hour, 6-hour, daily). Additionally the Ott was shown to be less variable over longer periods of the record. Therefore the Ott precipitation record was used when possible to determine precipitation amounts for the catchment. Missing data in the Ott record were filled directly using the ten-minute regression of the LPM and regional observations provided by the Pennsylvania State Climatologist (http://climate.met.psu.edu/).

Precipitation samples, for isotopic analysis, were collected Jan. 14, 2009 to Dec. 20, 2012 on an event basis using an automatic precipitation sampler (model: NSA 181/S, Eigenbrodt GmbH & Co., Königsmoor, Germany) located in the clearing area on the ridge top approximately 6 m from the Ott-Pluvio weighing bucket. To capture intra-storm variability, precipitation was collected for the first 30-minutes of a storm followed by three 6-hour intervals. At the onset of an event, a gold-plated sensor would detect moisture causing the instrument's funnel cap to open and begin collecting precipitation while, at the same time, initiating an internal timer. For the first 30-minues the instrument would funnel precipitation to the first bottle in series. The funnel cap would remain open, provided that the gold-plated sensor remained wet. After the first 30-minutes, the instrument would begin to funnel any precipitation to the second bottle in series for an additional 6-hours, after which bottles three and four would fill for six additional hours each. If at any point during the collection period the gold-plated sensor became dry, the instrument's funnel cap would close, preventing evaporation of the precipitation sample. The instrument was capable of collecting two separate events before resetting. Each one-liter bottle in the instrument was cleaned and dried prior to installation. In the event of extremely intense events, the instrument provided overflow routing to a reserve bottle preventing cross contamination. Samples collected in the reserve bottle were brought to the lab and archived but not included in this analysis. Additionally, heating coils located on the gold-plated sensor and within the funnel allowed for continual measurements of frozen precipitation. All precipitation samples were collected 1-3 days after an event and stored in 30 mL amber glass vials with cone-lined caps to prevent evaporation. Sample bottles were stored in a cool location and contained little or no headspace, when collection amounts permitted, to minimize water-air exchange.

Average precipitation type (rain, snow, drizzle, etc.) was estimated for each precipitation sample collected from the raw LPM record. The 21 types were narrowed and grouped into heavy rain, light rain, heavy snow, light snow, drizzle, and hail. For this study, the types were further narrowed for simplicity into rain or snow. The average type was estimated by determining the most predominate type of precipitation during a given collection period. During periods with numerous types of precipitation, the type that contributed the majority of precipitation amount to the sample was chosen. This procedure was labor intensive and resulted in a subjective identification of precipitation over each collection interval. In the event of gaps within the LPM record, sample precipitation type was flagged as missing data.

Water samples were analyzed using laser absorption spectrometer (DT-100 Liquid Water Isotope Analyzer, Los Gatos Research, Inc., Mountain View, CA) following the IAEA Standard Operating Procedure (Newman et al., 2008). The analytical precision of the instrument is 0.1‰ and 0.8‰ for oxygen-18 and deuterium, respectively (Lis et al., 2008). The isotopic composition of the water was reported as a δ-value relative to Vienna Standard Mean Ocean Water (VSMOW):

$$\delta_X(permil) = \left(\frac{R_X}{R_{VSMOW}} - 1\right) \times 1000 \quad (1)$$

where R is the ratio of deuterium to hydrogen or ^{18}O to ^{16}O in the unknown (X) or VSMOW.

3.3.3. Analysis Methods

3.3.3.1. Kernel Density Estimates

The frequency of observing a precipitation isotope composition at a given location can be difficult to infer from a simple time series, but fortunately there exist numerous statistical tools to assist in determining distributions from observations. Univariate and bivariate kernel density estimators were constructed to determine the underlying distribution of precipitation isotope compositions at SSHCZO. Kernel density estimation (KDE) is a nonparametric statistical tool used to estimate the probability density of a continuous random variable and has advantages over standard histograms. For example, KDEs are smooth, data dependent estimates of probability distributions while histograms require bin width and bin location parameters, making discontinuous estimates of the probability density. To demonstrate the advantages of KDEs over histograms, probability density histograms were constructed for the full dataset for $\delta^{18}O$ values only. Bin widths were determined using the Freedman–Diaconis rule, where the bin width is twice the interquartile range divided by the cubed root of the sample size (Freedman and Diaconis, 1981). To aid visualization of bivariate KDEs, contours were selected to correspond to cumulative probability densities of 95, 90, 75, 50, 25, 10, and 5%. Contours can be thought of representing a certain quantile of observations (i.e. 95% of the observations fall inside the 95% contour).

There are two parameters for KDE construction, kernel type and bandwidth. For both the univariate and bivariate case, Gaussian kernels were used for their straightforward nature. Alternate kernels were investigated briefly and results showed similar KDEs. Bandwidth selection, on the other hand, is important to KDE construction as it balances smoothness and resolution of the probability density distribution. A bandwidth that is too small results in a jagged distribution difficult to interpret, while a bandwidth that is too large results in an overly smooth distribution disguising asymmetries.

To more closely investigate the influence of bandwidth selection on the univariate and bivariate KDEs, a subset of the full precipitation record was selected. Selection of the subset was performed manually extracting a much smaller (6 samples) dataset that contained relatively large variations in isotopic composition and precipitation amount (Table 3-1). The six observations were collected within a 24-hour period during September 2011 and had an arithmetic mean of -9.11‰, a weighted mean of -8.87‰, and a range of 4.76‰ for $\delta^{18}O$ and an arithmetic mean of -60.84‰, a weighted mean of -57.99‰, and a range of 41.40‰ for δD. Reduction of the precipitation record from 456 to six reduced the complexity of the record and allowed simplified visual investigation of the KDEs.

Two bandwidths selection methods were compared for a univariate KDE of the subset; one set equal to unity and the other determined using the Silverman method (Silverman, 1986). The Silverman method provided relatively robust and straightforward estimates of bandwidth for the univariate distribution of the subset and was then used in the bivariate distribution of the subset. Because of its overall robustness and its accessibility, the Silverman method was then used in determining the bandwidth of the univariate and bivariate KDEs for the full precipitation record.

Further, KDEs were constructed from the subset using isotopic compositions only (unweighted KDEs) and using isotopic compositions weighted by precipitation amounts (weighted KDEs) for both univariate and bivariate distributions to understand the importance of precipitation amounts on the distributions. Weighted KDEs scale individual kernels by fractional amounts to estimate the probability distribution. Observations associated with very small amounts (<1 mm/6 hours) contributed very little to a given KDE.

Table 3-1: Subset of complete precipitation dataset for analysis of effects of bandwidth selection and precipitation amount weighting on one-dimensional and two-dimensional kernel density estimations (**Figure 3-3** and **Figure 3-4**).

Date of Event	Time of Event	Duration of Collection (HH:MM)	δD (permil)	$\delta^{18}O$ (permil)	Amount During Collection (mm)
9/6/11	8:45:00 AM	0:30	-75.73	-10.60	0.2
9/6/11	9:15:00 AM	6:00	-74.26	-10.52	8.3
9/6/11	3:15:00 PM	6:00	-78.73	-11.16	14
9/6/11	9:15:00 PM	6:00	-57.89	-8.86	28.2
9/7/11	3:50:00 AM	0:30	-37.33	-6.40	1.4
9/7/11	4:20:00 AM	6:00	-41.06	-7.06	23.5

3.3.3.2. Integration Periods

Individual precipitation samples were time-averaged to daily, weekly, monthly, and seasonally amount weighted compositions for both $\delta^{18}O$ and δD to determine the effects of time integration on the time series and the LMWL. Yearly amount weighted values for each of the four years were also calculated to understand interannual variability. Integration periods were selected for convenience and for comparison of typical sampling procedures of other isotope hydrology studies. Many hydrologic studies analyze bulk daily, weekly or monthly precipitation samples for isotopic composition and do not collect precipitation in sub-daily intervals. Bulk precipitation collection or low-resolution sampling effectively performs precipitation amount weighting in the field as larger events contribute more volume to a given sample. To integrate high-resolution samples from SSHCZO to longer intervals, the sample precipitation isotope compositions were weighted by precipitation amount and calculated using the following equation:

$$\delta_T = \frac{\sum_{i=1}^{n} P_i \delta_i}{\sum_{i=1}^{n} P_i} \tag{3}$$

where δ_T is the amount-weighted precipitation value, P_i represents the amount (depth) of precipitation in an event, δ_i is the isotope composition of an event, and n is the number of events in the time period considered.

3.3.3.3. Regression Procedures

The $\delta^{18}O$ and δD values from the various time series (sample, day, week, month, season) were used to construct the local meteoric water line for SSHCZO. Regressions were performed using ordinary least squares regression procedure (IAEA, 1992) on each time series as well as using a precipitation amount weighted least squares regression (Hughes and Crawford, 2012), yielding a total of six time-averaged estimates of the LMWL. Details on regressions procedures are provided in Appendix C. Correlation coefficients for ordinary least squares and precipitation weighted least squares regressions were calculated for each LMWL. T-tests for differences in slope between the precipitation amount weighted least squares regression and each ordinary least squares regression were performed following Volk (1958, p. 241).

3.4. Results & Discussion

3.4.1. Observed Meteorology

Although monthly precipitation amount normals, based on NOAA 30-year climate data (NOAA, 2007), are evenly distributed throughout the year, for the four-year observed record, precipitation amounts varied from month to month within a given year imposing interannual variability into the precipitation record. Typical of most locations, the SSHCZO seasonal compositions of $\delta^{18}O$ and δD in precipitation are largest in the late spring and early fall with low values in the winter. The driest year was 2009, with the first four months having considerably less precipitation than average and seven out of twelve months having less than average. The wettest year was 2011, with well above average precipitation occurring during March, April, and May. Interestingly, during the four observed years, precipitation amounts were near equal or less than average for February each year and above average for the month of May. The annual precipitation totals were 1,033 mm, 895 mm, 1,326 mm, and 930 mm for 2009 – 2012 respectively, values which were similar to the climate normal of 1006 mm.

The monthly temperatures of each year matched relatively closely with the climate normal. Temperatures tended to be coldest during the months of January, February, and December and warmest during June, July and August. The coldest year observed was 2009, with temperatures in January, May, June, July and December being clearly less than the long-term average. The warmest year was 2012, with temperatures well above average during January, February, March, May and December.

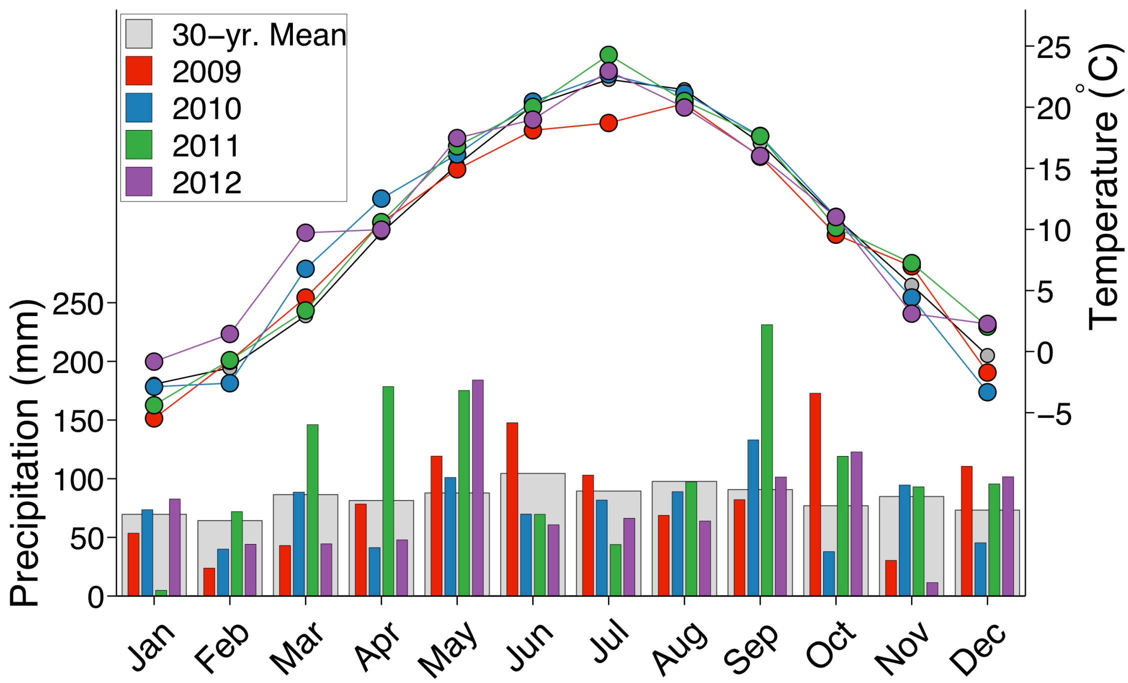

Figure 3-2: Monthly climate normals for precipitation (grey bars) and temperature (grey circles) based on NOAA 30-year record and monthly precipitation and temperature observations at SSHCZO for 2009 – 2012.

Six major meteorological events were identified using NOAA's Feature Directory for State College, PA (http://www.erh.noaa.gov/ctp/features/). The events were categorized as either a significant snow event or tropical storm. The three snow events identified include the October 15 – 16, 2009 storm which was the earliest measured snow fall event, dropping 15 cm across much of the state, the combination of storms on February 6 and 10, 2010 which dropped more than 60 cm of snow throughout Pennsylvania, and the Oct. 29 – 30, 2011 storm (i.e. "Snowtober") which dropped more than 20 cm of snow and caused widespread power outages. The other three major meteorological events were categorized as tropical storms or remnants of tropical storms. These events include the remnants of Tropical Storm Nicole September 30 – October 1, 2010 which dropped 10 cm throughout the state, Tropical Strom Lee August 4 – 8, 2011 which dropped more than 35 cm of precipitation in eastern Pennsylvania, and Hurricane Sandy October 28 – 30, 2012 which dropped over 7 cm of precipitation across much of the state and caused widespread damage along the Atlantic coast.

3.4.2. Kernel Density Estimations

3.4.2.1. Sample Test Case

To visualize the construction of the unweighted one-dimensional KDE (Figure 3-3a), individual Gaussian kernels (blue curves), with standard deviation of one, were centered at each of the subset's six observed isotopic compositions. Individual kernels were scaled by ⅙, to equally weight each kernel. The summation of the individual kernels yielded a smooth kernel density estimation for the data (red curve) with a bandwidth of one. It is clear that the KDE with a bandwidth of one was fairly smooth and showed two distinct peaks at -11.00‰ and -6.8‰. Conversely, using the Silverman method to calculate a bandwidth of 1.26, the KDE (black curve) became smoother and loss the two distinct peaks. Clearly, bandwidth selection plays an important role in establishing the shape of the distribution, as a balance must be made between smoothing and resolution.

To understand the impact of precipitation amounts to one-dimensional weighted KDEs (Figure 3-3b), individual Gaussian kernels (blue curves) were scaled based on their specific fraction of the total amount rather than a uniform ⅙. For example, the sample, which began collection at 9:15 PM, had a $\delta^{18}O$ value of -8.86‰ and an associated amount of 28.2 mm, and thus was scaled by 37.3%, its contribution to the total precipitation amount. Further the next sample collected had a $\delta^{18}O$ value of -6.40‰ and an associated amount of 1.4 mm and was scaled by 1.85%. It is evident this adaptive scaling dramatically influenced the contributions of each event to the total KDE (red curve). Interestingly, the KDE constructed using the Silverman method (black curve) has a bandwidth of

1.15, which is similar to the KDE constructed with a bandwidth of one (red curve), suggesting bandwidth selection may be less important when dealing with weighted KDEs.

Comparison of unweighted and weighted KDEs indicated important differences, which could impact LMWL interpretation for hydrologic investigations (Figure 3-3). In the case of unweighted one-dimensional KDE with a bandwidth selected using the Silverman method (black curve), the KDE showed the highest density of $\delta^{18}O$ near -11‰ and a tail towards less negative values whereas the similar, weighted one-dimensional KDE showed the highest density of $\delta^{18}O$ near -8.4‰ and a more normally distributed shape. These clear differences in mean and shape were directly attributed to the amounts of precipitation associated with each event. Determining the applicability or utility of an unweighted or weighted KDE depends on the research question. In the case of understanding the possible distributions of isotope compositions for a given time or location, an unweighted KDE would be adequate. Occasionally associated precipitation amounts are unavailable in an isotope composition dataset, requiring the use of an unweighted KDE. On the other hand, when associated precipitation amount data is available, and the research question entails precipitation's interaction and contribution to various hydrologic pools, a weighted KDE is likely most applicable.

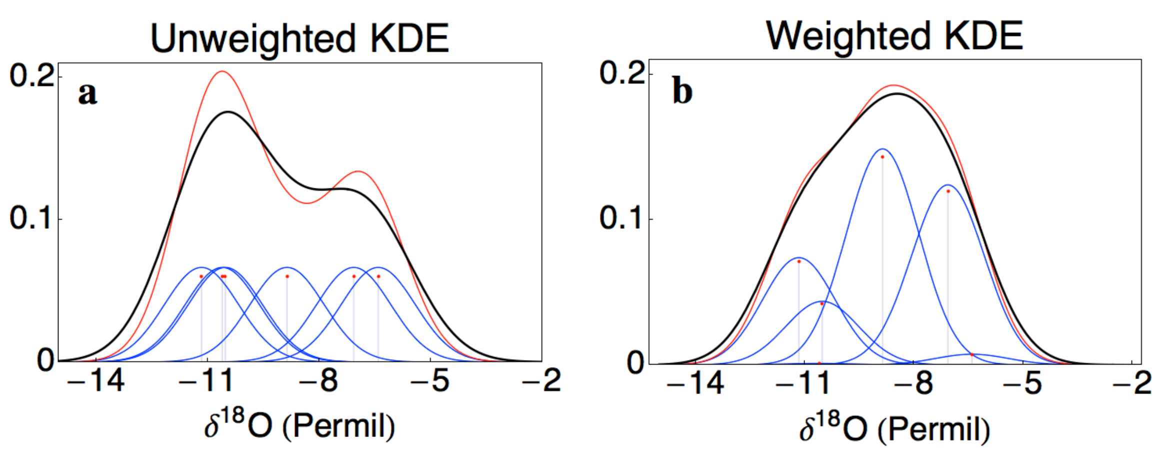

Figure 3-3: One-dimensional kernel density estimations for unweighted (a) and weighted (b) subset of full precipitation dataset. Gaussian kernels (blue curves) are centered over data points (red points) and have a standard deviation equal to one. Summation of individual Gaussian kernels gives kernel density estimation with bandwidth equal to one (red curve). Kernel density estimation with bandwidth selected using Silverman method is shown in black. Distribution shapes change with bandwidth selection and incorporation of precipitation amounts.

Two-dimensional KDEs of precipitation have utility when an understanding of both isotope species can provide information on evaporation processes or connections of precipitation to various hydrologic pools. Before applying this to the full precipitation dataset, assessment of the construction of two-dimensional KDEs for the subset was performed to understand the impact of precipitation amount weighting on the two-dimensional KDEs. Visualization of the two-dimensional KDEs was performed similarly to the one-dimensional KDEs, except, in this case, two-dimensional Gaussian kernels, with differing standard deviations, were centered at the observations. Directional standard deviations of the individual kernels varied because the range of δD observations is approximately eight times larger than that of $\delta^{18}O$. Using the Silverman method for bandwidth estimation, the y-directional standard deviations were set to 11.53 (unweighted) and 10.96 (weighted) and the x-directional standard deviations were set to 1.26 (unweighted) and 1.15 (weighted). This differing directional kernel standard deviation allowed for nearly circular kernels and prevented skewed kernels from complicating the interpretation of the distribution. Additionally, individual kernels were scaled either equally with ⅙ for the unweighted case, or based on their fraction of total precipitation amount for the weighted case. This scaling method follows the same procedure as previously stated in the one-dimensional case. It is can be seen that overlap between individual kernels (Figure 3-4a and 3-3c) begins to provide information on distribution of the isotope compositions but a composite of the individual kernels to a two-dimensional KDE provides the most valuable insight to data distributions (Figure 3-4b and 3-3d). Similar to the one dimensional KDEs, the two dimensional KDEs show clear differences between the unweighted and weighted distributions which suggest incorporation of precipitation amounts can be important for accurate interpretations.

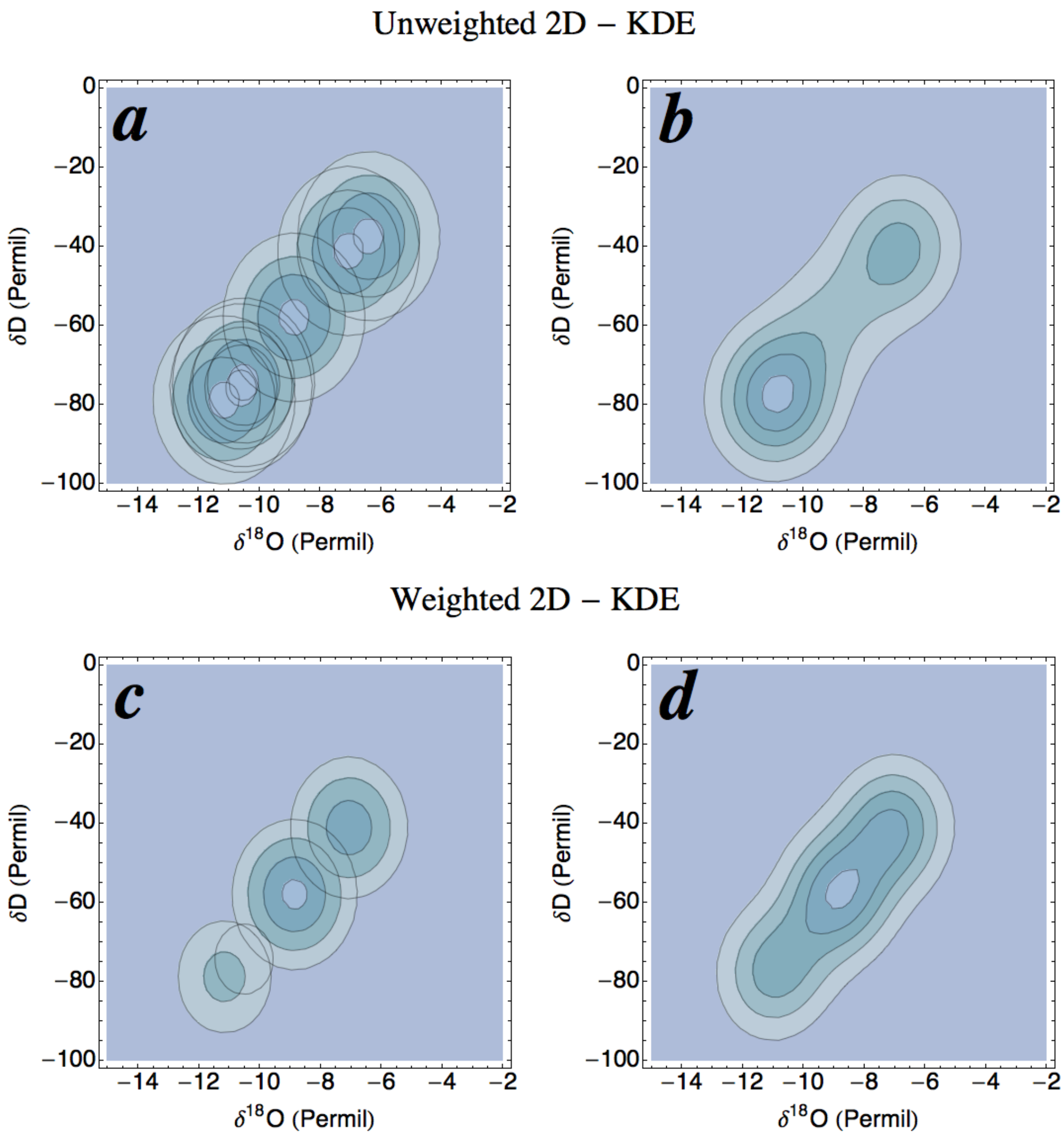

Figure 3-4: Individual two-dimensional Gaussian kernels, with x and y-directional standard deviation estimated using the Silverman method for bandwidth selection, are centered at the observations for unweighted (a) and weighted (c) subsets of full precipitation dataset. Smooth two-dimensional KDEs using Silverman method to estimate bandwidth for the unweighted (b) and weighted (d) dataset show distinct differences in the peak density and shape of distributions.

3.4.2.2. Full Precipitation Record

One-dimensional KDEs and probability density histograms of the full precipitation record show the distribution of isotope compositions is not normally distributed but skewed towards more depleted values (Figure 3-5). The bandwidth, estimated using the Silverman method (Silverman, 1986), was calculated to be 1.31 for the unweighted version and 1.26 for the weighted version. Incorporation of precipitation amounts to the one-dimensional KDEs further pulls the distribution towards the more depleted range. Additionally, the peak density decreases slightly, further increasing the overall spread of the distribution. The δD KDEs (not shown) were constructed and showed similar tendencies. The four-year composite KDEs suggest that highly depleted precipitation events (< -15‰ $\delta^{18}O$) occur less frequently and a large portion of events fall within a range of -8 to -2‰ for $\delta^{18}O$.

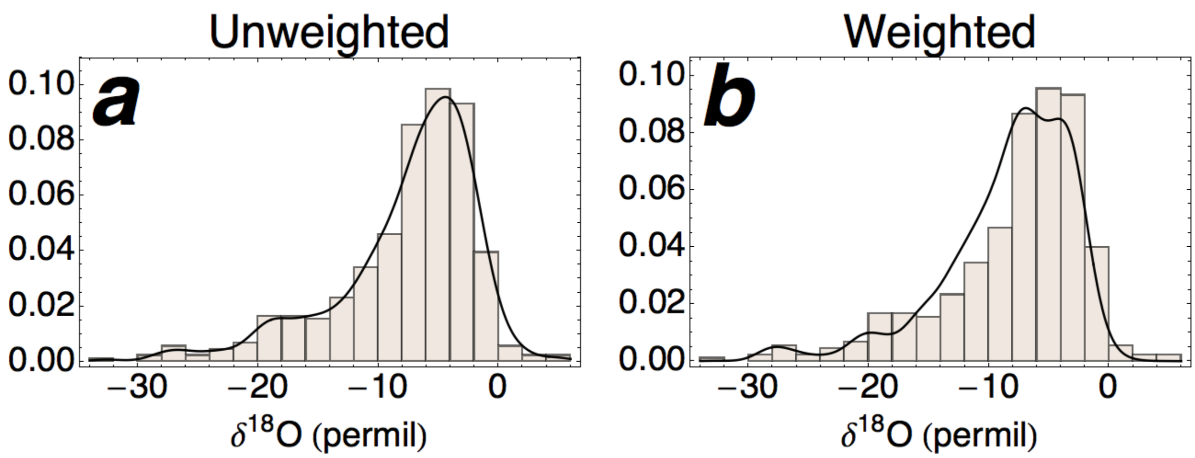

Figure 3-5: One-dimensional unweighted (a) and weighted (b) kernel density estimates and probability density histograms for all observed $\delta^{18}O$ values of precipitation for 2009-2012. Bandwidth selection for kernel density estimates was made using Silverman method. Bin width selection for histograms was made using Freedman–Diaconis' method. Both unweighted and weighted distributions of $\delta^{18}O$ values of precipitation are negatively skewed; yet incorporation of precipitation amounts reduces the peak probability of the kernel density estimate and slightly shifts the distribution towards the more depleted range.

Two-dimensional KDEs for the full precipitation record show similar trends as the one-dimensional KDEs (Figure 3-6). By looking at contours for 95, 90, 75, 50, 25, 10 and 5% quantiles, it is clear precipitation isotope compositions are skewed towards the more depleted values. There appear to be larger differences in contour sizes when moving from 90% to 75% when compared to moving from 25% to 10% which suggests the bivariate distributions have steeper peaks and higher densities near the mean. Sample observations are grouped around the arithmetic mean of -7.66‰ for $\delta^{18}O$ (-52.17‰ for δD) for the unweighted KDE and around the weighted mean of -8.33‰ for $\delta^{18}O$ (-53.87‰ for δD) for the weighted KDE. Differences between the unweighted and weighted bivariate KDEs are small but appear significant. The weighted KDE rotates counterclockwise slightly and shifts further toward the more depleted range. Additionally the peak density is stretched downward, away from the origin. This adjustment of the weighted KDE suggests either large precipitation events are contributing more to the weighted KDE and/or small precipitation events are contributing less. This would imply that unweighted KDEs are insufficient when large variations in precipitation amount are associated with observed isotope compositions.

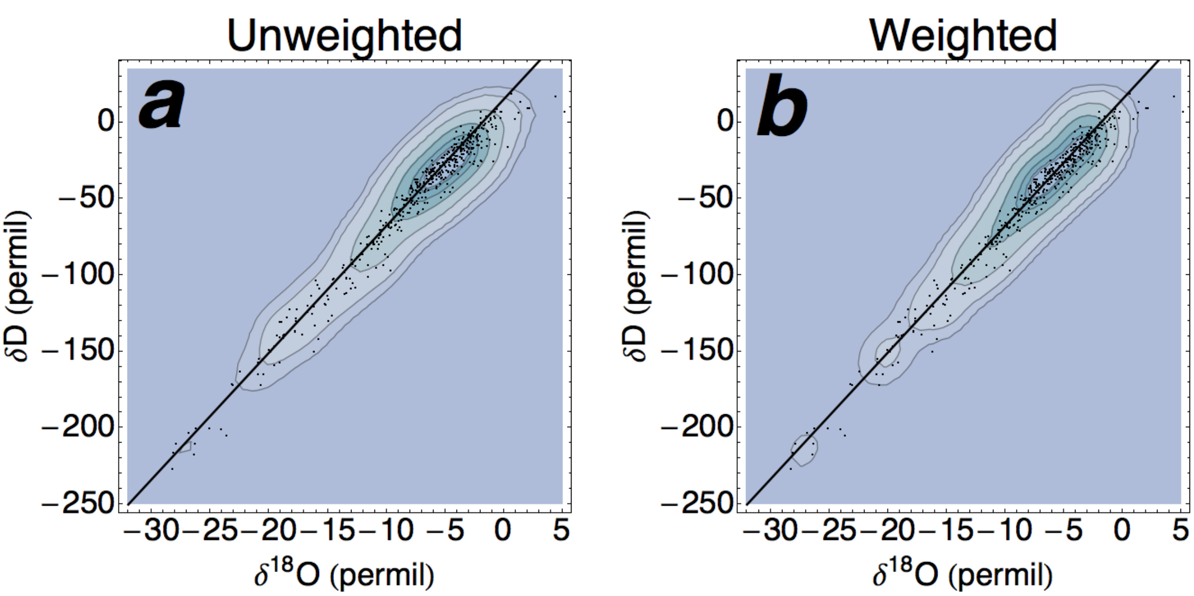

Figure 3-6: Two-dimensional unweighted (a) and weighted (b) kernel density estimates for all observed $\delta^{18}O$ and δD values of precipitation for 2009 – 2012. Bandwidth selection for kernel density estimates was made using Silverman method. Contour intervals correspond to 95, 90, 75, 50, 25, 10, and 5% inclusion quantiles. LMWL calculated using precipitation amount weighted least squares and sample points are shown for reference. Both two-dimensional KDEs show skewness towards more negative values.

3.4.3. Temporal Patterns of Isotopes in Precipitation

The precipitation isotope composition record showed strong seasonal variability through all sub-annual integration periods with more depleted values in the cold season and less depleted values in the warm season (Figure 3-7). As discussed previously, seasonal dependency of isotope compositions is due to a combination of variations in surface temperatures at the moisture source, variable temperatures at the precipitation site, and variations in evaporative fluxes throughout the year (Araguás-Araguás et al., 2000) and these variations become more pronounced at mid to high latitudes (IAEA, 1992). The δD time series show similar trends (data not shown). The sample time series contains large variability within the record and can be seen most prominently in the winter months of 2009-2010 and 2011-2012. Overall the sample time series had a variation of 34.7‰. The daily time series also had large variability with a variation of 34.12‰. Although the sample and daily time series appear nearly identical, it is important to note sample numbers were reduced from the sample to daily time series as numerous samples were collected on a given day and composed a single event. Variability with the record decreases as the time series is integrated to weekly (27.68‰), monthly (18.97‰), and seasonally (7.68‰) amount weighted time series yet the seasonal patterns in isotope compositions remained preserved. Annual amount weighted isotope compositions remained relatively constant for 2009-2012, with the most depleted year being 2009 (-9.46‰ and -64.83‰ for $\delta^{18}O$ and δD respectively).

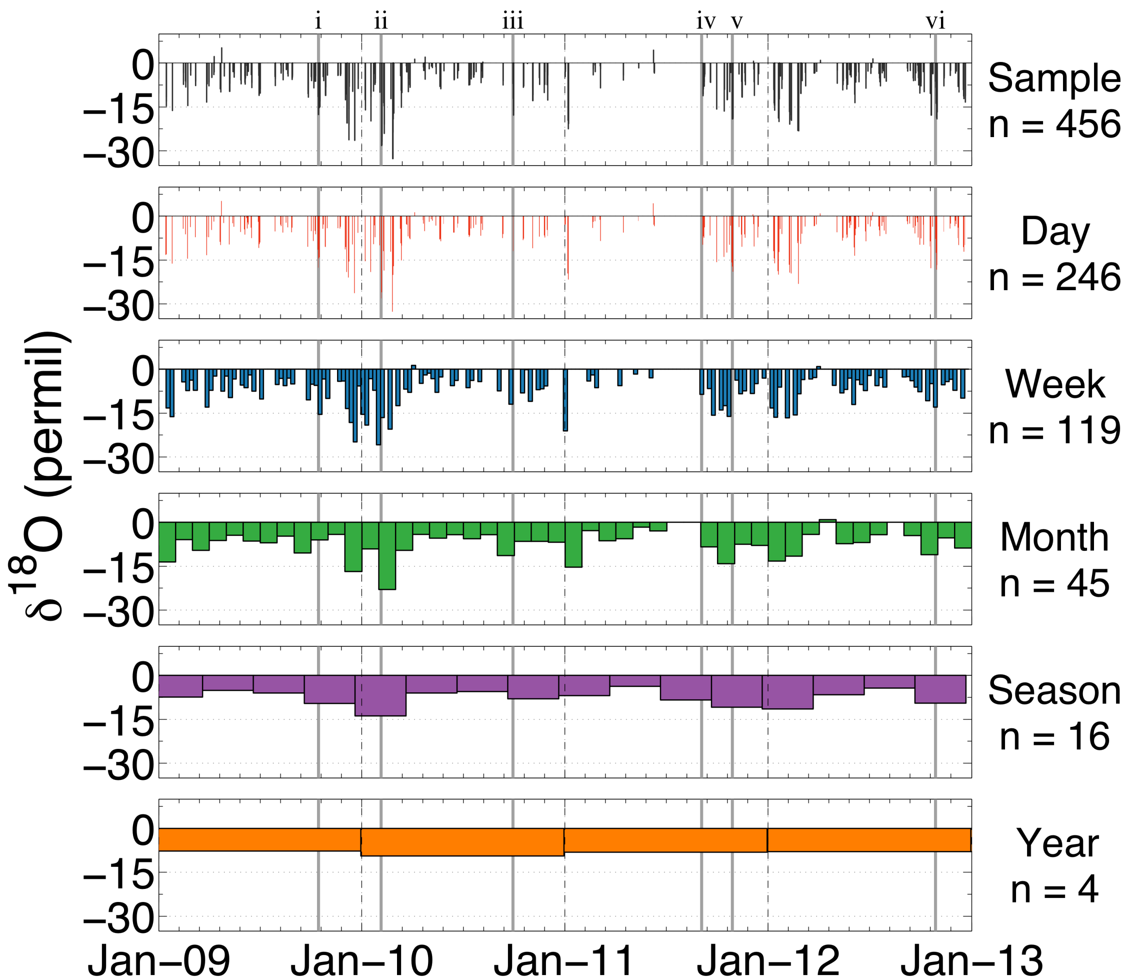

Figure 3-7: Observed $\delta^{18}O$ compositions in precipitation for SSHCZO for 2009 – 2012. Sample compositions were integrated independently to daily, weekly, monthly, seasonally, and yearly amount weighted compositions from individual samples. Major meteorological events are shown as grey bars and correspond to earliest observed snowfall (i), two-day snow event (ii), Tropical Storm Nicole (iii), Tropical Storm Lee (iv), record snow event (v), and Hurricane Sandy (vi). Seasonal variability is preserved through all sub-annual integration periods. Sample, daily, and weekly amount weighted time series contain large variability where as monthly, seasonally, and yearly amount weighted time series are relatively smooth.

A closer investigation of the monthly $\delta^{18}O$ time series revealed interesting temporal patterns in weighted KDEs with respect to precipitation type and origin (Figure 3-8). Aggregation of observations by month and by precipitation type (rain, tropical storm, or snow) provided a large enough dataset to perform robust weighted KDE calculations. As shown above (Figure 3-5), the four-year composite weighted KDE is not normally distributed but is skewed towards more depleted values (right panel, Figure 3-8). Decomposition of the four-year composite to monthly weighted KDEs showed the depleted skew is due to the aggregation of evolving monthly KDEs. Each individual monthly KDE has relatively similar upper bounds on its distribution. That is to say, each month experienced similarly less depleted or slightly enriched precipitation values. On the other end, each month experienced different degrees of depleted precipitation and correspondingly different ranges in precipitation isotope compositions. For example, February clearly had the largest range in observed isotopic compositions while August had the smallest range, yet they had similar upper bounds to the observed isotopic composition.

This variable lower bound is mainly due to snowfall and the corresponding depleted signature. Weighted KDEs for snow for January, February, October and December all showed isotope compositions considerably more depleted than the weighted KDEs for rain for the same month. Aggregation of all snow weighted KDEs for the four observed years contributed a very small amount to the total weighted KDE compared to rain but established the majority of the tail behavior in the four-year composite KDE. Interestingly, only one sample during November of each of the four years was classified as snow. This is not unexpected, as the two October snow events were considered very unusual for central Pennsylvania. The October 15, 2009 snowstorm was the earliest observed snow event for much of Pennsylvania and the October 29, 2011 event was relatively unexpected and caused substantial damage across the region. With additional years of sampling, snow events in November would be expected.

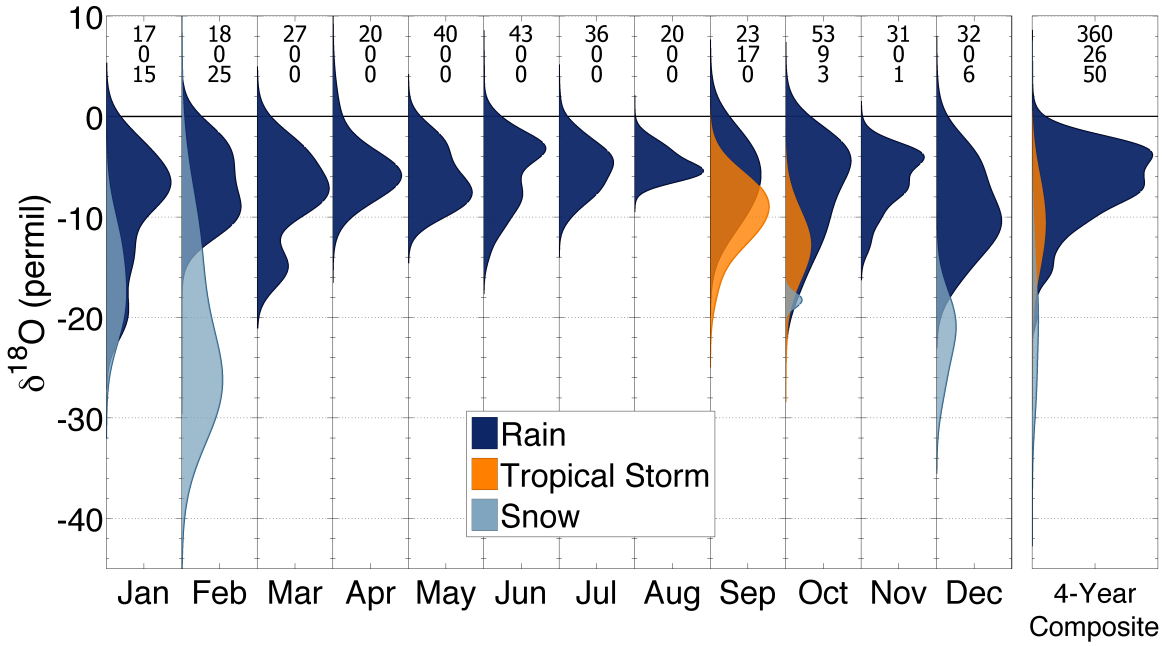

Figure 3-8: Monthly weighted kernel density estimates of precipitation $\delta^{18}O$ values at SSHCZO for 2009 – 2012 and the 4-year composite weighed kernel density estimate. KDEs were constructed using sample $\delta^{18}O$ values and precipitation amounts. The x-axis for each plot has been scaled to allow for clear interpretation of the shape of each KDE. Each KDE for each precipitation type and month has been normalized by amount, therefore the area under all KDEs for a given month is equal to one. Precipitation type was determined using LPM (see text) or by major tropical storm events (Nicole, Lee, or Sandy). Sample number for rain, tropical storm, or snow KDE is listed at the top of each subplot. Based on LPM measurement of "No Precipitation," twenty samples were not included in KDEs.

Tropical storms also appear to play a role in the monthly evolution of weighted KDEs. As discussed previously, there were three significant storms of tropical origin during the four-year monitoring period. Each of the three events, Tropical Storm Nicole, Hurricane Lee, and Hurricane Sandy, occurred during September or October. An additional event, Hurricane Irene, occurred during the end of August 2011 but unfortunately, instrument malfunction prevented sample collection and therefore the data could not be included in these analyses. From the monthly weighted KDEs (Figure 3-8), precipitation from tropical storms is slightly more depleted than the other rains during a given month. This depletion of large precipitation events was likely due to the amount effect. First detailed by Dansgaard (1964), as precipitation amount increases, the isotope composition becomes more depleted in heavy isotopes. Closer investigation of samples from Hurricane Sandy (October 28-30, 2012) show $\delta^{18}O$ compositions progressed from -4.94‰ at 3:41

on Oct. 28 to -19.07‰ at 16:50 on Oct. 30. The impacts of large tropical events on monthly weighted KDEs are significant and appear to pull isotope compositions towards more depleted values.

3.4.4. LMWL Based on Different Integration Periods

Construction of local meteoric water lines for SSHCZO was performed using sample (6 hourly), daily, weekly, monthly, and seasonally amount weighted time series following a ordinary least squares regression procedure (IAEA, 1992). Additionally a LMWL was constructed using sample isotope compositions and precipitation amounts following a weighted linear regression procedure (Hughes and Crawford, 2012). The six different LMWLs provided slightly different interpretations of precipitation isotope compositions (Figure 3-9). From the figure, it is clear that time integration shifts the LMWL to the left by increasing the intercept and slope. Because the daily amount weighted time series is similar to the sample time series (Figure 3-7), both LMWLs have very similar slopes and intercepts and become indistinguishable. Further integration begins to shift the LMWL until the seasonally amount weighted LMWL nearly overlaps the precipitation weighted LMWL. This transition is demonstrated further by looking at the unweighted sample mean and the amount weighted sample mean for the full four-year record. The unweighted sample mean falls directly on the sample and daily amount weighted LMWL while the weighted sample mean falls directly on the amount-weighted LMWL.

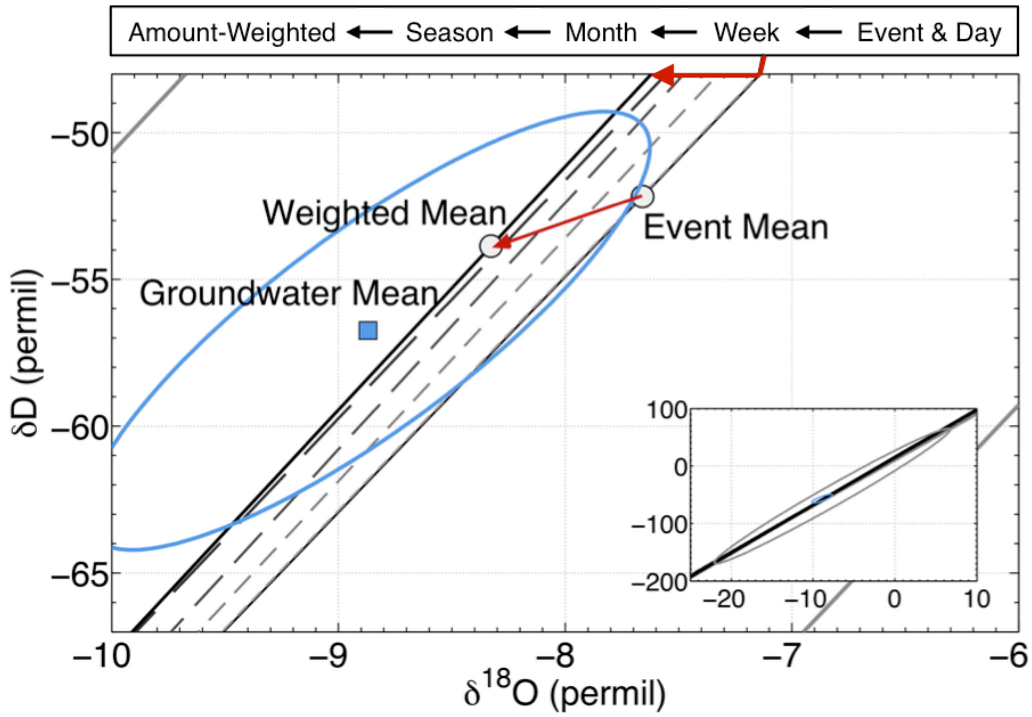

Figure 3-9: Close up comparison of local meteoric water lines for SSHCZO based on different integration periods. Inset figure shows extents of observed isotopic composition of precipitation for 2009-2012. Groundwater ellipse encompassing 95% of observed groundwater isotope compositions is show in both figures for reference. LMWLs defined by individual samples and daily amount weighted values fall directly on each other.

The shift in sample LMWL to seasonally amount weighted LMWL is driven by low amount and low d-excess biases in the sample LMWL (Figure 3-10). During the four-year observation period, sample d-excess (d-excess = δD - 8 x $\delta^{18}O$) varied from -40‰ to 20‰. This variation was constrained to the small amount events. As precipitation amounts increased over 5 mm, d-excess values remained near -10‰. These extreme low d-excess samples contributed dramatically to the lower slopes and intercepts seen in the sample and daily amount weighted LMWLs. Integration to longer time periods wipes out the influence of these small events and results in LMWLs similar to the precipitation amount weighted LMWL. When using individual samples without including precipitation amounts to define the LMWL, researchers are often unknowingly, giving equal importance to each precipitation sample. For some applications this could potentially be useful but for hydrologic applications where researchers are interested in hydrologic response to precipitation, this may not be the correct approach.

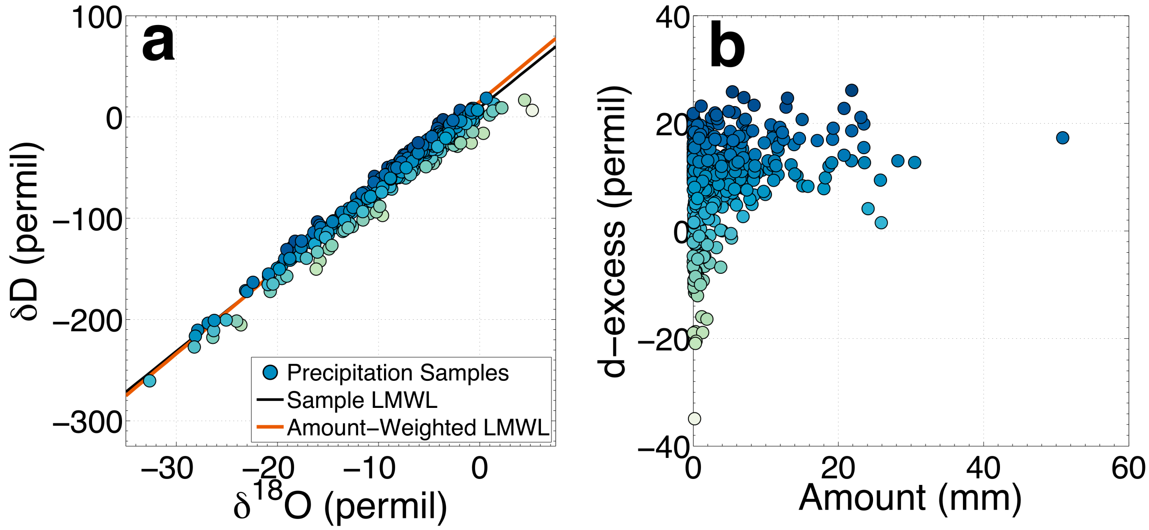

Figure 3-10: Local meteoric water line for SSHCZO (a) defined using least squares regression of individual samples (black line) and amount weighted least squares regression of individual samples (orange line). Comparison of d-excess values and precipitation amount (b) show large negative values associated only with small precipitation amounts. Colors of scatter points correspond to d-excess values, where lighter colors are more negative and darker colors are positive d-excess values.

Table 3-2 shows the sample size, slope, intercept and associated statistics for each LMWL. Although there nearly twice as many observations for the sample time series compared to the daily amount weighted time series, the slopes and intercepts are nearly equal. The sample time series has lower standard deviations for slope and intercept but a lower R^2 value. T-tests for differences in slope between time series and precipitation amount weighted LMWL showed that both the sample and daily amount weighted line have significantly different slopes at all significance levels. Moving to weekly amount weighted LMWL, both the slope and intercept increased along with the standard deviations. The t-test showed the slope of the weekly LMWL is significantly different from the precipitation amount weight LMWL at the 55% level, a level that typically is rejected. This pattern continues for monthly and seasonally amount weighted LMWLs, where slopes and intercepts increase, yet the t-scores are relatively low. This suggests using sample or daily amount weighted values to construct a LMWL will result in a statistically different LMWL than an amount weighted LMWL. Researchers concerned with precipitation impacts and interactions with other hydrologic pools should carefully define the LMWL for the specific question.

Table 3-2: Statistics of local meteoric water lines based on different integration periods and the amount-weighted least squares regression. T-test significance is for the difference in slope between the amount-weighted least squares regression and a given integration period.

Integration Interval	N	Slope ± σ_m	Intercept ± σ_b	R^2	T-score	T-test Significance
Sample	456	8.02 ± 0.07	9.27 ± 0.65	0.9694	4.13	0.00
Day	231	8.02 ± 0.09	9.31 ± 0.90	0.9700	3.15	0.00
Week	116	8.28 ± 0.12	12.67 ± 1.13	0.9757	0.13	0.55
Month	44	8.40 ± 0.18	14.81 ± 1.62	0.9801	-0.50	0.45
Season	16	8.12 ± 0.28	13.36 ± 2.28	0.9837	0.39	0.35
Amount Weighted	456	8.30 ± 0.03	15.24 ± 0.52	0.9821	-	-

In order to clearly visualize this LMWL shift, it was necessary to change the scale dramatically since precipitation isotope compositions inherently have a very large range. To appreciate the scale difference, 95% confidence ellipses for precipitation and groundwater observations at SSHCZO were included for reference in both the main figure as well as the inset figure (Figure 3-9). It is clear the degree of change in LMWLs slope and intercept is relatively small in comparison of the entire precipitation data yet it can play an important role in interpreting isotopic data. Hydrologic pools (soil water, stream water, groundwater, etc.) act as vessels for mixing of water with different isotopic compositions. This mixing is naturally performing a volume-weighted average, which is dependent on a variety of factors including storage volume, residence time, flow rates and others. When these pools are plotted along with the LMWL, the only hydrologic pool not being weighted volumetrically is the high-resolution precipitation samples. Therefore, comparisons between precipitation and other hydrologic pools, without performing amount-weighting operations, could lead to flawed results and interpretations.

3.5. Summary & Conclusion

Through high frequency sampling of precipitation and other meteorological data, numerous temporal patterns have become evident in the isotopic record of precipitation at the SSHCZO. Closer investigation of kernel density estimates and various time series constructed using different integration periods have provided the following conclusions:

1. Univariate and bivariate kernel density estimates of precipitation clearly demonstrate that isotope compositions of precipitation are not normally distributed but rather, are skewed towards more depleted values.
2. Precipitation amount weighted kernel density estimates differ from unweighted kernel density estimates for both the univariate and bivariate scenarios. Application of unweighted versus weighted kernel density estimates should be considered when research questions are attempting to answer hydrologic processes.
3. Integration of samples to daily, weekly, monthly, or seasonally amount weighted time series reduces the variability of the record yet preserves the seasonal pattern of more depleted values in the cold season and less depleted values in the warm season.
4. The shape of monthly amount weighted kernel density estimates is governed by snow and tropical storms, both of which impose more depleted compositions to the distributions. Although snow and tropical storm distributions are distinct from typical monthly rain distributions, they contribute little to the four-year composite kernel density estimate.
5. Distinct local meteoric water lines can be constructed from various integrated time series. Use of appropriate LMWL must be decided prior to analysis.
6. High-resolution sampling captures precipitation events, which contain low d-excess values and low amounts. These events potentially bias the local meteoric water line towards a more evaporative signal.

Although much has been gained from this study, there remain unanswered questions regarding precipitation isotopic composition at SSHCZO and in the region. To fully understand the long-term temporal patterns of isotopes in precipitation, additional sampling must continue at SSHCZO. Daily or weekly bulk sampling would be sufficient at capturing sub-seasonal variability of standard events in central Pennsylvania. Prior to unique events such as tropical storms or large snow events, high-resolution sampling could continue to capture intrastorm variability. Additionally, cross comparisons of precipitation patterns at nearby catchments would validate much of the work completed. Extension of monitoring of stable isotopes in precipitation to other critical zone observatories could further test the findings of this work.

Chapter 4.

Validation of Precipitation Isotope Compositions from an Atmospheric General Circulation Model Using SSHCZO Observations

This chapter will be submitted for publication with co-authors K. Yoshimura and C. J. Duffy.

4.1. Abstract

Datasets of stable isotope compositions in precipitation have been compiled and processed over the past decades to develop large-scale regionally and globally distributed maps of isotopic compositions. Often these data products are then applied to estimate isotopic compositions of precipitation in ungagged basins. This research was intended to determine the feasibility of applying Global and Regional Atmospheric General Circulation Models to determine the long-term hydrologic forcing and isotope composition of precipitation at the watershed scale. Specifically four-years of observations at the Susquehanna-Shale Hills Critical Zone Observatory (SSHCZO) was used to determine the accuracy and precision of three separately modeled time series of isotope composition of precipitation. Comparisons were performed using linear regressions and singular spectrum analysis of daily, weekly and monthly amount weighted isotope compositions. Results show all time-integrated simulations accurately predict seasonal timing of isotope compositions over the four-year record yet slightly under predicts the amplitude of the seasonal variation. The monthly amount weighted time series performed modestly better than the weekly or daily amount weighted values. Singular spectrum analysis on the global and regional models showed the importance of low frequency cycles and the annual cycle and its harmonics. Singular spectrum analysis on the SSHCZO record reinforced the importance of the annual cycle and its harmonics. Reconstruction of modeled 32-year weekly amount weighted time series and 4-year SSHCZO weekly amount weighted time series accounted for 51.78% and 43.44% of the variability respectively, suggesting much of the record is inherent noise. Further work is required to validate modeled isotope compositions in precipitation at other spatial locations around the region as well as possible long-term trends at SSHCZO.

4.2. Introduction

Recent advances in computing power and general circulation models (GCM) have given researchers and hydrologists unprecedented access to high-resolution reanalysis and forecasting data products. With improved resolution and accuracy, scientists now have the opportunity to implement these meteorological datasets as hydrologic forcing for medium and long term distributed hydrologic models over a variety of scales. Additionally advances in isotope age modeling are now providing researchers estimates of the age of waters within small to medium sized basins. For the first time, isotope-incorporated atmospheric general circulation models can be combined with isotope age modeling in distributed hydrologic models to determine the age of water anywhere in space or time within a given basin. The potential utility of this tool is profound. For example researchers can now begin to understand the timescales of hydrologic turnover and residence times for basins of any size and easily relate isotopic age to a variety of physical variables or fluxes calculated by the distributed model. Managers can now also begin to understand the expected lag between implementation of policy and observation of results. The public and other stakeholders can now be educated on the length of time a parcel of water takes to move from a point in a basin to its outlet, a concept previously difficult to describe.

While these opportunities are incredibly exciting and useful to our understanding of distributed hydrology, it is important to understand the data products being used and their potential limitations before moving forward. This study is intended to analyze the validity of an isotope-incorporated atmospheric general circulation model by using observations at one location in space. The two main products this study are a global GCM and its dynamically downscaled regional model both capable of describing stable isotopes in precipitation and their distribution through time and space. Additionally a common empirically based product is investigated as a reference. All simulations are compared against observations at the Susquehanna-Shale Hills Critical Zone Observatory. The objectives of this study are to determine the accuracy of each simulation through three specific time steps: daily, weekly, and monthly values. Also for the first time, model time series are analyzed using singular spectrum analysis to determine the temporal structures and the associated major components of each record.

4.3. Data

4.3.1. Isotope-Incorporated Atmospheric General Circulation Models

4.3.1.1. Global Spectrum Model (IsoGSM)

Time series from two closely related isotope-incorporated atmospheric general circulation models (GCM) were investigated for this study. The global atmospheric GCM is referred to as IsoGSM for isotope-incorporated global spectrum model and provides 200 km x 200 km spatial resolution and six-hour temporal resolution over the entire globe. This physically based model performs numerical reanalysis of atmospheric and meteorological processes (Yoshimura and Kanamitsu, 2008) and is based on NCEP's Medium-Range Forecast Model (Caplan et al., 1997). Liquid and gaseous forms of HDO and $H_2^{18}O$ were incorporated to GSM as passive tracers, which are transported between cells via atmospheric circulation and sub-grid processes. Isotopic species evolution occurs during evaporation and condensation based on Rayleigh distillation. Equilibrium fractionation was assumed to occur during all phase transitions except during evaporation from a free surface, condensation of vapor to ice in supersaturated conditions, or during evaporation of liquid precipitation into dry air mass (Yoshimura and Kanamitsu, 2008; Yoshimura et al., 2008). A 32-year record (1979-2010) for the grid cell (Lon. = 78.75°W, Lat. = 40.95°E) containing SSHCZO was extracted for analysis (Figure 4-1). IsoGSM provides relatively computationally inexpensive distributed data for isotopes in precipitation.

4.3.1.2. Regional Spectrum Model (IsoRSM)

The regional atmospheric GCM is referred to as IsoRSM for isotope-incorporated regional spectrum model and provides 10 km x 10 km spatial resolution and one-hour temporal resolution. The regional model is developed through a dynamical downscaling technique that applies the results of the global simulation and a spectral nudging technique to produce the higher resolution data. For this step, a modification of scale-selective bias correction developed by Kanamaru and Kanamitsu (2007) was performed. The regional spectrum model then utilizes the identical physical parameters as the global spectrum model. Surface pressures, temperatures, humidity, an wind fields were recalculated to account for fine-scale topography and higher-resolution vertical coordinates. Large-scale weather and circulation patterns were incorporated to account for processes larger than the 200 km x 200 km boundary. This process resolves any potential edge effects from the simulation (Yoshimura and Kanamitsu, 2008; Yoshimura et al., 2008). For this study, a 32-year (1980-2011) record for the grid cell containing SSHCZO was extracted for analysis (Figure 4-1). Compared to IsoGSM, IsoRSM provides computationally expensive distributed data for isotopes in precipitation.

4.3.2. Online Isotopes in Precipitation Calculator (OIPC)

A popular tool to predict isotope compositions of precipitation at ungagged locations is the Online Isotopes in Precipitation Calculator (OIPC). The OIPC was used in this comparison as a baseline for understanding the seasonal patterns of isotopes in precipitation and acts a first cut to development of spatially distributed maps of isotopes in precipitation. The OIPC uses an empirical regression incorporating latitude, elevation, and a detrending technique to establish isotope compositions in precipitation over the entire global on monthly time steps (Bowen and Wilkinson, 2002; Bowen and Revenaugh, 2003; Bowen et al., 2005). The detrending technique follows Waliser and Gautier (1993) by transforming monitoring station latitudes into effective monthly latitudes use the globally averaged intertropical convergence zone for a given month. The OIPC utilizes the IAEA's Global Network of Isotopes in Precipitation and the USGS's 5-minute resolution DEM to develop the spatially distributed isoscapes. To monitor the OIPC through time, replicates of the $\delta^{18}O$ and δD monthly values for the SSHCZO location were concatenated to the required length.

4.3.3. Susquehanna-Shale Hills Critical Zone Observatory

Precipitation samples were collected at the Susquehanna-Shale Hills Critical Zone Observatory (SSHCZ) for comparison against the models. Located in central Pennsylvania, the SSHCZO is a small, forested catchment characteristic of the low-laying shale hills in the Ridge and Valley Physiographic Province of eastern United States (Figure 4-1). Elevation of the catchment varies from 310 m at the ridge top to 256 m at the stream outlet. A total of 456 precipitation samples were collected Jan. 14, 2009 to Dec. 20, 2012 on an event basis using an automatic precipitation sampler (model: NSA 181/S, Eigenbrodt GmbH & Co., Königsmoor, Germany) located in a clearing on the ridge top. To capture intra-storm variability, precipitation was collected for the first 30-minutes of a storm followed by three 6-hour intervals. All liquid water samples were collected soon after events and stored in 30 mL amber glass vials with cone-lined caps to prevent evaporation. Sample bottles contained little or no headspace and were stored in a cool location to minimize water-air exchange.

Water samples were analyzed using laser absorption spectrometer (DT-100 Liquid Water Isotope Analyzer, Los Gatos Research, Inc., Mountain View, CA) following the IAEA Standard Operating Procedure (Newman et al., 2008). The analytical precision of the instrument is 0.1‰ and 0.8‰ for oxygen-18 and deuterium, respectively (Lis et al., 2008). The isotopic composition of the water was reported as a δ-value relative to Vienna Standard Mean Ocean Water (V-SMOW):

$$\delta_X(permil) = \left(\frac{R_X}{R_{VSMOW}} - 1\right) \times 1000 \qquad (1)$$

where R is the ratio of deuterium (^2H) to hydrogen (H) or ^{18}O to ^{16}O in the unknown (X) or Vienna Standard Mean Ocean Water (V-SMOW).

Before any analysis, gaps in the SSHCZO record were filled using weekly averages. This was performed by first establishing the full precipitation amount record for 2009-2012. Each week of the year was indexed from 1-52 and a corresponding average weekly amount weighted isotope value was calculated. During the four-year record, two separate indexed weeks contained no observed isotope compositions. In these cases, the isotope composition of the previous week was assigned to the index without an observation. A comparison of observed events and missed events was performed using the full precipitation amount record for 2009-2012. Days without an observed isotopic composition were filled using the weekly amount weighted value based on the index value. Isotope values for days where no precipitation event occurred were filled with zeros.

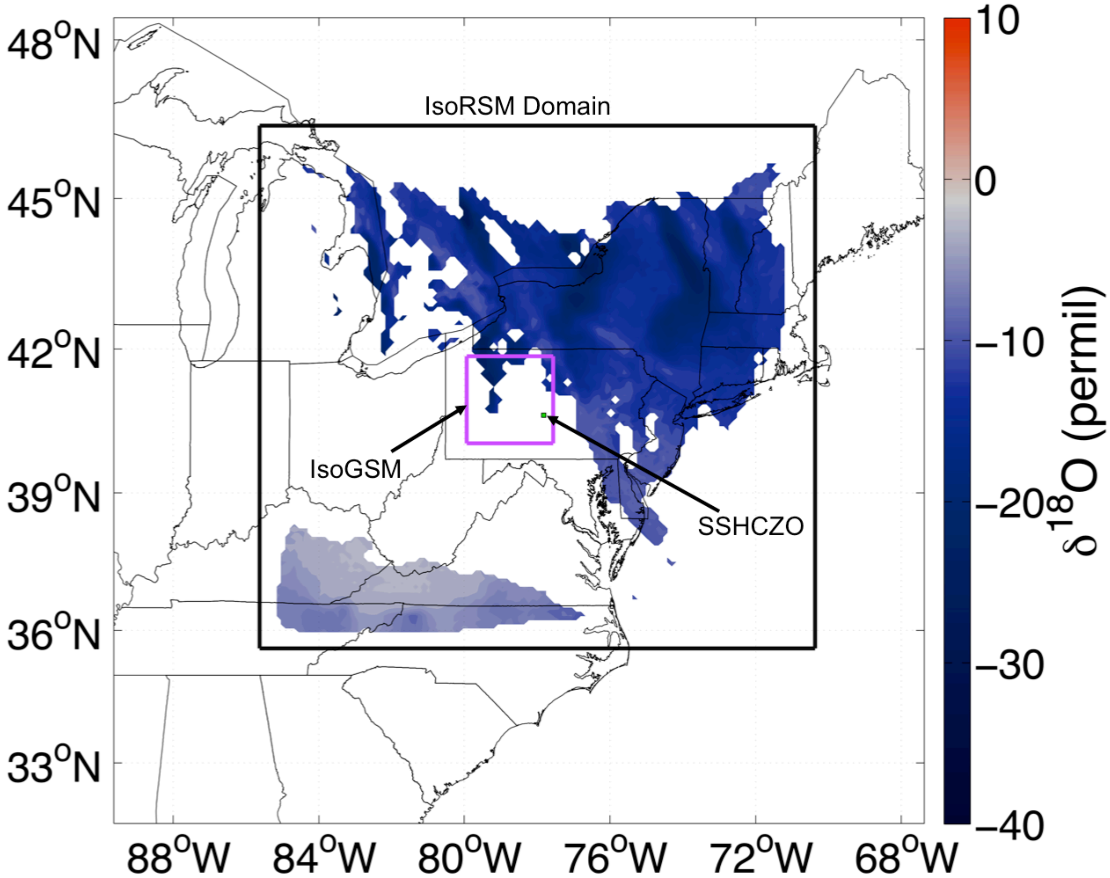

Figure 4-1: Location of SSHCZO (green point) in relation to IsoGSM grid cell (pink square) and IsoRSM domain (black rectangle). IsoRSM domain consisted of 129 grid cells east-west and 120 grid cells north-south. Blue shaded regions correspond to IsoRSM simulated precipitation isotope compositions for an arbitrary day for demonstration purposes only.

4.4. Methods

4.4.1. Time Integration

Time series of varying temporal resolution provide varying degrees of information about the environmental processes in question. High-resolution (daily) values provide insight to atmospheric or hydrological processes, which occur over periods of days to weeks. On the other hand, monthly values can provide insight to seasonal dynamics of water storages. Because the data records contain a wealth of information through various time scales, this study is intended to assess the quality of these data at different time integration intervals. In order to more fully understand the temporal structure of the models and the SSCHZO record, each time series was time averaged to daily, weekly, or monthly amount weighted values using the following equation:

$$\delta_T = \frac{\sum_{i=1}^{n} P_i \delta_i}{\sum_{i=1}^{n} P_i} \tag{2}$$

where δ_T is the amount-weighted precipitation value, P_i represents the amount (depth) of precipitation in an event, δ_i is the isotope composition of an event, and n is the number of events in the time period considered. The time integration procedure was not preformed on the OIPC time series, as monthly values were the highest resolution data available.

4.4.2. Regression Procedures

Models were compared against the SSHCZO $\delta^{18}O$ and δD values using linear regressions and Nash-Sutcliffe coefficients on daily, weekly, and monthly amount weighted isotopic compositions. The IsoGSM and IsoRSM models were compared for daily, weekly, and monthly amount weighted values while the OIPC was only compared for the monthly values. IsoGSM was compared for only 2009 and 2010 because of limited length of IsoGSM record. IsoRSM and OIPC were compared for 2009 through 2011. Model values were compared against observations only when observations occurred. In other words, if in a certain time step a model predicted a precipitation event but the filled SSHCZO record did not contain an event, the model value is left out of the regression. For time steps when the SSHCZO record contained an event and the model did not, model values of zero were included in the regression. This procedure gives a rigid account of performance with respect to the observed record.

Linear regressions provide information towards the general performance of each model. A slope of one refers to perfect agreement between model and observation. A slope less than one suggests under prediction of isotopic range for the model while a slope greater than one suggests an over prediction of isotopic range. A larger intercept suggests a bias towards less depleted compositions while a smaller intercept suggests a bias towards more depleted values. R-squared values were also calculated to estimate the overall variability of the model-observation regression. R-squared values near one suggest a strong linear relationship (not necessarily strong model-observation agreement), while values near zero suggest poor linear relationship (not necessarily poor model-observation agreement).

To better understand the overall model efficiency Nash-Sutcliffe coefficients for each comparison were calculated. The Nash-Sutcliffe efficiency coefficient (NSE) compares the residual noise to the variance of the observations using the following equation:

$$NSE = 1 - \frac{\sum(\delta_O - \delta_M)^2}{\sum(\delta_O - \overline{\delta_O})^2} \tag{2}$$

where δ_O is the observed isotopic value, δ_M is the modeled isotopic value, and $\overline{\delta_O}$ is the arithmetic average observed isotopic value (Nash and Sutcliffe, 1970). NSE values equal to one suggest perfect match between modeled and observed isotopic composition. Values less than zero suggest the model does no better than the observed mean at predicting isotopic compositions.

4.4.3. Singular Spectrum Analysis (SSA)

4.4.3.1. SSA Background and Motivation for Use

To determine the temporal structure of IsoGSM and IsoRSM, singular spectrum analysis (SSA) was performed on the 32-year daily, weekly, and monthly amount weighted $\delta^{18}O$ and δD time series for both IsoGSM and IsoRSM. Here, temporal structure refers to important trends or oscillations within the record as well as the structure of the residual noise. The results were then compared against SSA of daily and weekly amount weighted $\delta^{18}O$ and δD for SSHCZO. In all, SSA was performed on a total of 16 time series. Note the records for IsoGSM (1979-2010), IsoRSM (1980-2011), and SSHCZO (2009-2012) do not completely overlap. SSA was performed on the longest available record in order to capture the longest cycles imbedded within the time series. Pioneered by the work of Broomhead and King (1986), SSA is a data-based signal processing method which deconstructs a time series into its three main components: trend, signal and noise. SSA has numerous advantages over other time series analysis tools, mainly it is not limited to sines and cosines and its basis functions are data-adaptive, empirical, and orthogonal. In other words, SSA efficiently determines the fewest number of components to capture the most variance. It is our intent to use SSA to understand the important components within each model time series and compare them to the important components of the SSHCZO observations. This comparison should inform us on the efficiency of model predictions as well as where models need improvement.

4.4.3.2. SSA Procedure

There are four steps involved in SSA: embedding, spectral decomposition, principle component computation, and reconstruction. Before we begin let's assume we have a time series $X = (x_1, \cdots, x_N)$, with no gaps. The first step, embedding, constructs a trajectory matrix from the original time series:

$$\boldsymbol{T_x} = \begin{bmatrix} x_1 & x_2 & x_3 & \cdots & x_K \\ x_2 & x_3 & x_4 & \cdots & x_{K+1} \\ x_3 & x_4 & x_5 & \cdots & x_{K+2} \\ \vdots & \vdots & \vdots & \ddots & \vdots \\ x_L & x_{L+1} & x_{L+2} & \cdots & x_N \end{bmatrix} \tag{3}$$

where L is the window length and $2 < L < \frac{N}{2}$. The second step performs singular value decomposition on the trajectory matrix. This is done by finding the eigenvectors (U_i) of the lagged covariance matrix $\boldsymbol{S} = \boldsymbol{T_x}\boldsymbol{T_x}'$, and sorting the corresponding eigenvalues (λ_i) in descending order. In the third step, the eigenvectors are projected onto the original time record to produce the principle components. The fourth step consists of reconstructing the signal by convolving one or more of the principle components with the corresponding eigenvectors (Vautard et al., 1992; Elsner and Tsonis, 1996; Golyandina et al., 2001).

The most important parameter for SSA is the window length, as it determines the longest cycle that can be resolved within the record. Typically window lengths vary between 10-40% of the series length. For this study, a variety of window lengths were investigated and lengths of 10 years were chosen for IsoGSM and IsoRSM and 2 years for SSHCZO. For the daily time series this became a window length of 3650 (10-years) or 730 (2-years), for the weekly time series the window length was 520 (10-years) or 104 (2-years), and for the monthly time series the window length was 120. The lengths were chosen to balance number and resolution of major oscillatory components. The dominant frequency of each eigenvector w determined by performing fast Fourier transforms and extracting the most significant frequency. This procedure is most effective for well-resolved eigenvectors, which have clear oscillatory patterns. Statistically significant eigenvalues were determined by applying a red noise filter to the spectrum. This procedure was performed manually on each eigenspectrum to establish a rough cutoff of significant components from the noise. Confidence bounds for the noise spectrum were calculated to correspond to 2.5 and 97.5%. Values which fell above the upper confidence bounds were considered statistically significant components of the signal while values that fell below the lower confidence bounds were contributed very little to the overall variance of the record. Values within the confidence bounds correspond to the red noise spectrum. Reconstructions were performed with significant components of the record as well as manually chosen components, which were near the significance level.

4.5. Results & Discussion

Daily, weekly, and monthly amount weighted $\delta^{18}O$ time series for IsoGSM, IsoRSM, and SSHCZO showed varying degrees of variability (Figure 4-2), with more variability in the daily record and less variability in the monthly record. Similar patterns were evident for δD values through time. All time series showed similar patterns of more depleted values in the winter and less depleted values in the summer. In general, IsoGSM had less depleted values compared to SSHCZO while IsoRSM had more depleted values. The OIPC values matched relatively well with SSHCZO but contained no interannual variability as the 12 month record was repeated for the 34 years. The long-term averages of each time series showed clear seasonality with the SSHCZO containing the most variability. It is safe to assume that with a longer observation record, much of the variability in the long-term average of SSHCZO would be reduced.

The daily time series for IsoGSM, IsoRSM, and SSHCZO contained numerous values equal to zero, which could pose a problem as they represented days with no observed precipitation yet contain numeric values. Physically speaking, an isotopic composition equal to zero means the concentration of rare isotopes in the sample is equal to that of ocean water. Artificially assigning isotope compositions of zero to days without precipitation events potentially introduces an error, which could propagate through the analysis. Zeros were also observed in the weekly amount weighted $\delta^{18}O$ time series, but were much less frequent, and integration to monthly time series completely removed the zero observations.

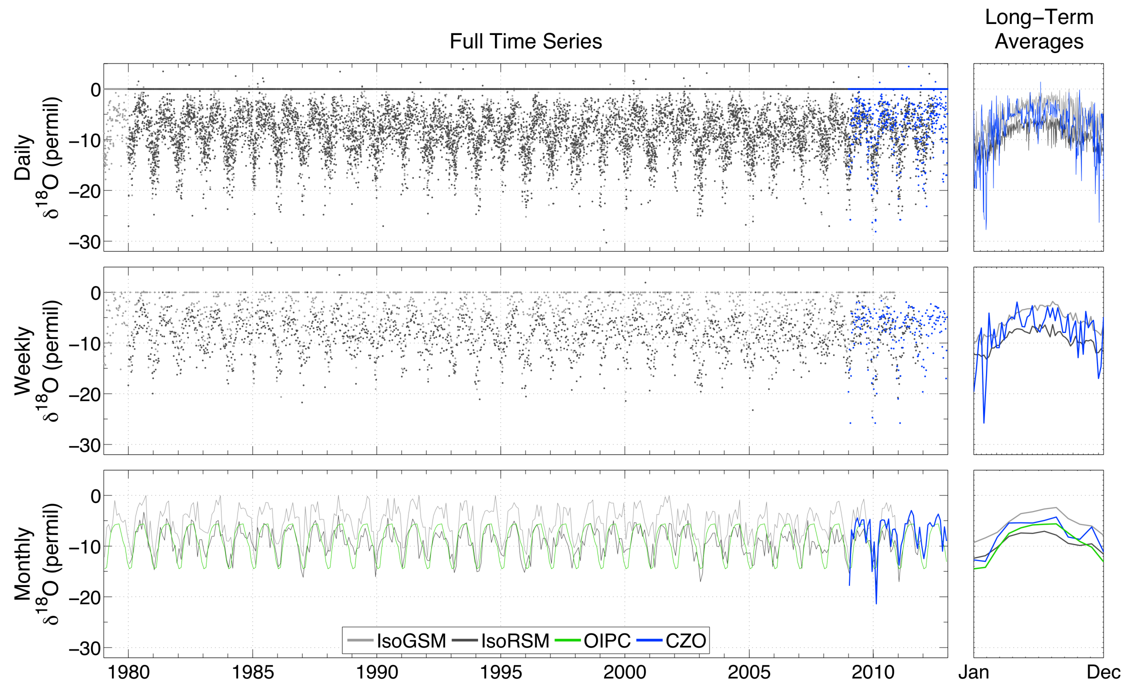

Figure 4-2: Daily, weekly, and monthly amount weighted time series for IsoGSM (light grey), IsoRSM (dark grey), OIPC (green), and SSHCZO observations (blue). Long-term averages are shown for each time period (right panels).

4.5.1. Regression Results

Comparisons of $\delta^{18}O$ values for each simulation against the observations at SSHCZO shed light on the efficiency of each model over various time steps (Figure 4-3). Daily amount weighted values for IsoGSM and IsoRSM did a similar job at predicting observed isotope compositions. R-squared values and regression parameters are nearly identical for models at the daily time step. Neither model adequately captured the range of isotopic values seen in the observed record, a fact demonstrated by the regression slopes being less than one. Nash-Sutcliffe efficiency coefficients suggest the IsoGSM (NSE = 0.3037) better predicts isotope composition when compared to IsoRSM (NSE = 0.1797), but neither provide strong representations of daily amount weighted observed compositions at SSHCZO. Comparison of δD values was also performed and showed similar trends.

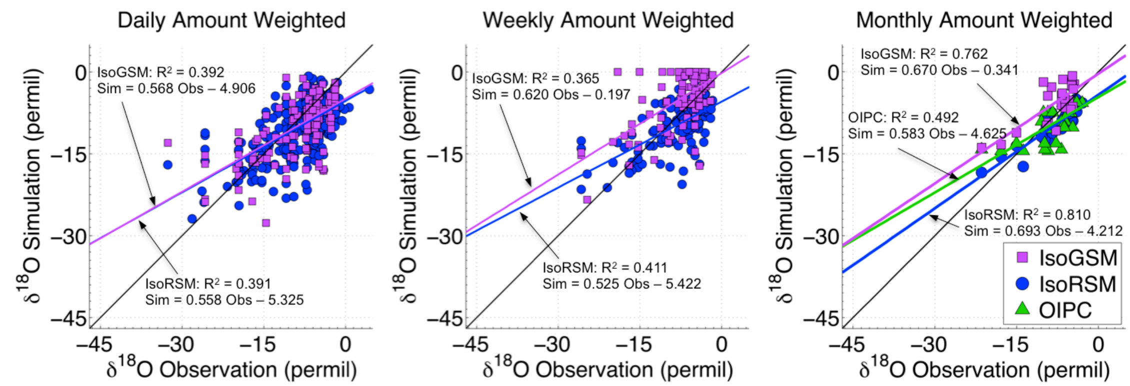

Figure 4-3: Comparison of IsoRSM (blue), IsoGSM (pink), and OIPC (green) for daily, weekly and monthly amount weighted $\delta^{18}O$ values. The OIPC was compared for the monthly time series only. One-to-one line (black) is shown for reference.

Integration to the weekly time step differentiates the two models slightly (Figure 4-3). Using the slope of the linear regressions to understand performance, IsoGSM better captured the isotopic range when compared to IsoGSM. But at the same time, IsoGSM appears to have gained a bias towards less depleted values, evident through the increased intercept of the IsoGSM weekly regression. The likely cause of the less depleted bias is the numerous composition equal to zero (Figure 4-2) and thus pulling the regression upward. The weekly record for IsoRSM contained less zeros and therefore did not have a similar bias as IsoGSM. NSE values for IsoGSM (NSE = -0.0806) and IsoRSM (NSE = 0.2604) suggest the weekly amount weighted models do not improve the prediction of isotope compositions. Interestingly based on the NSE value, the weekly integrated IsoGSM does no better predicting isotope compositions than the average observed value.

Further integration to the monthly time step improves the model performance over the daily or weekly amount weighted values (Figure 4-3). Overall the IsoRSM model had the highest slope and thus did the best at capturing the isotopic range observed. Further the R-squared value of the IsoRSM model was relatively large suggesting a strong linear relationship between the model and the observations. NSE values further supported the IsoRSM as the strongest model with a NSE value of 0.5792 compared to IsoGSM value of 0.2807 and OIPC value of 0.3882. Table 4-1 shows summary statistics for each comparison. From these comparisons the monthly amount weighted IsoRSM values performed the strongest when compared to the remainder of the models.

Table 4-1: Summary statistics for comparisons of SSHCZO daily, weekly, and monthly amount weighted values against IsoRSM, IsoGSM, and OIPC.

Integration Period	Simulation vs. CZO	Slope	Intercept	R^2	Nash-Sutcliffe
Day	IsoRSM	0.558	-5.325	0.391	0.1797
	IsoGSM	0.568	-4.906	0.392	0.3037
Week	IsoRSM	0.525	-5.422	0.411	0.2604
	IsoGSM	0.620	-0.197	0.365	-0.0806
Month	IsoRSM	0.693	-4.212	0.810	0.5792
	IsoGSM	0.670	-0.341	0.762	0.2807
	OIPC	0.583	-4.625	0.492	0.3882

4.5.2. SSA Results

4.5.2.1. IsoGSM

The normalized eigenvalue spectrum for the 32-year IsoGSM record (1979-2010) showed important oscillatory components imbedded within the record (Figure 4-4). The red noise spectrum was also shown with its associated 95% confidence intervals. Eigenvalues above the 95% confidence intervals were considered significant components of the signal while the remaining eigenvalues made up the noise. With a 10-year window, numerous significant components were extracted from the daily, weekly, and monthly time series for both $\delta^{18}O$ and δD. For the daily record, significant values were found for the 10-year, 2.5-year, 2-year, 1-year, 0.5-year, 0.37-year, 0.25-year, and 19-day cycles. Additional components were found to be significant but either fell on or just above the confidence bounds of the noise spectrum or were high-frequency and considered less important to the overall spectrum. These high frequency components represented cycles on the order of days or weeks. Each significant eigenvector shown in Figure 4-4 corresponded to a pair of eigenvalues. Similar eigenvalues were found for $\delta^{18}O$ and δD with the exception of high frequency components considered to be less important. For both spectrums, the 1-year and 0.5-year cycles represented the most variance within the record corresponding to approximately 22% of the variance. Eigenvalues which corresponded to 0.5 and 0.25-year cycles represent harmonics of the annual while the 10, 2.5, and 2-year cycles account for interannual variability in the record.

Integration to the weekly amount weighted time series reduced the total number and number of significant eigenvalues (Figure 4-4). With the 10-year window, significant values were found at the 10-year, 1-year, 0.8-year, 0.5-year, and 0.25-year as well as at higher frequencies, which again were considered less important to the overall spectrum. The same significant eigenvalues were found to be significant for both $\delta^{18}O$ and δD. Again the annual and its harmonics were the strongest eigenvalues evident within the record and accounted for approximately 22% of the variance.

Further integration to monthly amount weighted time series further reduced the number of eigenvalues (Figure 4-4). The only significant eigenvalue pair found using the 10-year window was the annual cycle with the 10-year, 2-year, and 0.5-year falling just below the confidence bounds of the red noise spectrum. Combined, the annual eigenvalues accounted for approximately 30% of the variance within the monthly amount weighted time series.

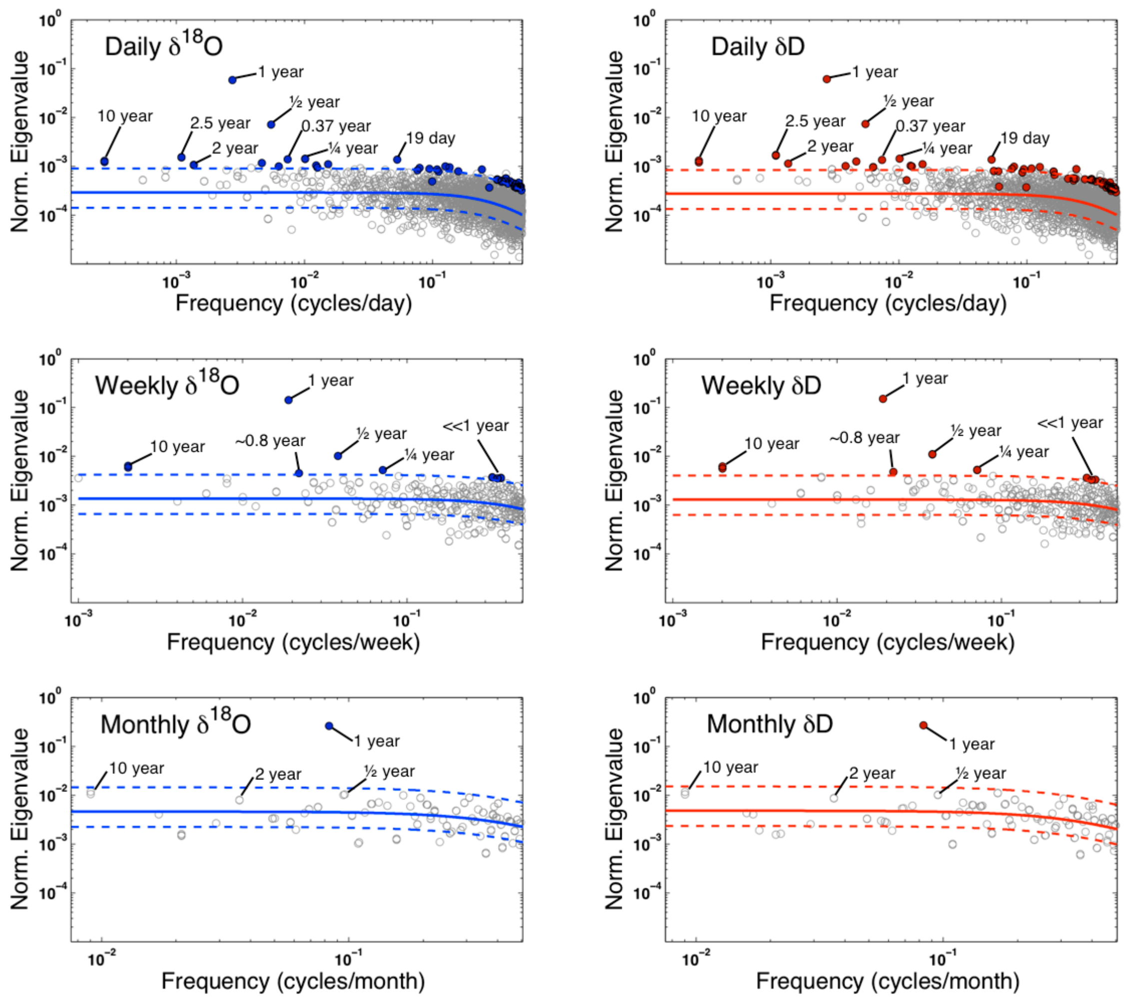

Figure 4-4: Eigenspectrum for daily, weekly, and monthly amount weighed $\delta^{18}O$ (blue) and δD (red) values of IsoGSM. Colored circles represent significant paired oscillatory or trend components. Solid line represents red noise floor and dashed lines correspond to 97.5 and 2.5%

confidence bounds. The embedding dimension was 10 years for each time series (3650 days, 520 weeks, or 120 months).

The significant eigenvectors, from the eigenspectrums, had clear sinusoidal shapes, which further validated their importance to describing each record (Figure 4-5). The eigenvectors, which represented the annual cycle, had the largest variance for each respective record. Variance of annual cycles increased from daily to weekly to monthly time series. This increase in proportion of variance was due to the decreasing number of eigenvectors associated with each time series. Because the monthly time series had 120 eigenvectors and the daily time series had 3650 eigenvectors, and the sum of the variances from all eigenvectors must equal one, each eigenvector from the monthly time series must account for proportionally more variance. Additionally the annual eigenvectors displayed no amplitude modulation throughout their series, suggesting they represented the pure seasonal components of the record. The near significant components of the monthly time series of IsoGSM were shown in grey (Figure 4-5). It is clear they contained important aspects of the record but have not been fully resolved by the SSA procedure. This poor resolution was likely due to the limited number of points within the record. With a longer monthly record, it is likely the near significant eigenvectors would be resolved and become significant components of the record.

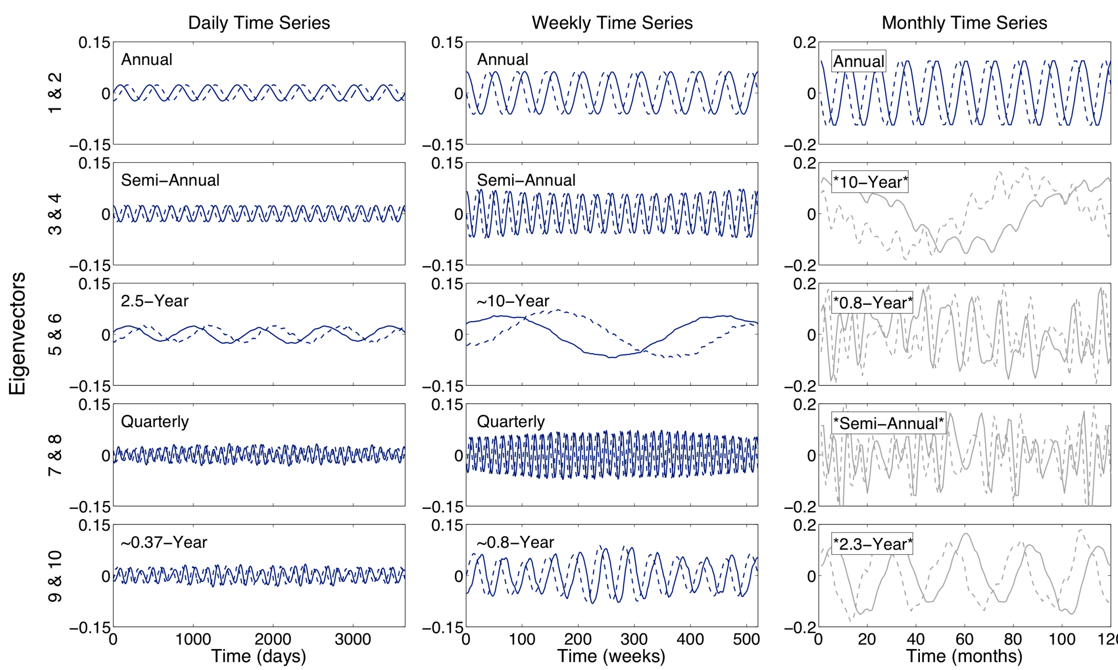

Figure 4-5: Significant eigenvectors from SSA analysis of daily, weekly, and monthly IsoGSM time series. The first five pairs of eigenvectors represented the largest portion of variance for daily and weekly time series. Only the first pair of eigenvectors was considered significant for the monthly time series the remainder of the eigenvectors were near significant (grey).

4.5.2.2. IsoRSM

Eigenspectrum for the regional spectrum model, IsoRSM (Figure 4-6), showed similar patterns as the eigenspectrum for IsoGSM. With respect to the daily $\delta^{18}O$ time series, significant eigenvalues were found at the 10-year, 2.5-year, 2-year, 1-year, 0.5-year, 0.3-year, and 0.25-year frequencies. Numerous eigenvalues fell just above the red noise significance level and represented cycles with frequencies less than a month. Similar eigenvalues were found for the δD time series. Similar to the IsoGSM eigenspectrum, time integration to weekly amount weighted values reduced the number of significant eigenvalues observed. For both the $\delta^{18}O$ and δD time series, eigenvalues representing the 10-year, 2.75-year, 1.75-year, 1-year, 0.8-year, and 0.5-year frequencies were found to be significant. Time integration to monthly amount weighted values further reduced the number of significant eigenvalues to the 1-year, 0.5-year, and 4-month frequencies. With time integration, significant eigenvalues of the daily and weekly time series become less significant in the monthly time series. As discussed above, the reduced significance of major eigenvectors is due to the decreased record length and poorer resolution of eigenvectors.

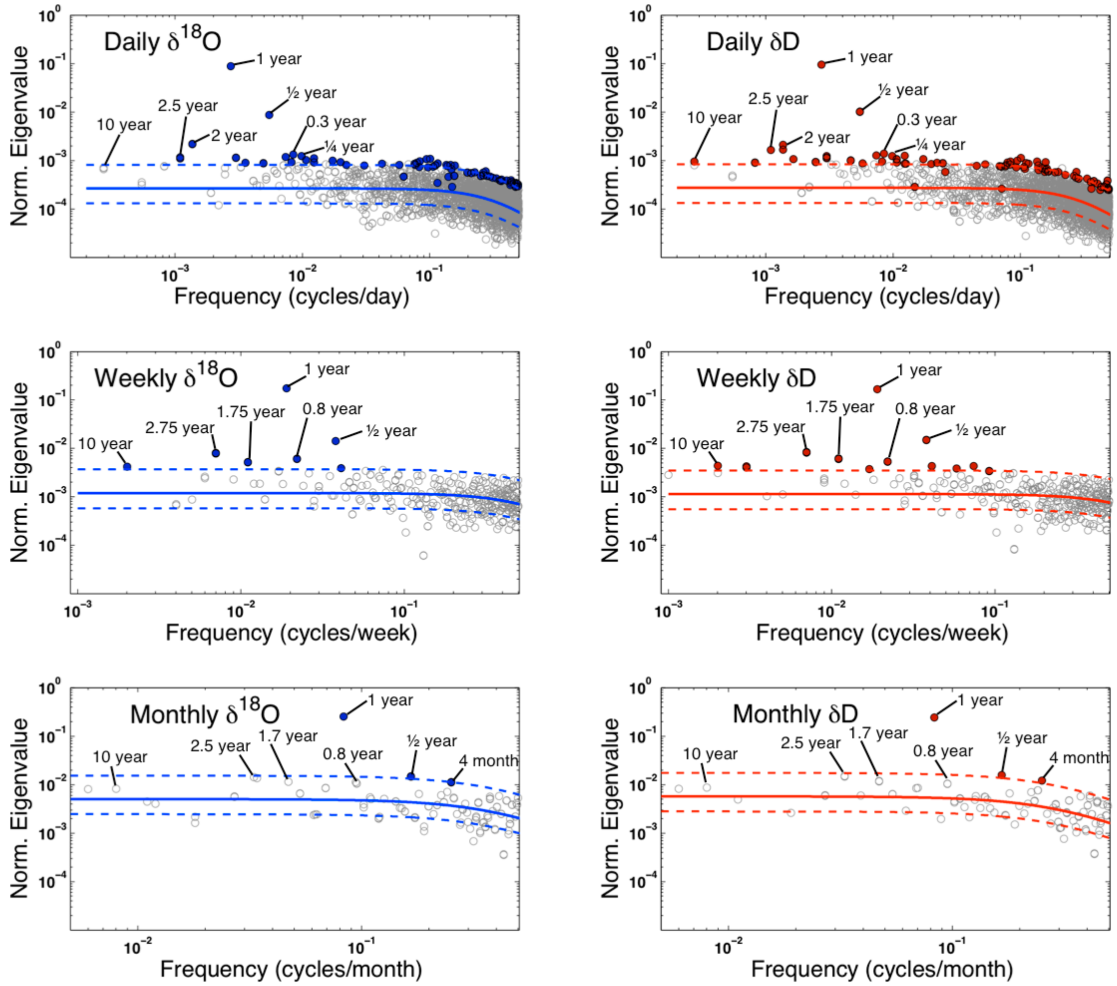

Figure 4-6: Eigenspectrum for daily, weekly, and monthly amount weighed $\delta^{18}O$ (blue) and δD (red) time series of IsoRSM. Colored circles represent significant paired oscillatory or trend components. Solid line represents red noise floor and dashed lines correspond to 97.5 and 2.5% confidence bounds. The embedding dimension was 10 years for each time series (3650 days, 520 weeks, or 120 months).

Significant eigenvectors for IsoRSM (Figure 4-7) were similar to the significant eigenvectors of IsoGSM (Figure 4-5). All eigenvectors falling above the confidence levels of the red noise spectrum were well resolved and clearly contained sinusoidal oscillations. Due to the large number of eigenvalues of the daily time series, each significant eigenvector represents only a small portion of the overall record variance for reasons discussed above. On the other hand, significant eigenvectors (1-year, 0.5-year, and 0.3-year) for the monthly time series accounted for substantially more variance. Monthly eigenvectors, which fell just below the red noise spectrum confidence levels (2.5-year, 1.7-year, and 0.8-year), were poorly resolved but were considered significant for the daily and weekly time series. This suggests that with a longer record, better resolution would improve the importance of these cycles.

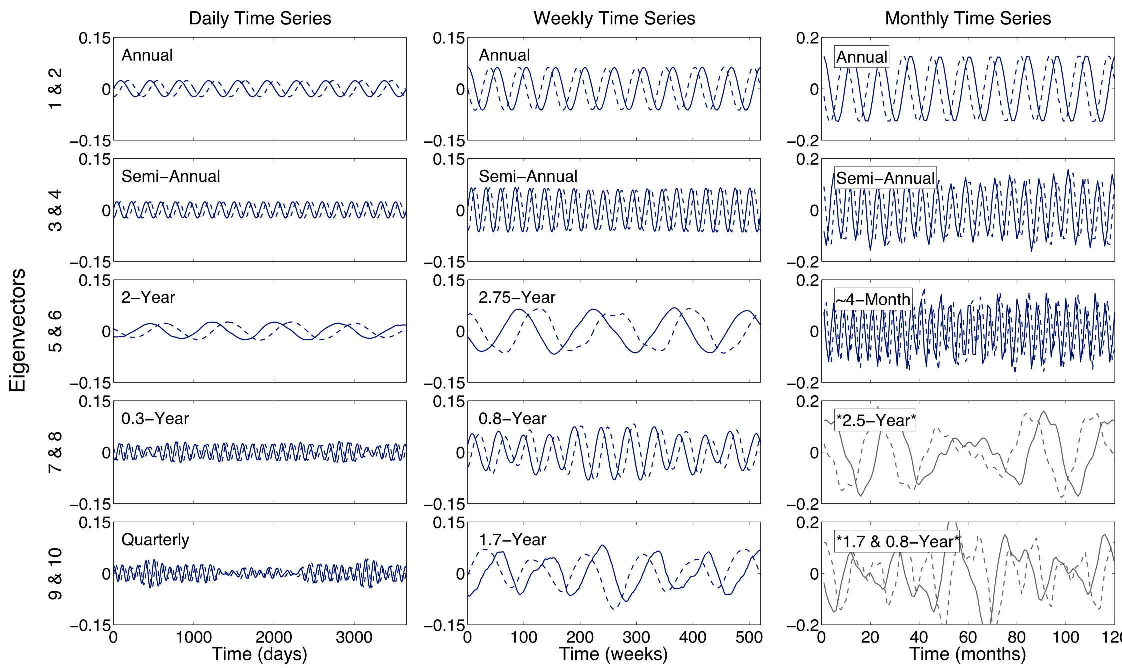

Figure 4-7: Significant eigenvectors from SSA analysis of daily, weekly, and monthly $\delta^{18}O$ IsoRSM time series. The first five pairs of eigenvectors represented the largest portion of variance for daily and weekly time series. The first three pairs of eigenvectors were considered significant for the monthly time series. Eigenvectors in grey were not statistically different from the red noise spectrum but considered important components of the time series.

4.5.2.3. SSHCZO

Eigenspectrum for daily and weekly time series of the SSHCZO (Figure 4-8) contained a fewer number of significant eigenvalues than the eigenspectrum for IsoGSM or IsoRSM. From the models' longer-term records, significant frequencies were found for the annual, semi-annual and quarterly cycles for all time integration periods. For daily and weekly amount weighted time series, low frequency components were also found to be significant in the models. The question then becomes do these significant oscillations exist in the observed isotope record or are they an artifact of the modeling procedure. While it is difficult to definitively answer the latter question, investigation of the eigenspectrum for SSHCZO can shed light into which significant frequencies exist in the natural record. From the daily eigenspectrum (Figure 4-7), the 2-year and 1-year eigenvalues contribute the most to the overall record's variance. Other important frequencies appeared to be the 26-day, 12-day, and 0.3-year. Interestingly, the 5-year cycle appears in the $\delta^{18}O$ time series but not the δD. Because the windowing length was set as 2-years, the maximum frequency which could be resolved was 2-years, any frequencies longer than 2-years are not considered well resolved. For the weekly time series, the 1-year, 0.5-year, and 0.3-year frequencies were important with other high frequency components contributing to the overall variance. This suggests the annual, semi-annual, and 4-month cycles are relatively important to the overall record. With a longer time series, it would be possible to extract additional low frequency components from the record.

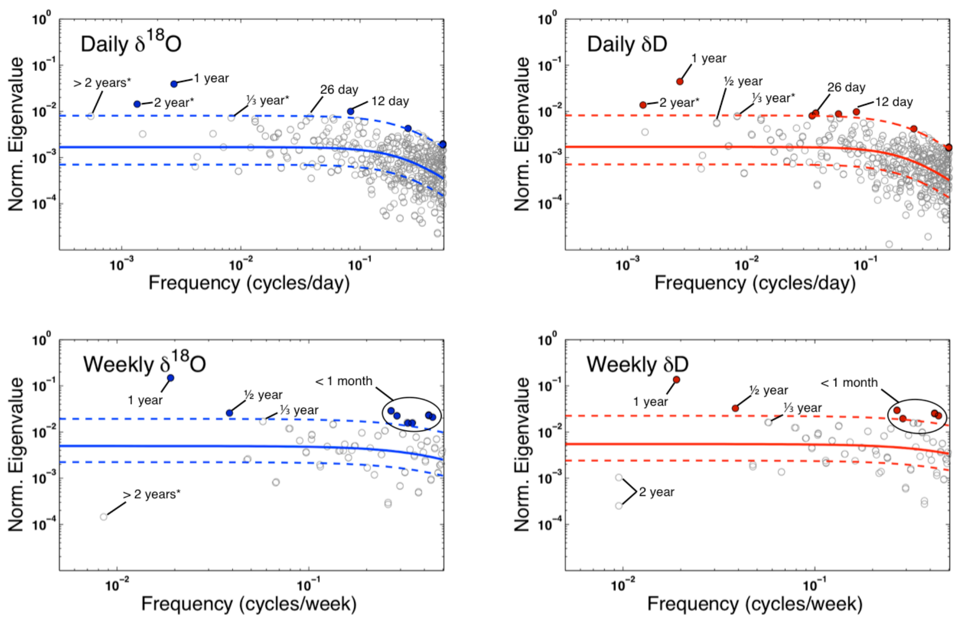

Figure 4-8: Eigenspectrum for daily and weekly amount weighted $\delta^{18}O$ (blue) and δD (red) time series of SSHCZO. Colored circles represent significant paired oscillatory or trend components. Eigenvalues labeled with star (*) correspond are single eigenvectors and not part of a pair. Solid line represents red noise spectrum and dashed lines correspond to 97.5 and 2.5% confidence bounds. The embedding dimension was 2 years for each time series (730 days or 104 weeks).

Major eigenvectors for SSHCZO show clear sinusoidal patterns (Figure 4-9). The annual eigenvectors were well resolved for both the daily and the weekly time series. The 2-year, 0.3-year, and 5-year eigenvectors for the daily time series did not have a matching pair. In other words, there was only one eigenvector used to describe each frequency. The 0.3-year cycle for the weekly time series appeared to have a strong sinusoidal signal but fell just below the confidence interval of the red noise spectrum (Figure 4-8). The 2.3-week cycle contained large amounts of amplitude modulation through its record, which potentially could play an important role during reconstruction.

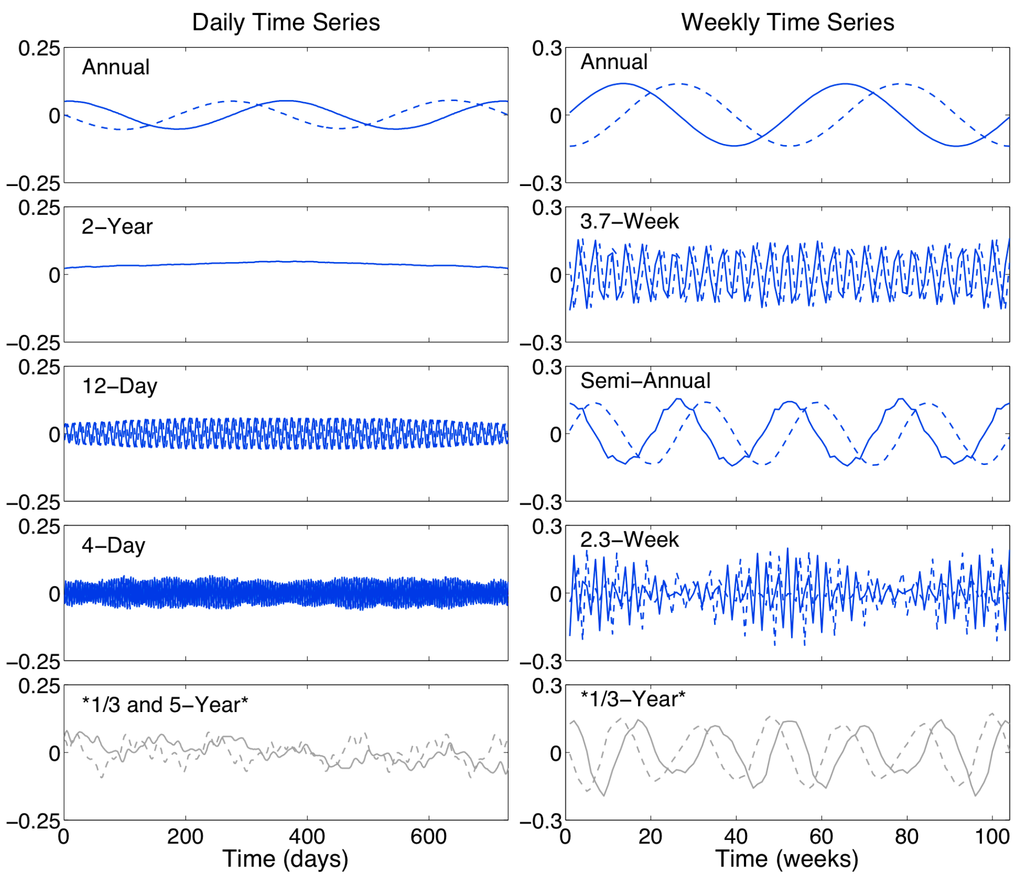

Figure 4-9: Major eigenvectors from SSA analysis of daily and weekly $\delta^{18}O$ time series for SSHCZO. Blue eigenvectors were considered statistically significant and fell above the red noise confidence bounds. Grey eigenvectors were not statistically significant but considered important to the time series.

4.5.3. 32-Year Reconstruction at SSHCZO

Reconstructions of the time series were created to understand the predictive power of major eigenvectors. The weekly time step was chosen for reconstruction as it balanced noise and signal, although other reconstruction time series could be developed. Because results of IsoGSM showed limited success when compared to SSHCZO, especially at the weekly time step, reconstructions were only developed for IsoRSM and SSHCZO (Figure 4-10). Reconstructions of IsoRSM for 32 years and SSHCZO for four years using important frequencies did an adequate job describing temporal patterns of isotopes in precipitation. Important frequencies were chosen based on significance and near-significance. For IsoRSM, the 10-year, 2.75-year, 1.75-year, 1-year, 0.8-year, and 0.5-year cycles were projected to reconstruct the weekly record. The eigenvectors were selected based on analysis of IsoGSM and SSHCZO eigenspectrum to determine which eigenvectors were important to describe the time series. With the reconstruction, the six pairs of eigenvectors accounted for 43.44% of the variability. Substantial variability was missed from the 32-year record due to short-term fluctuations around the seasonal cycle. Interannual variability was a strong component of the reconstructed time series.

For SSHCZO, the 2-year, 1-year, 0.5-year, 0.3-year, 3.7-week, and 2.3-week cycles were combined to reconstruct the 4-year record (Figure 4-10). The 2-year component did not have a matching eigenvector and constituted a trend within the record. Eigenvectors were selected following similar method as above. The SSHCZO reconstruction accounted for 51.87% of the variability within the record. Overall the reconstruction was more successful at describing short-term variability, an unsurprising fact, as high-frequency eigenvectors were used in the reconstruction.

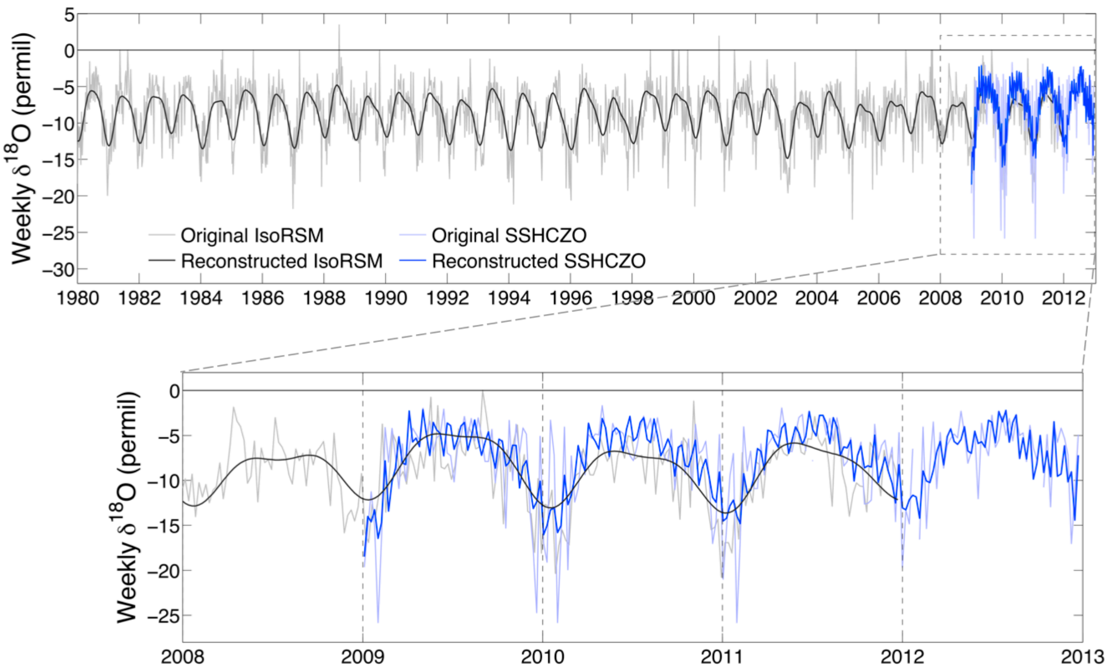

Figure 4-10: Reconstructions of weekly amount weighted $\delta^{18}O$ values for SSHCZO (blue) and IsoRSM (grey) using major eigenvectors (see text). Upper panel shows long-term reconstruction of IsoRSM in relation to SSHCZO time series. Lower panel shows agreement between SSHCZO and IsoRSM reconstructions. SSHCZO reconstruction accounts for 51.78% of the variability of the original time series while IsoRSM reconstruction accounts for 43.44% of the variability.

4.6. Summary & Conclusions

Comparisons of time series from two isotope-incorporated atmospheric general circulation models and observations from SSCZHO were performed to assess the efficiency of the models and their internal temporal structures. Linear regressions and Nash-Sutcliffe coefficients were calculated for daily, weekly, and monthly amount weighted $\delta^{18}O$ values of IsoGSM and IsoRSM versus SSHCZO. Additionally, the OIPC was compared against the SSHCZO as a baseline test. Singular spectrum analysis was also performed on daily, weekly, monthly amount weighted $\delta^{18}O$ and δD values for IsoGSM and IsoRSM. Due to record length limitations, SSA was performed on the daily and weekly amount weighted record of SSHCZO. Results provided the following conclusions:

1. Overall, models through all time series under predicted the isotopic range observed at SSHCZO. Time integration, moderately improved the predictive power of the models, yet could not completely describe the full isotopic range observed.
2. In general, IsoRSM at the monthly time step provided the best description of isotope values at SSHCZO and had a Nash-Sutcliffe coefficient of 0.5792.
3. Eigenspectrum for IsoGSM, IsoRSM, and SSHCZO at each time interval showed significant eigenvalues at the annual cycle and its harmonics.
4. Time integration reduced the number of eigenvalues considered significant, suggesting time averaging performs a type of windowing on the eigenspectrum.
5. Reconstructions of IsoRSM and SSHCZO are capable of explaining approximately half of the original time series, suggesting large portion of the time series is inherent variability.
6. The specific IsoRSM and SSHCZO reconstruction contained different amounts of resolution, affecting the applicability of reconstructions.

Although substantial progress has been made comparing IsoGSM and IsoRSM to SSHCZO observations, there remain unanswered questions. First, additional sampling and measurements of isotopes in precipitation at SSHCZO is required to determine long term variability and low frequency oscillations in precipitation isotopes. A record length of 5+ years would increase the resolution of long-term fluctuations. Second, intercomparisons must be preformed at other spatial locations to fully understand the efficiency of IsoGSM and IsoRSM to predict the space-time dependency of precipitation isotopic compositions. Finally, with the results of this work, improvements to the general circulation models can be performed to more successfully describe isotopes in precipitation at SSHCZO and other locations.

Chapter 5.

Conclusions and Future Work

5.1. Summary of Completed Work

Building of previous work at SSHCZO, numerous findings were described in Chapter 2 regarding spatiotemporal patterns of soil water isotopes within the catchment. Most dramatically, soil water isotopes were found to vary seasonally similar to precipitation especially in the shallow layers. Soil water isotope profiles showed strong attenuation of this seasonal variation of isotopic compositions with depth, suggesting the importance of hydrodynamic mixing of precipitation from multiple seasons. Additionally, isotopic composition profiles provided unique insight to preferential flow patterns and snow melt dynamics. Large increases in standard deviations along soil horizon and soil-bedrock interfaces during the winter months suggested lateral preferential flow occurred regularly within the catchment. Relatively smooth isotopic composition profiles through the first meter, during the summer months, suggested little lateral preferential flow, and occurrences of vertical preferential flow bypassing the upper soil layers. Comparison of north and south slopes showed variable snowmelt dynamics in the catchment, with snow more readily melting and infiltrating the upper soil layers on the north slope, and snow sublimating and enriching on the south slope prior to infiltration. Finally, investigation of summer soil water isotope compositions showed little evaporation trends suggesting the mobile domain of the soil profile does not experience substantial evaporation. This finding must be taken carefully as a major limitation of the study is the inability of the suction cup lysimeters to fully sample the soil matrix, leaving behind tightly held water.

A more detailed analysis of the isotopic composition of precipitation at SSHCZO (Chapter 3) led to a better understanding of the isotopic input to the catchment. Using event based precipitation data from 2009-2012, univariate and bivariate kernel density estimates were constructed to understand the probability density distributions, and results showed precipitation compositions were skewed towards more depleted values. Unweighted and precipitation amount weighted kernel density estimates were also constructed to understand the influence of precipitation amount on distributions. Inclusion of precipitation amounts to KDEs decreased the peak densities and shifted the distributions slightly towards more depleted values. Time integration to daily, weekly, monthly, and seasonally amount weighted time series reduced the variability within the record yet preserved the seasonal variability, with more depleted values in the cold season and less depleted values in the warm season. Snow in the cold months and tropical storms in the early fall appeared to control this seasonal variability. Construction of the local meteoric water line using event, daily, weekly, monthly, and seasonally amount weighted time series demonstrated the variability in slope and intercept. Closer investigation showed the local meteoric water line defined using high-resolution sampling contained a bias due to low d-excess and low amount events. The local meteoric water line defined using precipitation amount weighted least squares regression provided the most valuable local meteoric water line for future hydrological investigations.

The first step in development of a spatially and temporally distributed data layer for isotope compositions in precipitation was carried out through the time series analysis of isotope incorporated atmospheric general circulation models and SSHCZO (Chapter 4). Specifically, regressions of daily, weekly, and monthly amount weighted time series were performed on a global spectrum model and its downscaled regional spectrum model to compare how each model performed versus the observations at SSHCZO. Overall, each model underpredicted the isotopic range observed at SSHCZO. IsoRSM was found to be the best performing model based on a Nash-Sutcliffe coefficient of 0.5792. Singular spectrum analysis was preformed on each amount weighted time series to determine the temporal structure of each record and showed the importance of the annual cycle and its harmonics. Time integration reduced the number of eigenvalues considered significant suggesting time integration performs a type of windowing on the eigenspectrum. Reconstructions of the weekly amount weighted IsoRSM and SSHCZO records accounted for approximately 50% of the variability, suggesting both records contain substantial innate noise.

5.2. Potential Future Work

5.2.1. Continued Isotope Hydrology Studies at SSHCZO

Detailed investigations of spatiotemporal patterns of soil water and precipitation isotope compositions have furthered the understanding of hydrologic process at SSHCZO, yet there remains unfinished work to more fully appreciate processes such as tree source water dynamics, the role of immobile soil water, deep groundwater storage and flows, and long term trends in precipitation isotope compositions. Ongoing work is attempting to synthesize isotope hydrology with previous conceptual hydrologic models of SSHCZO to understand how various hydrologic pools interact at different periods of time. Further, knowledge gained through these isotope hydrology studies will be used in conjunction with other water chemistry data to understand flow paths, hydrologic timescales, and deep groundwater dynamics.

5.2.2. Spatial Validation of Results from Downscaled Atmospheric GCM

Based on the relatively promising results of the comparison between IsoRSM and SSHCZO, a fully distributed data product with isotopes in precipitation for the Chesapeake Bay watershed has been developed, yet remains unverified at other spatial locations. As a raw data product, the data layer adequately predicts isotopic composition of precipitation at 10 km resolution and hourly time steps. Further work is required to more robustly understand the temporal variability of the modeled isotopic compositions. One procedure, which would be beneficial for this understanding, would be a detailed analysis of one or more major meteorological events at a specific location. This would provide insight to the accuracy of modeled precipitation isotopic compositions during important hydrologic events. Detailed investigation of a typical event would also shed light on the processes, which contribute to the long-term hydrological state of a watershed.

Cross comparison of IsoRSM at other locations in the Chesapeake Bay watershed would further validate its predicted isotopic composition of precipitation. Observations from sites in the IAEA's Global Network of Isotopes in Precipitation (GNIP) or the National Atmospheric Deposition Program (NADP) are an ideal candidate for further validation. Typically these sites have multi-year records of weekly or monthly bulk precipitation samples, which could be used following the linear regression or singular spectrum procedures outlined in Chapter 4. Results would then determine if IsoRSM provides a better estimate of isotopes in precipitation than the Online Isotopes in Precipitation Calculator, the current standard for estimating isotopes in precipitation for ungagged basins.

5.2.3. Distributed Isotopic Age Modeling of Chesapeake Bay watershed

A promising application of the IsoRSM derived data product is the distributed isotopic age modeling of waters in the Chesapeake Bay watershed using the Penn State Integrated Hydrologic Model (PIHM). Building off the work of Bhatt (2012), it is now possible to model the isotopic age dynamics through space and time over large regions using realistic isotopic forcing. Findings from distributed age modeling potentially could inform managers, policy makers, and the public of hydrologic process timescales, which often can be difficult to determine or conceptualize. Before application of the IsoRSM derived data product, it would be important to validate the spatiotemporal dynamics of precipitation isotopic compositions as well as develop a strategy for implementation. One major challenge is the know errors associated with GCM modeled precipitation amounts. A robust data management technique must be developed to successfully and accurately apply the data product to a large-scale hydrologic model.

REFERENCES CITED

Anderson, S.P., R.C. Bales, and C.J. Duffy. 2008. Critical Zone Observatories: Building a network to advance interdisciplinary study of Earth surface processes. Mineralogical Magazine 72(1): 7–10.

Anderson, S.P., F. von Blanckenburg, and a. F. White. 2007. Physical and Chemical Controls on the Critical Zone. Elements 3(5): 315–319.

Andrews, D.M., H. Lin, Q. Zhu, L. Jin, and S.L. Brantley. 2011. Hot Spots and Hot Moments of Dissolved Organic Carbon Export and Soil Organic Carbon Storage in the Shale Hills Catchment. Vadose Zone Journal 10(3): 943–954.

Araguás-Araguás, L., K. Froehlich, and K. Rozanski. 2000. Deuterium and oxygen-18 isotope composition of precipitation and atmospheric moisture. Hydrological Processes 14(8): 1341–1355.

Argiriou, A. a., and S. Lykoudis. 2006. Isotopic composition of precipitation in Greece. Journal of Hydrology 327(3-4): 486–495.

Barnes, C.J., and G.B. Allison. 1983. The distribution of deuterium and 18 O in dry soils: 1. Theory. Journal of Hydrology 60: 141–156.

Barnes, C., and G. Allison. 1988. Tracing of water movement in the unsaturated zone using stable isotopes of hydrogen and oxygen. Journal of Hydrology 100: 143–176.

Bhatt, G. 2012. A Distributed Hydrologic Modeling System: Framework for Discovery and Management of Water Resources. PhD Dissertation, The Pennsylvania State University.

Bowen, G.J., and J. Revenaugh. 2003. Interpolating the isotopic composition of modern meteoric precipitation. Water Resources Research 39(10): 1299.

Bowen, G.J., L.I. Wassenaar, and K. a Hobson. 2005. Global application of stable hydrogen and oxygen isotopes to wildlife forensics. Oecologia 143(3): 337–48.

Bowen, G., and B. Wilkinson. 2002. Spatial distribution of δ18O in meteoric precipitation. Geology 30(4): 315–318.

Brantley, S., M. Goldhaber, and K. Ragnarsdottir. 2007. Crossing Disciplines and Scales to Understand the Critical Zone. Elements 3: 307–314.

Brooks, R.J., H.R. Barnard, R. Coulombe, and J.J. McDonnell. 2009. Ecohydrologic separation of water between trees and streams in a Mediterranean climate. Nature Geoscience 3(2): 100–104.

Broomhead, D.S., and G.P. King. 1986. On the qualitative analysis of experimental dynamical systems. Nonlinear Phenomena and Chaos: 113–144.

Burton, W.C., L.N. Plummer, E. Busenberg, B.D. Lindsey, and W.J. Gburek. 2002. Influence of fracture anisotropy on ground water ages and chemistry, Valley and Ridge Province, Pennsylvania. Ground Water 40(3): 242–257.

Caplan, P., J. Derber, W. Gemmill, S.-Y. Hong, H.-L. Pan, and D. Parrish. 1997. Changes to the 1995 NCEP Operational Medium-Range Forecast Model Analysis–Forecast System. Weather and Forecasting 12(3): 581–594.

Clark, I., and P. Fritz. 1997. Environmental Isotopes in Hydrogeology. Lewis Publishers, Boca Raton, Florida.

Craig, H. 1961a. Standard for Reporting Concentrations of Deuterium and Oxygen-18 in Natural Waters. Science 133(3467): 1833–1834.

Craig, H. 1961b. Isotopic Variations in Meteoric Waters. Science (New York, N.Y.) 133(2465): 1702–1703.

Criss, R.E., and M.L. Davisson. 1996. Isotopic imaging of surface water/groundwater interactions, Sacramento Valley, California. Journal of Hydrology 178(1-4): 205–222.

Dansgaard, W. 1954. The O18-Abundance in Fresh Water. Geochimica et Cosmochimica Acta 6: 241–260.

Dansgaard, W. 1964. Stable isotopes in precipitation. Tellus 16(4): 436–468.

Darling, W.G., and a. H. Bath. 1988. A stable isotope study of recharge processes in the English Chalk. Journal of Hydrology 101(1-4): 31–46.

Davisson, M.., and R. Criss. 1993. Stable isotope imaging of a dynamic groundwater system in the southwestern Sacramento Valley, California, USA. Journal of Hydrology 144: 213–246.

Dawson, T., and J. Ehleringer. 1991. Streamside trees that do not use stream water. Nature 350(6316): 335–337.

Duffy, C. 1996. A two-state integral-balance model for soil moisture and groundwater dynamics in complex terrain. Water Resources Research 32(8): 2421–2434.

Ehleringer, J.R., and T.E. Dawson. 1992. Water uptake by plants: perspectives from stable isotope composition. Plant, Cell and Environment 15(9): 1073–1082.

Eichinger, L., B. Merkel, G. Nemeth, J. Salvamoser, and W. Stichler. 1984. Seepage and velocity determinations in unsaturated quaternary gravel. p. 303–313. *In* Recent investigations in the Zone of Areation. Munich, West-Germany.

Elsner, J.B., and A.A. Tsonis. 1996. Singular Spectrum Analysis: A New Tool in Time Series Analysis. Plenum Publishig Corporation, New York and London.

Epstein, S., and T. Mayeda. 1953. Variation of O 18 content of waters from natural sources. Geochimica et cosmochimica acta 4: 213–224.

Figueroa-Johnson, M. a., J. a. Tindall, and M. Friedel. 2007. A Comparison of 18Oδ Composition of Water Extracted from Suction Lysimeters, Centrifugation, and Azeotropic Distillation. Water, Air, and Soil Pollution 184(1-4): 63–75.

Freedman, D., and P. Diaconis. 1981. On the histogram as a density estimator: L2 theory. Zeitschrift f�r Wahrscheinlichkeitstheorie und Verwandte Gebiete 57(4): 453–476.

Friedman, I. 1953. Deuterium content of natural waters and other substances. Geochimica et Cosmochimica Acta 4(1-2): 89–103.

Fritz, P., R.J. Drimme, S.K. Frape, and K. O'Shea. 1987. The Isotopic Composition of Precipitation and Groundwater in Canada. p. 815. *In* Isotope Techniques in Water Resources Development. International Atomic Energy Agency, Vienna.

Gat, J.R. 1971. Comments on the Stable Isotope Method in Regional Groundwater Investigations. Water Resources Research 7(4): 980–993.

Gat, J.R. 1996. Oxygen and Hydrogen Isotopes in the Hydrologic Cycle. Annual Review of Earth and Planetary Sciences 24(1): 225–262.

Gat, J.R., and R. Gonfiantini. 1981. Atmospheric waters. p. 103–142. *In* Stable Isotope Hydrology: Deuterium and Oxygen in the Water Cycle. Technical Report Series No. 210. International Atomic Energy Agency, Vienna.

Gazis, C., and X. Feng. 2004. A stable isotope study of soil water: evidence for mixing and preferential flow paths. Geoderma 119(1-2): 97–111.

Geake, A., and S. Foster. 1989. Sequential isotope and solute profiling in the unsaturated zone of British Chalk. Hydrological Sciences Journal 34(1): 79–96.

Gierke, C. 2012. Sourcing Tree Water in the Sacramento Mountains of New Mexico: A Stable Isotope Study. MS Thesis, New Mexico Institute of Mining and Technology.

Golyandina, N., V. Nekrutkin, and A. Zhigljavsky. 2001. Analysis of Time Series Structure: SSA and Related Techniques. Chapman & Hall/CRC.

Graham, C.B., and H.S. Lin. 2011. Controls and Frequency of Preferential Flow Occurrence: A 175-Event Analysis. Vadose Zone Journal 10(3): 816.

Hintze, J., and R. Nelson. 1998. Violin plots: a box plot-density trace synergism. The American Statistician 52(2): 37–41.

Holmes, G.H. 2011. Using δ2H and δ18O to Determine the Flowpath and Timescales of Water at the Susquehanna Shale Hills Critical Zone Observatory. MS Thesis, The Pennsylvania State University.

Hughes, C.E., and J. Crawford. 2012. A new precipitation weighted method for determining the meteoric water line for hydrological applications demonstrated using Australian and global GNIP data. Journal of Hydrology 464-465: 344–351.

IAEA. 1992. Statistical treatment of data on environmental isotopes in precipitation. Technical. International Atomic Energy Agency, Vienna.

International Atomic Engery Agency. 2009. Reference Sheet for International Measurement Standards. Vienna.

Jin, L., D.M. Andrews, G.H. Holmes, H. Lin, and S.L. Brantley. 2011. Opening the "Black Box": Water Chemistry Reveals Hydrological Controls on Weathering in the Susquehanna Shale Hills Critical Zone Observatory. Vadose Zone Journal 10(3): 928–942.

Jin, L., and S.L. Brantley. 2011. Soil chemistry and shale weathering on a hillslope influenced by convergent hydrologic flow regime at the Susquehanna/Shale Hills Critical Zone Observatory. Applied Geochemistry 26: S51–S56.

Jin, L., R. Ravella, B. Ketchum, P.R. Bierman, P. Heaney, T. White, and S.L. Brantley. 2010. Mineral weathering and elemental transport during hillslope evolution at the Susquehanna/Shale Hills Critical Zone Observatory. Geochimica et Cosmochimica Acta 74(13): 3669–3691.

Kanamaru, H., and M. Kanamitsu. 2007. Scale-Selective Bias Correction in a Downscaling of Global Analysis Using a Regional Model. Monthly Weather Review 135(2): 334–350.

Kirchner, J.W. 2003. A double paradox in catchment hydrology and geochemistry. Hydrological Processes 17(4): 871–874.

Kuntz, B.W., S. Rubin, B. Berkowitz, and K. Singha. 2011. Quantifying Solute Transport at the Shale Hills Critical Zone Observatory. Vadose Zone Journal 10(3): 843–857.

Landon, M.., G.. Delin, S.. Komor, and C.. Regan. 1999. Comparison of the stable-isotopic composition of soil water collected from suction lysimeters, wick samplers, and cores in a sandy unsaturated zone. Journal of Hydrology 224(1-2): 45–54.

Leaney, F., K. Smettem, and D. Chittleborough. 1993. Estimating the contribution of preferential flow to subsurface runoff from a hillslope using deuterium and chloride. Journal of Hydrology 147: 83–103.

Lee, K.-S., J.-M. Kim, D.-R. Lee, Y. Kim, and D. Lee. 2007. Analysis of water movement through an unsaturated soil zone in Jeju Island, Korea using stable oxygen and hydrogen isotopes. Journal of Hydrology 345(3-4): 199–211.

Leibundgut, C., P. Maloszewski, and C. Külls. 2009. Environmental Tracers. p. 13–56. *In* Tracers in Hydrology. John Wiley & Sons, Ltd.

Lin, H. 2006. Temporal Stability of Soil Moisture Spatial Pattern and Subsurface Preferential Flow Pathways in the Shale Hills Catchment. Vadose Zone Journal 5(1): 317–340.

Lin, H., J. Bouma, Y. Pachepsky, A. Western, J. Thompson, R. van Genuchten, H.-J. Vogel, and A. Lilly. 2006a. Hydropedology: Synergistic integration of pedology and hydrology. Water Resources Research 42(5): n/a–n/a.

Lin, H.S., W. Kogelmann, C. Walker, and M. a. Bruns. 2006b. Soil moisture patterns in a forested catchment: A hydropedological perspective. Geoderma 131(3-4): 345–368.

Lin, H., and X. Zhou. 2008. Evidence of subsurface preferential flow using soil hydrologic monitoring in the Shale Hills catchment. European Journal of Soil Science 59(1): 34–49.

Lis, G., L.I. Wassenaar, and M.J. Hendry. 2008. High-precision laser spectroscopy D/H and 18O/16O measurements of microliter natural water samples. Analytical chemistry 80(1): 287–293.

Lynch, J. 1976. Effects of antecedent soil moisture on storm hydrographs. PhD Dissertation, The Pennsylvania State University.

McDonnell, J.J. 1990. A Rationale for Old Water Discharge Through Macropores in a Steep, Humid Catchment. Water Resources Research 26(11): 2821–2832.

McDonnell, J.J., M. Sivapalan, K. Vaché, S. Dunn, G. Grant, R. Haggerty, C. Hinz, R. Hooper, J. Kirchner, M.L. Roderick, J. Selker, and M. Weiler. 2007. Moving beyond heterogeneity and process complexity: A new vision for watershed hydrology. Water Resources Research 43(7): 1–6.

Nash, J., and J. Sutcliffe. 1970. River flow forecasting through conceptual models part I—A discussion of principles. Journal of hydrology 10: 282–290.

National Oceanographic and Atmospheric Administration. 2007. U.S. divisional and station climatic data and normals: Asheville, North Carolina, U.S. Department of Commerce, National Oceanic and Atmospheric Administration, National Environmental Satellite Data and Information Service, National Climatic Data Center. Available at http://www7.ncdc.noaa.gov/CDO/cdo.

National Research Council. 2001. Basic Research Opportunities in Earth Science. National Academy Press, Washington, DC.

Newman, B., A. Tanweer, and T. Kurttas. 2008. IAEA Standard Operating Procedure for the DT-100 Liquid-Water Isotope Analyser. : 26.

Nutter, W.L. 1964. Determination of the Head-Discharge Relationship for a Sharp-crested Compound Weir and a Sharp-crested Parabolic Weir. MS Thesis, The Pennsylvania State University.

O'Driscoll, M. a., D.R. DeWalle, K.J. McGuire, and W.J. Gburek. 2005. Seasonal 18O variations and groundwater recharge for three landscape types in central Pennsylvania, USA. Journal of Hydrology 303(1-4): 108–124.

Pearce, A., M. Stewart, and M. Sklash. 1986. Storm Runoff Generation in Humid Headwater Catchments 1. Where Does the Water Come From? Water Resources Research 22(8): 1263–1272.

Phillips, F.M. 1995. The use of isotopes and environmental tracers in subsurface hydrology. Reviews of Geophysics Supplement(95): 1029–1033.

Qu, Y., and C.J. Duffy. 2007. A semidiscrete finite volume formulation for multiprocess watershed simulation. Water Resources Research 43(8): W08419.

Reich, E.G. 1966. A Rain Study of a Small Drainage Basin in Central Pennsylvania. MS Thesis, The Pennsylvania State University.

Rice, K.C., and G.M. Hornberger. 1998. Comparison of hydrochemical tracers to estimate source contributions to peak flow in a small, forested, headwater catchment. Water Resources Research 34(7): 1755–1766.

Rozanski, K., L. Araguás-Araguás, and R. Gonfiantini. 1993. Isotopic patterns in modern global precipitation. p. 1–36. *In* Swart, P.K., Lohmann, K.C., McKenzie, J., Savin, S. (eds.), Geophysical Monograph 78: Climate Change in Continental Isotope Records. American Geophysical Union, Washington, DC.

Silverman, B.W. 1986. Density Estimation for Statistics and Data Analysis. Chapman and Hall, New York, London.

Sklash, M.G., and R.N. Farvolden. 1979. The Role of Groundwater in Storm Runoff. Journal of Hydrology 43: 45–65.

Sklash, M.G., R.N. Farvolden, and P. Fritz. 1976. A conceptual model of watershed response to rainfall, developed through the use of oxygen-18 as a natural tracer. Canadian Journal of Earth Sciences 13: 271–283.

Susquehanna Shale Hills Critical Zone Observatory. Available at http://criticalzone.org/shale-hills.

Tang, K., and X. Feng. 2001. The Effect of Soil Hydrology on the Oxygen and Hydrogen Isotopic Compositions of Plants' Source Water. Earth and Planetary Science Letters 185: 355–367.

Vanclooster, M., M. Javaux, and J. Vanderborght. 2005. Solute Transport in Soil at the Core and Field Scale. Encyclopedia of Hydrological Sciences: 1–13.

Vautard, R., P. Yiou, and M. Ghil. 1992. Singular-spectrum analysis: A toolkit for short, noisy chaotic signals. Physica D: Nonlinear Phenomena 58: 95–126.

Vogel, T., M. Sanda, J. Dusek, M. Dohnal, and J. Votrubova. 2010. Using Oxygen-18 to Study the Role of Preferential Flow in the Formation of Hillslope Runoff. Vadose Zone Journal 9(2): 252–259.

Volk, W. 1958. Applied Statistics for Engineers. McGraw-Hill Book Company, Inc, New York.

Waliser, D., and C. Gautier. 1993. A Satellite-derived Climatology of the ITCZ. Journal of Climate 6: 2162–2174.

White, A.F., M.S. Schulz, D. V. Vivit, A.E. Blum, D. a. Stonestrom, and J.W. Harden. 2005. Chemical weathering rates of a soil chronosequence on granitic alluvium: III. Hydrochemical evolution and contemporary solute fluxes and rates. Geochimica et Cosmochimica Acta 69(8): 1975–1996.

Wilding, L.P., and H. Lin. 2006. Advancing the frontiers of soil science towards a geoscience. Geoderma 131(3-4): 257–274.

Winograd, I.J., A.C. Riggs, and T.B. Coplen. 1998. The relative contributions of summer and cool-season precipitation to groundwater recharge, Spring Mountains, Nevada, USA. Hydrogeology Journal 6(1): 77–93.

Yoshimura, K., and M. Kanamitsu. 2008. Dynamical Global Downscaling of Global Reanalysis. Monthly Weather Review 136(8): 2983–2998.

Yoshimura, K., M. Kanamitsu, D. Noone, and T. Oki. 2008. Historical isotope simulation using Reanalysis atmospheric data. Journal of Geophysical Research 113(D19): 1–15.

Zimmermann, U., D. Ehhalt, and K. Münnich. 1968. Soil-Water Movement and Evapotranspiration: Changes in the Isotopic Composition of the Water. p. 567–584. *In* Isotopes in Hydrology. International Atomic Energy Agency, Vienna, Vienna.

Appendix A

Data Management: Comparison between LPM and Ott Instruments

1. Motivation

The SSHCZO is a highly instrument experimental catchment interested in a large variety of environmental processes. Many of these environmental investigations utilized observed precipitation values to understand processes such as storm flow generation, soil moisture dynamics, or chemical weathering rates. Even though the catchment is relatively small and does not contain any large elevation gradients, it is still beneficial to monitor precipitation using a variety of techniques. In this study, an Ott Pluvio weighing bucket was compared against a Laser Precipitation Monitor (LPM) to establish if any significant differences exist and if so which instrument should be utilized for further investigations. Deciphering which instrument better observes the precipitating amounts is a challenging task as precipitation measurements are inherently stochastic. It is well known that precipitation measurements are influenced by a variety of factors including wind, precipitation type, air temperature, and vegetation cover. Both the Ott and the LPM have advantages over the other with respect to measurement errors. It should also be noted that multiple instruments are advantageous because of redundancy and that in the event of single instrument failure, the second instrument is capable of recording the environmental variable of interest.

2. Methods

2.1 Instruments

Both the Ott Pluvio (hereafter Ott) and LPM were installed in a ridge top clearing at the SSHCZO in central Pennsylvania. The clearing measured approximately 10 m in diameter and was vegetated by short to tall grasses during the growing season. The clearing was bordered by deciduous and coniferous trees, which drastically reduced the wind speeds to 0-10 m/s throughout the entire year. The Ott was installed in 2006 in the center of the clearing on a level concrete pad while the LPM as installed in 2009 at a height of 2 m and approximately 2 m horizontally from the Ott. Neither instrument was significantly affected by throughfall based on these installations. Because snow packs remained relatively low (<0.5 m) during the observation period, winter precipitation observations are considered to be accurate measurements.

The Ott gage works by continually weighing the volume of water collected within the stainless steel bucket. Incremental changes within the bucket are measured by an electronic weighting cell and record as an amount of precipitation every ten minutes. Precipitation intensities are also determined for each ten-minute increment. Stainless steel fans are installed around the perimeter of the Ott to reduce the affects of strong winds on the collection efficiency.

Raw data from the Ott instrument is streamed live to the SSHCZO website (http://criticalzone.org/shale-hills). Lags between data collection in the field and uploading to SSHCZO website occur occasionally due to network lags and power outages. After outage, data is typically restored online. Streaming raw data is considered Level 0 according to National CZO guidelines. This means data is not checked for gaps, errors, or processed. Analysis of precipitation was performed on the raw ten-minute precipitation amounts only.

The Laser Precipitation Monitor (LPM) records precipitation amounts, intensities, size, and type using a beam of lasers. As precipitation droplets fall through the LPMs sensors the instrument determines the type of precipitation using the ambient temperature, size of precipitation droplet, and droplet velocity. Precipitation measurements are reported similarly as the Ott instrument.

2.2 Data manipulation to compare similar measurements

Raw data from the LPM and Ott was adjusted to allow for equal comparisons. Raw time stamps and precipitation amounts were run through Matlab file, which adjusted the records so comparisons could be made for various time integration periods. Before comparison could be preformed, full-length time series were constructed from using the first and last observations. The time step for the full time series was ten-minutes. The ten-minute LPM data was constructed from the daily record. Values for a given time step were found by finding the difference between the given time step and the time step prior, unless the time step fell at the first measurement of a given day. This procedure was not carried out for the Ott measurements, as they were reported as amounts per ten-minutes.

Clear erroneous observations were removed before analysis. The threshold for this value was subjective and chosen as measurements >75mm during a given ten-minute sampling. Values above the threshold were replaced with NaN (not a number) values in Matlab. Gaps were filled with NaN values. Measurements made by one instrument while the other instrument did not record were not considered in the regressions below.

2.3 Comparison over different integration periods

Comparison of LPM and Ott was performed for four distinct integration periods, ten-minute, hourly, six-hour, and 24-hour to account for short collection and small amount variability. Investigation of sample collection amounts over a range of time periods allows for determination of biases either due to short or long collection periods. Further, integrating over longer periods is assumed to average micro-climatic variations with respect to each instruments location. For instance, slight variations in wind speed or wind directions, which would cause differences, in short term measurements, would be averaged out over longer integration periods. Additionally, comparisons over four periods allow for detailed understanding of process timescales and provides us with regressions based on each integration period.

The ten-minute integration period is the smallest value, which could be compared. This is considered pseudo-raw data as the LPM data had to be manipulated in order to compare against the raw Ott data. Hourly samples were calculated by summing the six measurements made during a given hour. If any of the six observations were missing during the hour period, the value was considered NaN. Six hour and 24-hour values were handled similar to hourly values.

2.4 Handling Outliers

To determine linear regressions for each time interval computation were only performed on high-quality data. Determination of high-quality data was a somewhat subjective process and consisted of two parts: comparison of measurements >0 mm and removal of outliers. Since both the LPM and Ott were co-located in the ridge top clearing of SSHCZO, it was expected that both instruments would report the same precipitation amounts for each measurement period resulting in a one-to-one regression of the two instruments. To account for periods of poor quality measurements, regardless of reason, time steps where either instrument recorded 0 mm of precipitation were removed from analysis. Additionally a subjective procedure for outlier selection was determined by finding the absolute difference between the LPM and Ott measurements during a given time step. Absolute differences were 10 mm, 15 mm, 15 mm, and 50 mm for ten minute, hourly, six hour, and 24-hour integration periods respectively.

Table A-1: Summary of Ott and LPM comparison.

		Integration Period			
		10-Minute	**1-Hour**	**6-Hour**	**24-Hour**
Number of LPM Measurements		158,677	26,424	4,404	1,101
Number of Ott Measurements		147,206	26,424	4,404	1,101
Full Record	**Slope**	0.6052	0.7868	0.8591	0.8070
	Intercept	0.1607	0.2664	0.3966	0.9538
	R^2	0.7974	0.9532	0.9479	0.9167
Number of Outliers		5	3	4	3
Number of Zeros		140,162	24,390	3,706	728
Outliers Removed	**Slope**	0.7022	0.8768	0.9552	0.9260
	Intercept	0.1267	0.1572	0.1157	0.1891
	R^2	0.8186	0.9651	0.9810	0.9716
Log-Log Regression	**Slope**	0.5848	0.8506	0.9209	0.8959
	Intercept	-0.4350	-0.0308	-0.0102	0.0321

3. Results and Discussion

Time series of each integration period (10-minute, 1-hour, 6-hour, 24-hour) showed general agreement between the two instruments. While difficult to determine, both instruments captured the high intensity events in the 10-minute record and captured the relatively uniform precipitation amounts associated with the 24-hour time series. Major gaps were discovered in the Ott instrument during the summer and fall of 2010 as well as the winter of 2011. The cause of this erroneous data is unclear, as the instrument was reporting zero precipitation during the entire period. Clearly this data is faulty, as was thrown out for the later regressions.

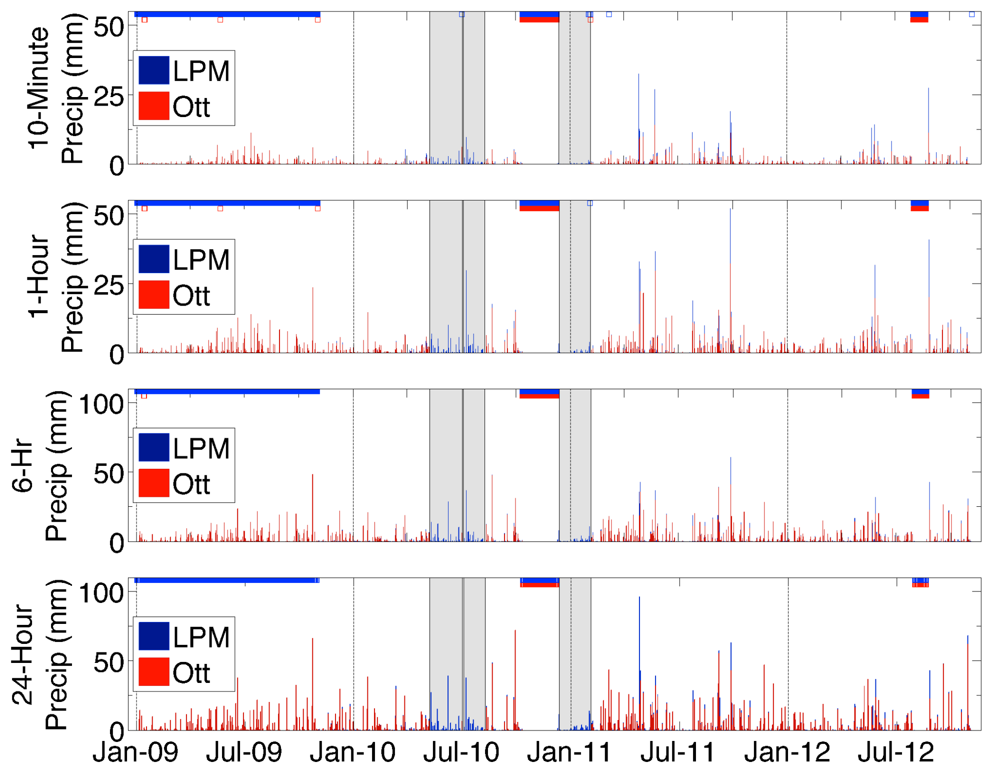

Appendix Figure 1: Time series of Ott and LPM instruments for 10-minute, 1-hour, 6-hour, and 24-hour precipitation totals. Colored bars at the top of each panel correspond to gaps within the record. Grey region of each panel corresponds to known errors in Ott record.

Regressions were performed using observations for time steps where both instruments record precipitation greater than zero. Each instrument had relatively similar precipitation amounts for each time interval. The best agreement occurred for the 1-hour, 6-hour, and 24-hour intervals. Over each time interval there appears to be a slight bias between the instruments where the LPM typically predicts larger precipitation amounts when compared to the Ott. Even with removal of the outliers, the bias appears to remain. Integration to 6-hour and 24-hour reduced the magnitude of the bias but could not remove it completely.

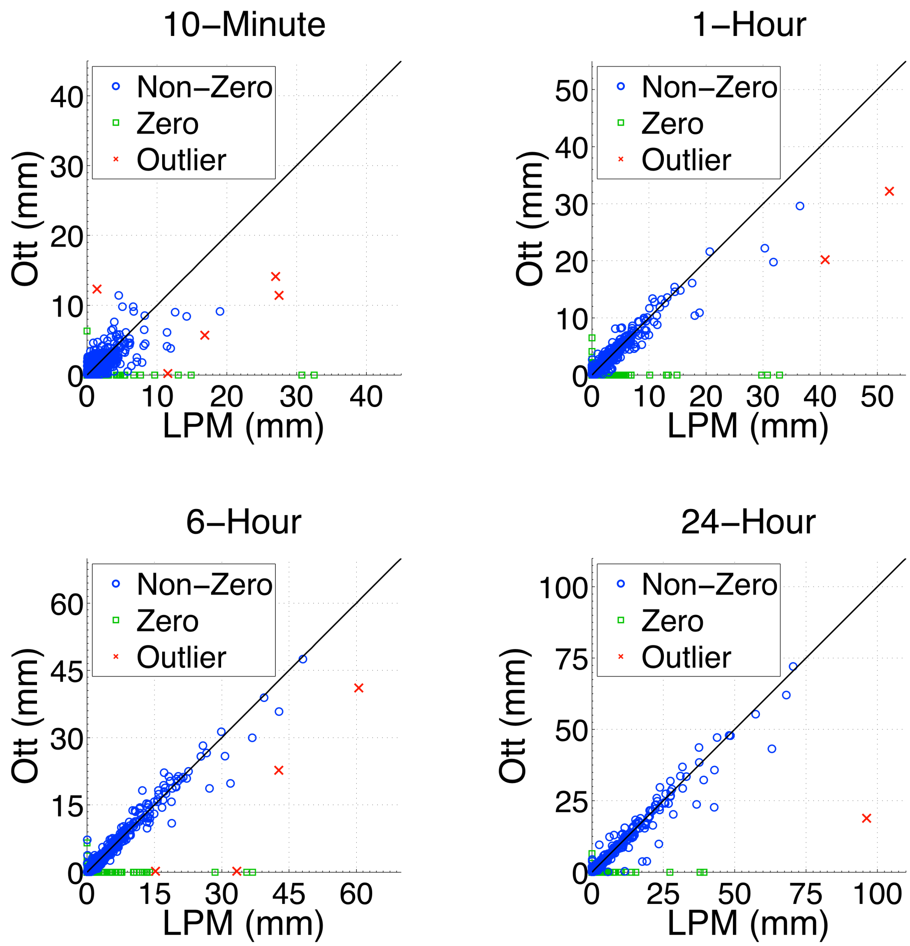

Appendix Figure 2: Linear regressions of Ott and LPM instruments for 10-minute, 1-hour, 6-hour and 24-hour integration periods. The black line is the one-to-one line.

Log-log regressions better display the comparison of low precipitation amounts for both the Ott and the LPM. It is clear from this comparison that as precipitation amounts get smaller the agreement between the two instruments decreases. This is mostly due to the differing resolution of the two instruments. Because the Ott only measures precipitation amounts to 0.1 mm and the LPM measures precipitation amounts to the 0.01 mm, the correlation between the two decreases. In hydrological applications this typically is not as important since these small events do not dominate the hydrologic response of the catchment.

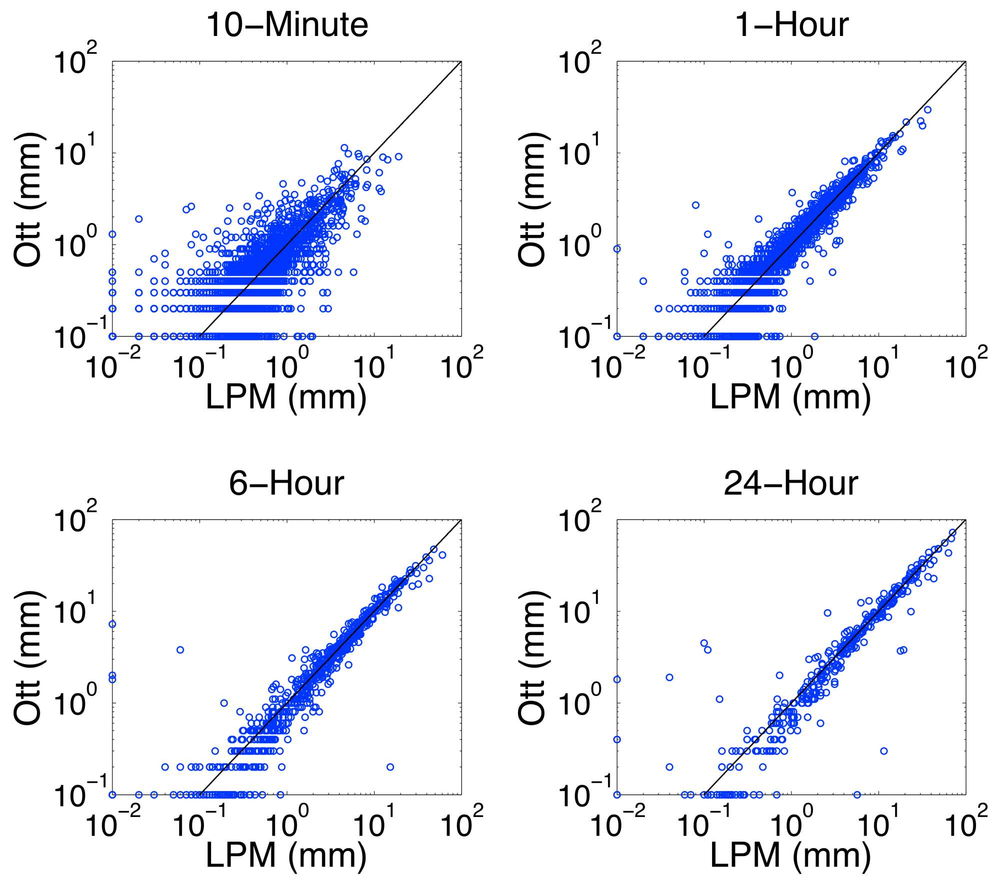

Appendix Figure 3: Log-log plots of Ott versus LPM for 10-minute, 1-hour, 6-hour, and 24-hour precipitation totals. Black line represents the one to one line.

4. Conclusion

Based on the comparison of 10-minute, 1-hour, 6-hour, and 24-hour precipitation amounts from the Ott and the LPM instruments at SSHCZO, the optimal record to use is the Ott. The Ott record provided relatively conservative estimates of precipitation amounts for the catchment. Gaps in the Ott record should be filled using the appropriate LPM regression.

Appendix B

Data Management: SSHCZO Stream Flow

Stream discharge data was processed using Matlab following rating curve developed by Nutter (1964). Stream water depth (in meters) was measured behind the double V-notch weir in one minute intervals using the Real-Time Hydrologic Network (RTHnet) and streamed online to the SSHCZO website. Discharge values were processed in bulk at the end of each calendar year or as needed. Raw timestamp, water depth, and water temperature RTHnet data were imported to Matlab. Gaps within the one-minute record were filled with NaN values. Values greater than 4 m or 0.1 m less than the 6-hour moving average were considered erroneous and replaced with NaN values. Water temperatures above 50 ˚C or below -10˚C were replaced with NaN values. The one-minute time series was then averaged to ten-minute values. Time intervals, which contained NaN values, were considered NaN in the ten-minute time series. The depth of above weir notch was calculated be subtracting 0.568 m from ten-minute averaged depths. This value was determined through a comparison of manual staff gage measurements and RTHnet depth measurements.

Water depths were then converted from meters to feet and processed through stage-discharge relationship developed by Nutter (1964) to produce discharge in cubic feet per second. Gaps in ten-minute discharge record were then flagged. Gaps less than 24 hours were filled using linear interpolation of the record and flagged as “Fitting (F).” Gaps greater than 24 hours were filled with model data provided by PIHM and flagged as “Model (M).” Observations recorded when ten minute average water temperatures were greater than or equal to 0 ˚C were flagged as “High Quality Observations (H),” while observations record when ten minute average water temperatures were less than 0 ˚C were flagged as “Low Quality Observations (L).” This was intended to identify periods when ice or frozen instrumentation could produce faulty measurements. Discharge values were then converted to cubic meters per day. StreamFlow.m processes raw water depth values to discharge values while providing visualization tools to ensure proper discharge calculations.

Appendix C

Local Meteoric Water Line Regression Procedures

The slope, intercept, and corresponding standard deviations of local meteoric water lines were calculated following an ordinary least squares regression procedure (IAEA, 1992) and a precipitation amount weighted least squares regression procedure (Hughes and Crawford, 2012).

The slope of the ordinary least square regression was calculated using the following equation:

$$m = \frac{\sum xy - \frac{\sum x \sum y}{n}}{\sum x^2 - \frac{(\sum x)^2}{n}} \tag{1}$$

The intercept was calculated using the following equation:

$$b = \frac{\sum y}{n} - m\frac{\sum x}{n} \tag{2}$$

The standard deviation of the slope (m) and intercept (b) were calculated using the following equations:

$$\sigma_m = \frac{S_{y,x}}{\sqrt{\sum x^2 - \frac{(\sum x)^2}{n}}} \tag{3}$$

$$\sigma_b = S_{y,x}\sqrt{\frac{\sum x^2}{n(\sum x^2 - \frac{(\sum x)^2}{n})}} \tag{4}$$

where $S_{y,x}$ is the standard error of the estimate:

$$S_{y,x} = \sqrt{\frac{\sum y^2 - b\sum y - m\sum xy}{n-2}} \tag{5}$$

The slope (m) and intercept (b) of the precipitation amount weighted least squares regression were calculated using the following equations:

$$m = \frac{\sum pxy - \frac{\sum px \sum py}{\sum p}}{\sum px^2 - \frac{(\sum px)^2}{\sum p}} \tag{6}$$

$$b = \frac{\sum py}{\sum p} - m\frac{\sum px}{\sum p} \tag{7}$$

where p is the precipitation amount (mm) for a given sample. The standard deviation of the slope (m) and intercept (b) for the weighted regression were calculated using the following equations:

$$\sigma_m = \frac{S_{y,x}}{\sqrt{\frac{n}{\sum p}\left(\sum px^2 - \frac{(\sum px)^2}{\sum p}\right)}} \tag{8}$$

$$\sigma_b = S_{y,x}\sqrt{\frac{\sum px^2}{n\left(\sum px^2 - \frac{(\sum px)^2}{\sum p}\right)}} \tag{9}$$

where $S_{y,x}$ is the weighted standard error of the estimate:

$$S_{y,x} = \sqrt{\frac{n}{n-2}\frac{(\sum py^2 - b\sum py - m\sum pxy)}{\sum p}} \tag{10}$$